Master Thesis

Evaluation of ultra thin solid state membranes and very small nanopores for DNA translocation with optical tweezers

Sebastian Knust

Experimental Biophysics and Applied Nanosciences
Faculty of Physics
Bielefeld University

sknust@physik.uni-bielefeld.de

May 2015

Academic Advisor: Prof. Dr. Dario Anselmetti

Acknowledgements

First of all I would like to thank Prof. Dr. Dario Anselmetti for granting me the possibility to continue my research and write this thesis in his workgroup. Also, I thank Dr. Lukas Bogunovic for his support, valuable discussions and for proof-reading my thesis.
I am indebted and incredibly thankful to Dr. Andy Sischka, who adviced me throughout my thesis and was readily available for discussions and to answer any questions, even though he was no longer employed by the university at that point.
Many thanks go to my office and lab colleague Roland Hillmann, who was always there for helpful discussions, motivation and the occasionally needed procrastination.
I would also like to thank Christoph Pelargus for all his technical advice and regular discussions. For helpful insights into the theoretical aspects of this work, I thank Andreas Meyer.
For reintroducing me to role playing and for always interesting academic and private discussions, I would like to express my gratitude to Sören Grannemann.
Of course, I thank the Kerbal Space Party team of Dr. Andy Sischka, Dr. André Spiering and Roland Hillmann for relaxing weekends and valuable discussions about orbital mechanics, rocket design, the viability of Asparagus staging and the aerodynamics of sub-orbital space planes.
My thanks also go to Franziska Neugebauer for an outside look of what I'm doing and for proof-reading my thesis.
I am grateful for the samples from Prof. Dr. Meni Wanunu from Northeastern University and from Prof. Dr. Sebastian Fiechter from the Helmholtz Zentrum Berlin für Materialien und Energie.
I also gratefully acknowledge financial support from the Wilhelm and Else-Heraeus Stiftung.
Finally, I would like to thank the whole group of D1 for a great atmosphere, especially my office and lab co-workers: Roland Hillmann, Mirjam Schulz, Marius Dotter, Fabian Heising, Ying Wang and Dr. Andy Sischka.

Contents

1. Introduction

Optical tweezers allow for the manipulation of micrometer-sized objects, moving them in three dimensions and simultaneously measuring the forces acting on them in the range of piconewtons. This has made them a standard tool for single molecule force spectroscopy[1]. In such experiments, the object is typically a bead made of a dielectric, transparent material. The investigated molecules are attached to the bead via specific bindings. Using multiple optically trapped objects, functionalised surfaces, nanopores etc. then allows for detailed and controlled analysis of the force landscape in specific situations. This enables a deeper understanding of the processes and the occurring interactions.

One commonly investigated molecule is deoxyribonucleic acid (DNA), the macromolecule carrying the genome of all known organisms. The most widespread method for analysing DNA with optical tweezers is illustrated in fig. 1.1. It involves attaching the DNA to two beads, using the streptavidin-biotin binding on one bead and the digoxigenin-antidigoxigenin binding on the other bead. Pulling the beads apart provides valuable information about the mechanical behaviour of DNA, both in regard to different environmental conditions and other molecules, so called ligands, which bind to the DNA. Such experiments are performed in our research group on a regular basis.

Another method for investigating DNA with optical tweezers is to analyse the forces acting on DNA during the translocation through nanopores, as illustrated in fig. 1.2. In this case, the DNA is attached to a single bead on one end, with the other end floating

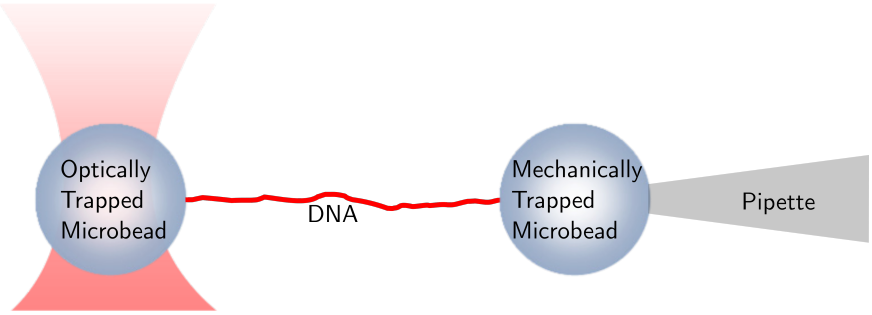

Fig. 1.1.: Stretching DNA between two beads

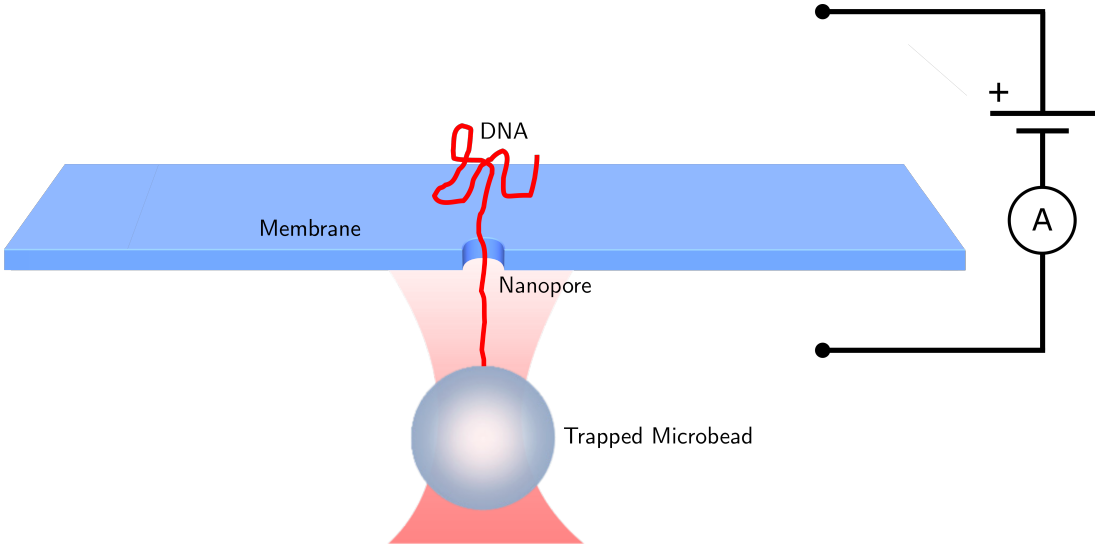

Fig. 1.2.: Translocating DNA through a nanopore

freely. It is then brought in the vicinity of a nanopore with an applied transmembrane voltage, leading to the uncontrolled threading of the DNA *into* the nanopore. Since the other end of the moleculecule is still attached to a bead, it can then be threaded *out* of the pore in a controlled fashion, as slow or fast as desired.

Measuring the electrical current through the nanopore during these translocation events provides an additional data source. Together with the gathered force data, such an experiment allows for label-free measurement of the translocation mechanics of biopolymers, and ultimately might enable *direct-access* DNA sequencing of arbitrary long DNA strands[2]. Additionally, the data might provide some insight into the secondary and tertiary structure of DNA, which contains information about gene expression[3] and which is not available with standard sequencing technologies.

In such experiments, the fundamental choice is that of the nanopore. On the one hand, one can use a biological nanopore like α-haemolysin which is embedded in a lipid membrane[2,4,5]. Such a system is perfectly biocompatible and closely represents intracellular transport processes. Also, the pore has very defined properties; two α-haemolysin in different experiments are mostly identical. However, the successful preparation of such a system proves to be very challenging[2].

On the other hand, solid state nanopores are easy to prepare, very stable, and can serve as a simplified model for biological pores. Additionally, especially silicon-based solid state nanopores are easily integrable in standard microelectronic devices. Furthermore, solid state nanopores can be fabricated in a variety of sizes, thicknesses and

surface properties. However, precise control of the fabrication process is challenging and reproducibility of a pore is near impossible[6]. Nevertheless, due to the numerous advantages of solid state nanopores, they have been used exclusively for DNA translocation experiments in our lab.

The thickness of the nanopores should be as low as possible. Very thin nanopores both ease the theoretical description of effects (e. g. via molecular dynamics simulations) and are a requirement for DNA sequencing approaches, since the number of DNA bases within the nanopore should be as low as possible. Also, nanopores with a very small diameter are highly interesting. Base specific interactions might be easier to measure, since the interactions between DNA and nanopores are generally stronger for smaller pores. Additionally, they ease the theoretical description as well.

Therefore, in this work I investigate and evaluate different ultra thin solid state membrane materials for use as a nanopore material in DNA translocation experiments with optical tweezers. The goal of this thesis is to find a new material that is suitable for use as a standard material in our experiments and to develop the necessary preparation protocols. Since a new material always has to be compared with its predecessors, this work also serves as a review concerning materials of the experiments performed and the results gained previously in our group. Additionally I examine the translocation behaviour of DNA through very small nanopores and analyse the viability of such experiments.

Since the theory, setup and much of the preparation is independent of the membrane material, this work is split into two parts. The first part, consisting of this introduction and chapters two and three, provides the material-independent information. In the second chapter, I will briefly outline the history and physical basics of optical tweezers, both in general and with a special look on the optical tweezers setup used in our group. The third chapter features an overview of DNA translocation through nanopores, from biological and biophysical foundations to a general overlook on nanopore creation in solid state nanopores.

In the second part, I will present each evaluated material in a separate chapter. For each material, I start with a short general introduction, followed by the specific preparation instructions and finally the results. This part is started with our standard material, silicon nitride. To enable an independent analysis of both small pores and new materials, small pores are investigated exclusively in silicon nitride.

This thesis ends with the conclusions and an outlook on further work. In the appendix, a detailed description of the automated membrane material monolayer flake detection process developed in the course of this thesis can be found.

2. Optical Tweezers

2.1. History

The first basis for what we call *optical tweezers* nowadays was laid by Arthur Ashkin in his 1970 paper[7] "Acceleration and Trapping of Particles by Radiation Pressure", which describes that when a bead approaches a TEM_{00}-mode laser beam, it is both "accelerated in the direction of the light" and "drawn in to the beam axis". This effect, the 2D or radial optical trapping, is the fundamental effect on which every optical tweezers is based.

There are multiple possibilities to use this effect to create a 3D optical trap. On the one hand, a 2D optical trap can be coupled with another force countering the acceleration along the optical axis. For example, another optical trap[7] or a setup using gravitation (leading to the term *Optical Levitation*[8]) can be used. On the other hand, a single beam can be focused tightly, creating a 3D single beam optical trap without the need for any external forces, as first demonstrated 1986 by Ashkin et al.[9] Such a 3D single beam optical trap is commonly called *optical tweezers*.

Optical tweezers soon became a standard tool for single molecule force spectroscopy (next to atomic force microscopy and, more recently, magnetic tweezers)[1]. Here, the studied molecules are attached to a trapped bead. Famous works depending on optical tweezers include the characterisation of the kinesin mulecular motor system by Steven Block et al. in 1990[10] and the description of the entropic elasticity of λ-Phage DNA (according to the worm-like chain model) by Carlos Bustamante et al. in 1994[11].

At the experimental biophysics group in Bielefeld, optical tweezers have been introduced by Andy Sischka in 2001[12]. They were first used for DNA stretching experiments between an optically trapped bead and a bead trapped by a micropipette. A second optical tweezers system was introduced by Andy Sischka in 2007[13]. It is dedicated to investigating the translocation of DNA through nanopores and featured force analysis based on backscattered light detection. In 2012, I added a video-based force analysis method to that system[14].

2.2. Theory of optical trapping

2.2.1. Gaussian optics

Electromagnetic waves such as light are subject to the Maxwell equations, from which the wave equation (also known as the d'Alembert equation) describing a scalar function $u(\boldsymbol{x}, t)$ can be derived*:

$$\frac{\partial^2 u}{\partial t^2} = c^2 \nabla^2 u \tag{2.1}$$

c in this equation is the local speed of light $c = c_0/n$. Writing the wave equation for an euclidean coordinate system for the light field strength E yields

$$\left(\frac{\partial^2}{\partial x^2} + \frac{\partial^2}{\partial y^2} + \frac{\partial^2}{\partial z^2} - \frac{1}{c^2} \frac{\partial^2}{\partial t^2} \right) E = 0 \tag{2.2}$$

Of the many possible solutions for this partial differential equation, the most simple one is the plane wave moving in e. g. z direction:

$$E(z, t) = E_0 cos(\omega t - kz) \tag{2.3}$$

with the angular frequency ω being related to the wavenumber k by $\omega = kc$.

Spherical waves form another common group of solutions to the wave equation. Their field strength depends on the distance r from the origin point of the wave. They are described by:

$$E(r, t) = \frac{A}{r} \exp\left(-i(kr - \omega t)\right) \tag{2.4}$$

Assuming the wave is centred at the origin of the coordinate system, it is obvious that $r = \sqrt{x^2 + y^2 + z^2}$.

Let us however assume that it is not centred in the coordinate system, but rather at the complex location $(0, 0, -iz_R)$ with $z_R \in \mathbb{R}$. Introducing $q := z + iz_R$ and using the notation of a cylindrical coordinate system with $r = \sqrt{x^2 + y^2}$ then leads to the form

$$E(r, z, t) = \frac{A}{\sqrt{q^2 + r^2}} \exp\left(-i(k\sqrt{q^2 + r^2} - \omega t)\right) \tag{2.5}$$

Analysis of the phase reveals a phase shift differing from that of a plane wave with

*The derivations in this subsection are covered in most textbooks on lasers and performed here according to Eichler and Eichler [15, p. 225ff] and Svelto [16, p. 150ff]

the same frequency. This difference is the *Gouy phase shift*, given as[17]

$$\zeta_G = \arctan \frac{z}{z_R} \tag{2.6}$$

Thus, the phase shift is most notable at and near the position of the beam waist.

As we are only interested in the beam near the axis in the far field, the paraxial approximation $r \ll |q|$ holds true, which allows us to simplify the equation to

$$E(r, z, t) \approx \frac{B}{q} \exp\left(-i\frac{kr^2}{2q}\right) \exp\left(i(\omega t - kz)\right) \tag{2.7}$$

with $B = A\exp(kz_R)$ just like A an undetermined amplitude.

We can now separate the real and imaginary part of $1/q$, which yields

$$\frac{1}{q(z)} = \frac{z - iz_R}{z^2 + z_R^2} = \frac{1}{R(z)} - i\frac{2}{k\mathrm{w}^2(z)} \tag{2.8}$$

Here, $\mathrm{w}(z)$ (written upright to avoid confusion with ω) denotes the beam width, which is directly related to the imaginary centre of the spherical wave described by z_R:

$$\mathrm{w}(z) = \sqrt{\frac{2z_R}{k}}\sqrt{1 + \frac{z^2}{z_R^2}} \tag{2.9}$$

In literature and data sheets, one often finds the minimum beam waist $\mathrm{w}_0 = \mathrm{w}(0) = \sqrt{\frac{2z_R}{k}}$ as a parameter to describe a Gaussian beam.

The radius of curvature of the wavefronts $R(z)$ also depends on z_R:

$$R(z) = z + \frac{z_R^2}{z} \tag{2.10}$$

Inserting equation 2.8 into equation 2.5 gives the most common description of a Gaussian beam, which is a paraxially approximative solution of the wave equation based on the above:

$$E(r, z, t) \approx \frac{B}{q} \exp\left(-\frac{r^2}{\mathrm{w}^2(z)}\right) \exp\left(-i\frac{kr^2}{2R(z)}\right) \exp(i(\omega t - kz)) \tag{2.11}$$

The intensity profile of a Gaussian beam is a Gaussian:

$$I = I_{\max} \exp\left(\frac{-2r^2}{\mathrm{w}^2(z)}\right) \tag{2.12}$$

The Gaussian beam is of essential importance in the field of optical tweezers as it describes the fundamental transversal mode TEM_{00} of many lasers.

2.2.2. 2D optical traps

For trapped particles in the Mie size regime ($2r \gg \lambda$) simple ray optics can be used to describe optical trapping[9]. The two important effects are refraction and (to a lesser extend) reflection. In both cases, we utilise the conversation of momentum with respect to the momentum of the light, $p = h/\lambda$.

Fig. 2.1 shows the basic effects for a polystyrene (PS, $n = 1.572$[18]) bead suspended in water ($n = 1.325$[19]). It should be noted that for 2D trapping, an unfocused beam is sufficient. Symmetrically to the light's axis, the refraction induces forces away from the centre and slightly in the direction of the light, resulting in axial but no radial force. The much weaker forces induced by reflection also point in the direction of the beam and produce no radial force.

If the beam hitting the bead is radially symmetric, e. g. a Gaussian beam, the effects depend upon the position of the bead in relation to the beam. If the bead is radially centred inside the beam, the intensity of the rays is symmetrical to the centre axis of the bead and the previous description holds true.

If however the bead is not centred inside the beam, the induced forces near the beam centre are stronger then the ones further away, as indicated in fig. 2.2. As the forces induced by refraction point away from the centre axis of the bead, it is pulled into the centre of the Gaussian beam, where again any displacement is counteracted with a force.

This results in a bead that is radially trapped in the centre of the light beam and accelerated along the direction of the light.

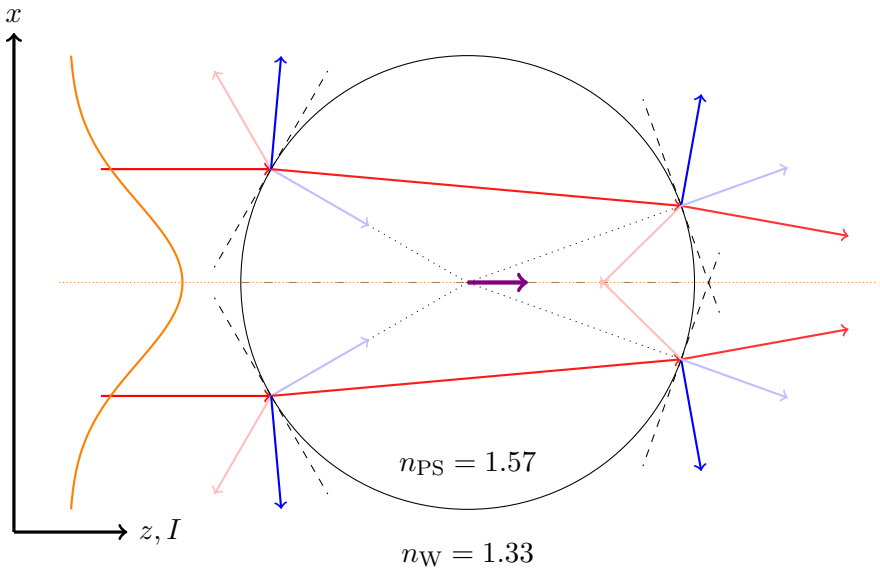

Fig. 2.1.: Light paths (red, intensity distribution in orange) and resulting forces (blue) for refraction (saturated) and reflection (pale) at a polystyrene bead suspended in water. The resulting total force is shown in violet.

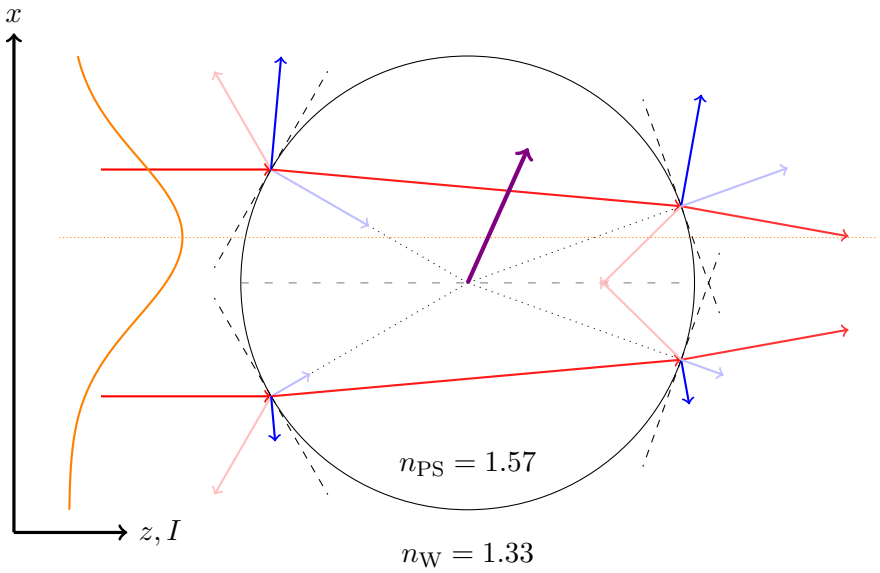

Fig. 2.2.: Light paths (red, intensity distribution in orange) and resulting forces (blue) for refraction (saturated) and reflection (pale) at a displaced polystyrene bead suspended in water. The resulting total force is shown in violet.

2.2.3. 3D optical traps

By using a tightly focused laser beam, a single beam 3D optical trap can be accomplished. Again, we have the two effects of refraction and reflection, and again the effects caused by reflection are small enough to be disregarded.

Assuming the light is coming from the left, if the bead is located too far to the right, because of the now strongly diverging beam, the refraction forces point backwards, creating a negative radiation pressure and pushing the bead to the left. This is illustrated in fig. 2.3.

If however the bead is positioned too far to the left, the radiation pressure is positive as with the two-dimensional trap, pushing the bead to the right. This is shown in fig. 2.4.

For radial bead displacements, the two-dimensional principle works as before: The rays passing through the part of the bead farthest away from the beam centre are weaker, therefore the radial forces do not compensate each other and force the bead back into the centre of the beam.

The result therefore is that the bead is trapped in all three dimensions at a point centred in the beam, slightly behind the focus.

It should be noted that both with 2D and with 3D optical traps, we do not necessarily require a Gaussian beam profile. In fact, in our setup we use a central obstruction filter to block out the centre portion of the TEM_{00}, giving something akin to a TEM_{01}^{*} (a superposition of two TEM_{01} profiles rotated by 90° to each other). As is obvious from ray optics, we only require that the profile is radially symmetric and has its highest intensity near the center. Near in this context means that the distance should be much lower then the radius of the trapped particles. Both conditions are fulfilled by our setup, and therefore the description of the trapping behaviour still holds true.

2.2.4. Hooke's Law

In optical tweezers experiments, the forces applied to the trapped bead are of interest, but cannot be measured directly. However, the displacement of the bead within the trap is usually accessible. For small displacements, we can reasonably assume that the potential landscape approaches a harmonic one[9], i. e.

$$\Phi(x, y, z) = \frac{1}{2}\left(k_x x^2 + k_y y^2 + k_z z^2\right) \tag{2.13}$$

with the displacement (x, y, z). As is conventional, x and y denote the radial displacement, i. e. displacement in the plane perpendicular to the trapping beam. z denotes

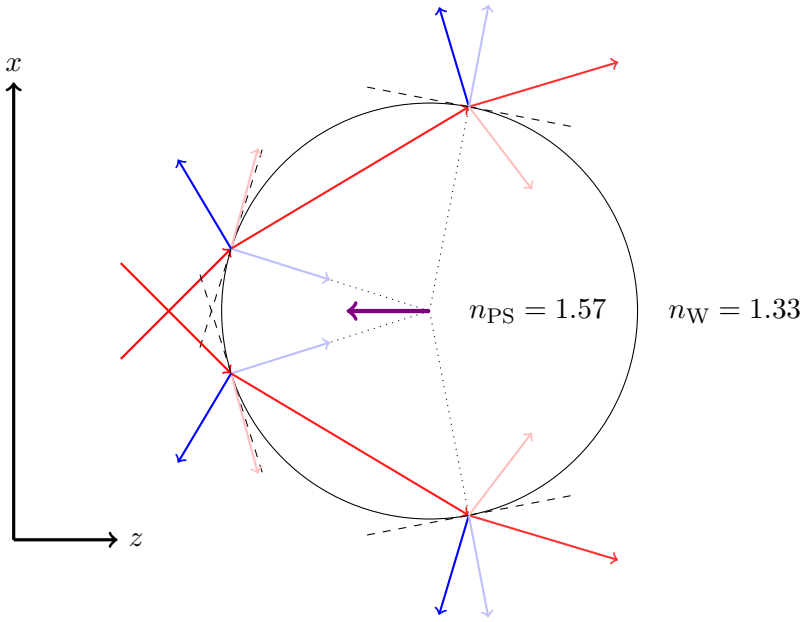

Fig. 2.3.: Light paths (red) and resulting forces (blue) for refraction (saturated) and reflection (pale) at a polystyrene bead suspended in water. The bead is displaced away from the laser source. The resulting total force is shown in violet.

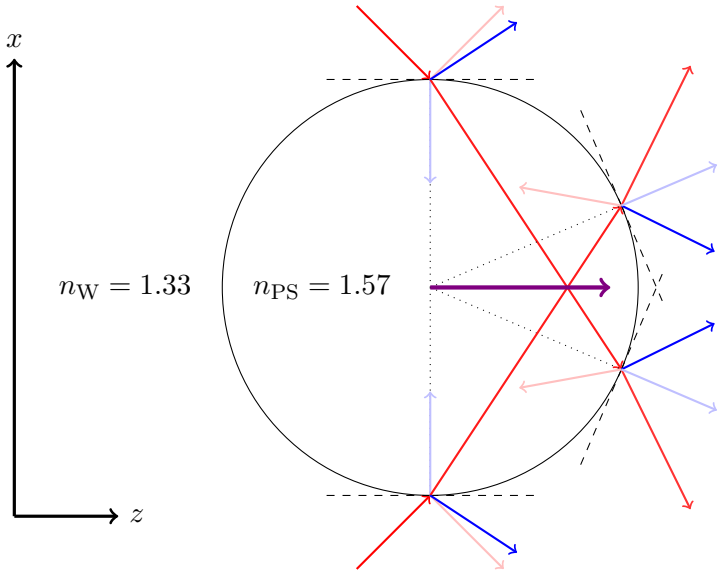

Fig. 2.4.: Light paths (red) and resulting forces (blue) for refraction (saturated) and reflection (pale) at a polystyrene bead suspended in water. The bead is displaced towards the laser source. The resulting total force is shown in violet.

the axial displacement, i. e. displacement in the direction of the trapping beam.

Thus it follows that trapped particles in optical tweezers obey Hooke's Law:

$$\vec{F} = -\vec{\nabla}\Phi(x,y,z) = -\begin{pmatrix} k_x x \\ k_y y \\ k_z z \end{pmatrix} \tag{2.14}$$

The validity of these assumptions can be verified numerically by integrating the forces acting on the bead by a single light beam over all light beams passing the bead. Such calculations were performed by Arthur Ashkin[20] with the results shown in figure 2.5. As can be seen, the assumptions hold true for $|x|, |y| < 0.3r, |z| < 0.6r$.

The shift in the equilibrium position for axial displacement stems from the radiation pressure. Since in experiment position detection is performed relative to the equilibrium position, this effect can be ignored safely.

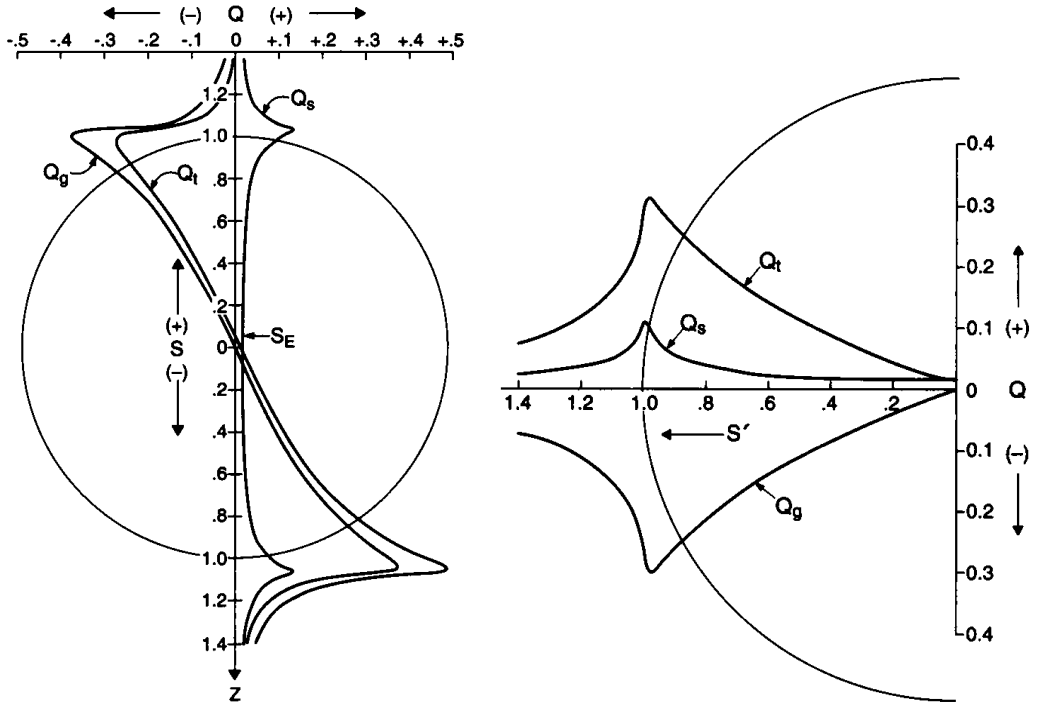

(a) Axial displacement (b) Radial displacement

Fig. 2.5.: Gradient, scattering and total force coefficients Q_g, Q_s, Q_t (for $F = nQP/c$ with laser power P, speed of light c) at a bead with relative index of refraction $n := n_{\text{Bead}}/n_{\text{Fluid}} = 1.2$ as calculated by Ashkin[20]

2.2.5. Trapping in the Rayleigh regime

Even tough in our experiments, we are well within the Mie regime, it should be noted that optical tweezers can be described in the Rayleigh regime ($2r \ll \lambda$) nicely as well, as briefly shown below.

The scattering force for a bead with radius r, relative index of refraction m (for polystyrene beads in water, $m = 1.186$) in a medium with index n calculated by Rayleigh theory is[†]

$$F_{\text{scat}} = \frac{nP_{\text{scat}}}{c} = \frac{I_0 n}{c} \frac{128\pi^5 r^6}{3\lambda^4} \left(\frac{m^2 - 1}{m^2 + 2} \right)^2 \tag{2.15}$$

The gradient forces result from dielectrophoresis: The electromagnetic field induces a dipole momentum in the bead, which is in turn subject to interactions with the electromagnetic field. The resulting gradient force is[9]

$$F_{\text{grad}} = -\frac{n}{2}\alpha \nabla E^2 = -\frac{n^3 r^3}{2} \left(\frac{m^2 - 1}{m^2 + 2} \right) \nabla E^2 \tag{2.16}$$

Comparing the two forces at the position of maximum axial gradient, which for a Gaussian beam is $z = \pi \mathrm{w}_0^2 / \sqrt{3}\lambda$, yields the following axial trap stability condition

$$R = \left| \frac{F_{\text{grad}}}{F_{\text{scat}}} \right| = \frac{3\sqrt{3}}{64\pi^5} \frac{n^2}{\left(\frac{m^2-1}{m^2+2} \right)} \frac{\lambda^5}{r^3 \mathrm{w}_0^2} > 1 \tag{2.17}$$

For polystyrene beads in water with a 1064 nm laser, this would lead to a maximum bead radius in the range of 230 nm. However, for such large beads, the Rayleigh regime is no longer valid and we are in a transition region to the Mie regime.

2.2.6. Langevin equation

The Langevin equation, first published by Paul Langevin in 1908[22,23], is a basic equation describing the random Brownian motion of a particle in an environment. For a particle trapped by optical tweezers, it can be formulated without loss of generality in one dimension (since the problem is trivially separable for each dimension) as:

$$m\ddot{x} + \gamma\dot{x} + U' = \xi(t) \tag{2.18}$$

[†]For a detailed derivation, see chapter 3.2 of Kerker [21], especially equations (3.2.7), (3.2.23) and (3.2.24)

$\xi(t)$ is the Brownian noise, a Gaussian white noise following the Fluctuation-Dissipation-Theorem, thus with:

$$< \xi(t) >= 0 \ \forall t \qquad < \xi(s)\xi(t) >= 2\gamma k_B T \delta(t-s) \ \forall s,t \tag{2.19}$$

where $< \xi >$ denotes the expectation value (average) of ξ for many iterations.

γ is the drag coefficient. Since we can assume spheres with very low Reynolds numbers and therefore laminar flow, the Stokes-Einstein equation holds true[‡], giving

$$\gamma = 6\pi\eta R \tag{2.20}$$

with the viscosity η and the bead radius R.

Since the characteristic dampening time $t_d = m/\gamma$ is very small (for typical experimental values, we get $t_d = 6 \times 10^{-7}\,\mathrm{s}$), the system is considered overdamped. Therefore, the acceleration term can be ignored. Furthermore, the derivation of the potential is simply $U' = kx$, as shown above. Therefore, we get

$$\gamma\dot{x} + kx = \xi(t) \tag{2.21}$$

Fourier transformation leads to

$$\tilde{x}(\omega) = \frac{\sqrt{2\gamma k_B T}}{i\omega\gamma + k} \tag{2.22}$$

which gives us the power spectrum as[25]

$$P(f) = \frac{k_B T}{2\pi^2\gamma(f^2 + f_c^2)} \tag{2.23}$$

with the corner frequency $f_c = k/2\pi\gamma$.

2.3. Experimental setup

The setup used in our experiments, as illustrated in fig. 2.6 is integrated in an Axiovert 100 microscope (Zeiss, Germany) and has been described in detail in multiple papers[13,14]. Briefly, it consists of a Nd:YAG laser (LCS-DTL-322-1000[26], Laser 2000, Germany; 1064 nm, 1 W, linear polarised TEM_{00}, full divergence angle 1.6 mrad, beam diameter (1.2 ± 0.1) mm), a longpass to filter out the pumping light, a polarised beam

[‡]For a detailed derivation, see e. g. §20 of Landau and Lifschitz [24]

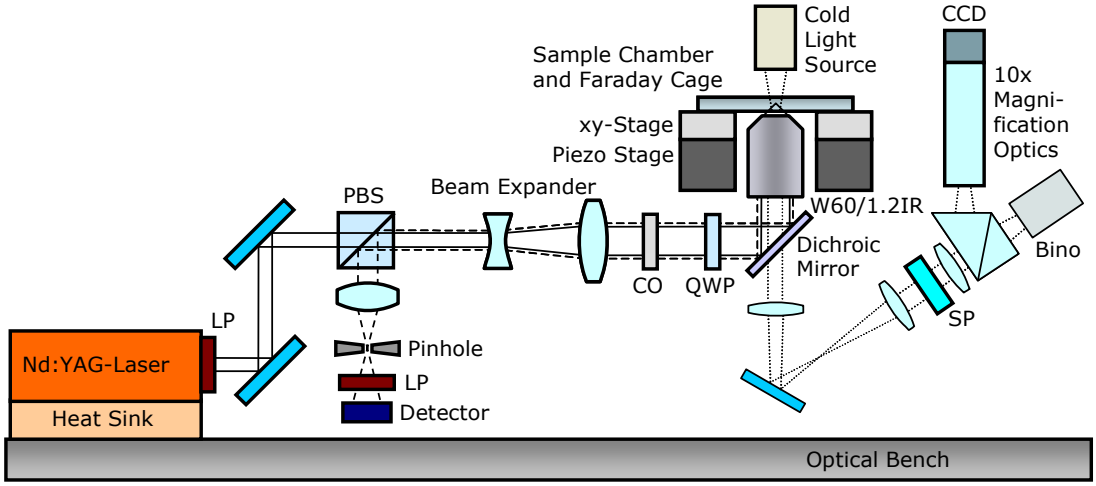

Fig. 2.6.: Optical tweezers setup suitable for both backscattered light axial force and video-based force analysis.

splitter that directs the backscattered light onto a linear detector, a beam expander, a central obstruction filter (creating a TEM_{01}^{*}-like intensity profile to lessen the interference effects as discussed in section 2.4.1), a quarter-wave-plate and a dichroic mirror.

The sample chamber is contacted to an Axopatch 200B amplifier (Molecular Devices, CA) by an agarose gel and cyanoferrat salt bridge with embedded platinum wires. Data from the linear detector and the Axopatch amplifier is acquired with a NI PCI-6036E IO card (National Instruments, TX; 16 bit, 200 kS s^{-1}). The sample chamber setup used for DNA translocation experiments will be explained in detail in section 3.5.

The 60× trapping objective (UPL-APO60W/IR) is a water immersion objective with a numerical aperture of 1.2. As very small electric currents are measured in nanopore experiments, the piezo stage, sample chamber and end of the illumination fibre optics are placed inside a Faraday cage.

For video-based analysis, an additional 10× post-magnification optics is integrated, projecting the image onto a Guppy Pro F-031 monochrome CCD camera (Allied Vision Technologies, Germany; Sony ICX618 sensor, 656 px × 492 px, 5.6 µm pixel size, 14 bit A/D converter, 123 fps). Illumination is done with a KL-2000 LED cold light source (Schott, Germany; 7 × 9 W high power LEDs, 1000 lm output). The light is brought to the sample chamber by fibre optics and focused by a collimator from a distance of

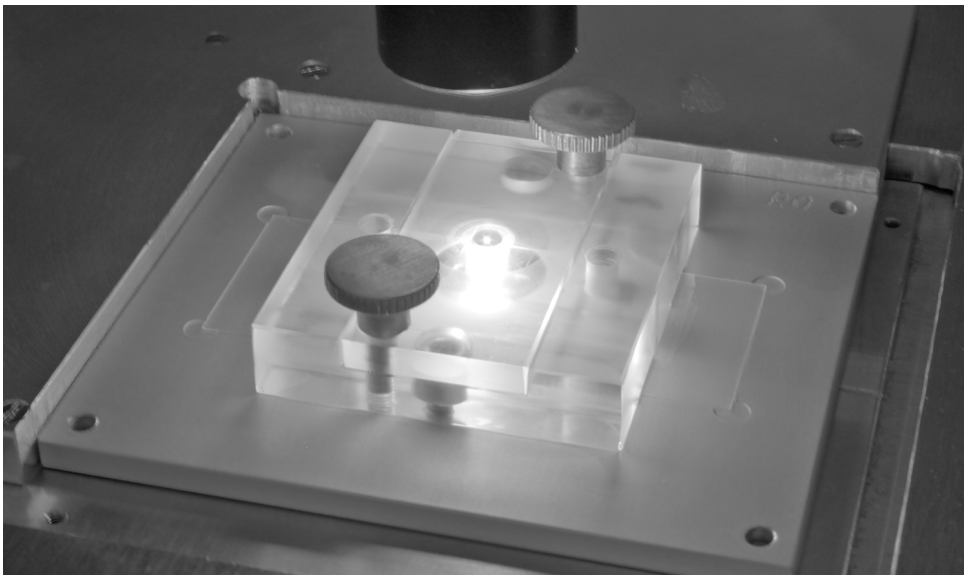

Fig. 2.7.: Illumination of the sample chamber

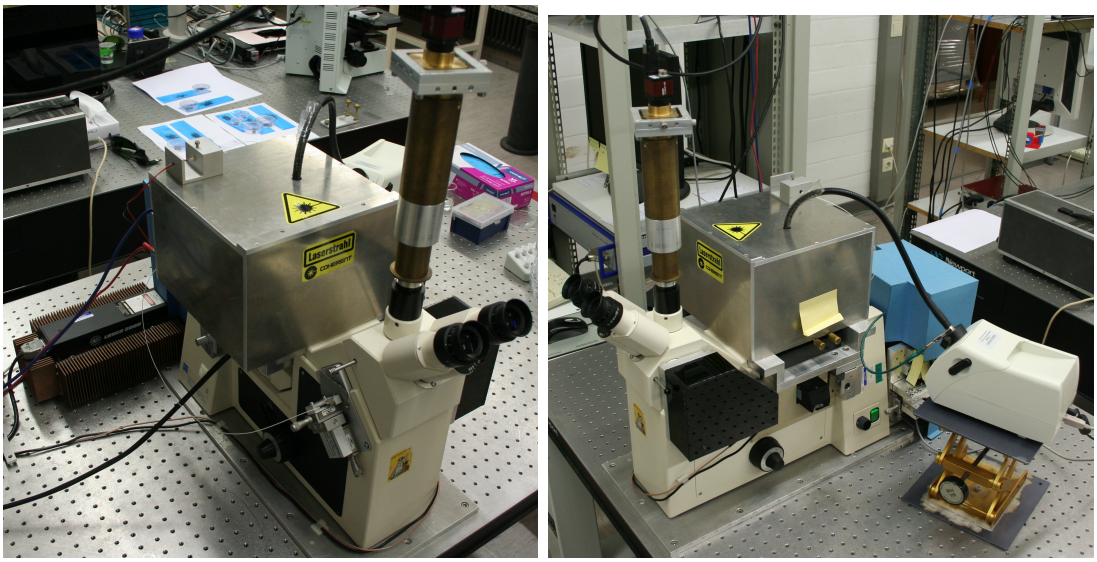

Fig. 2.8.: Pictures of the current setup

approx. 2 cm.

Further integrated are a standard b/w CCD camera for monitoring purposes and short pass filters in the visible light path to block the IR light residues still transmitted by the dichroic mirror.

2.4. Force analysis

As mentioned before, force analysis for optical tweezers is based on Hooke's Law and measures the displacement of the bead. For this, two main methods are employed: scattered light analysis and, as of late, video-based analysis.

2.4.1. Scattered light analysis

For scattered light analysis, the scattering of the trapping laser on the trapped bead is utilized. For *radial forces*, analysis is rather straightforward for both forward and backward scattered light. In both cases, the beam is projected onto either a four-quadrant photodiode (for both radial dimensions), or a linear detector (if one dimension is sufficient).

For *axial forces*, the intensity of the scattered light is analysed, either by adding the outputs of the four-quadrant photodiode or by splitting the scattered light beam and projecting it onto a photodiode as well. In the case of backscattered light detection, the displacement is linear to the amount of reflected light from the bead. In case of forward scattered light detection, the light passing through the bead interferes with the light passing next to the bead, also leading to a change in intensity. The Gouy phase shift ζ_G complicates the theoretical description[27]. However, for usual displacements encountered with optical tweezers a linear approximation is sufficient[27].

Forward scattered light analysis, first shown by Denk and Webb in 1990[28], of course requires a second objective above the sample chamber. Since high aperture objectives with low working distances are commonly employed, this limits the versatility of the system. Since the reflectivity of the used beads is usually quite low, the majority of the trapping beam is forward scattered, enabling high signal to noise ratios.

In contrast, *backward scattered* light has to cope with the possibly low reflectivity of the bead. Since usually infrared Nd:YAG lasers are used for trapping, one might consider using a second laser in the visible spectrum to detect the displacement[29]. This second laser can be chosen in such a way that the reflectivity of the bead is maximal at the laser wavelength. However, this solution has two major drawbacks: First, the setup is difficult to initially calibrate since both laser beams and foci must overlap

exactly. Second, the detection laser works as a second, albeit less powerful trapping laser as well. Therefore, two overlapping traps are introduced. Depending on the size of the offset, an unstable trap or a metastable two-trap layout can be created. In the latter case, the bead regularly hops between both trap positions, even if they are just some nanometers apart. This behaviour can be described by Kramers rate theory[30]. Since one might want to analyse sample systems in which such a state hopping occurs naturally[31], such setup-induced hopping is of course unacceptable.

Another possibility to cope with the low reflectivity of the bead, which was introduced into our setup in 2008[13], is to utilise the polarisation of light, first introduced by Carter et al.[32]. Here, the s-polarised light from the laser first passes a polarising beam splitter cube and then a quarter-wave-plate. The now right-circular polarised light is backscattered at the bead, becoming left-circular polarised. The quarter-wave-plate then converts it to p-polarised light, which is now reflected by the polarising beam splitter cube to the detection units. This way, almost no intensity is lost, thus allowing backscattered light analysis with a single laser at good signal to noise ratios.

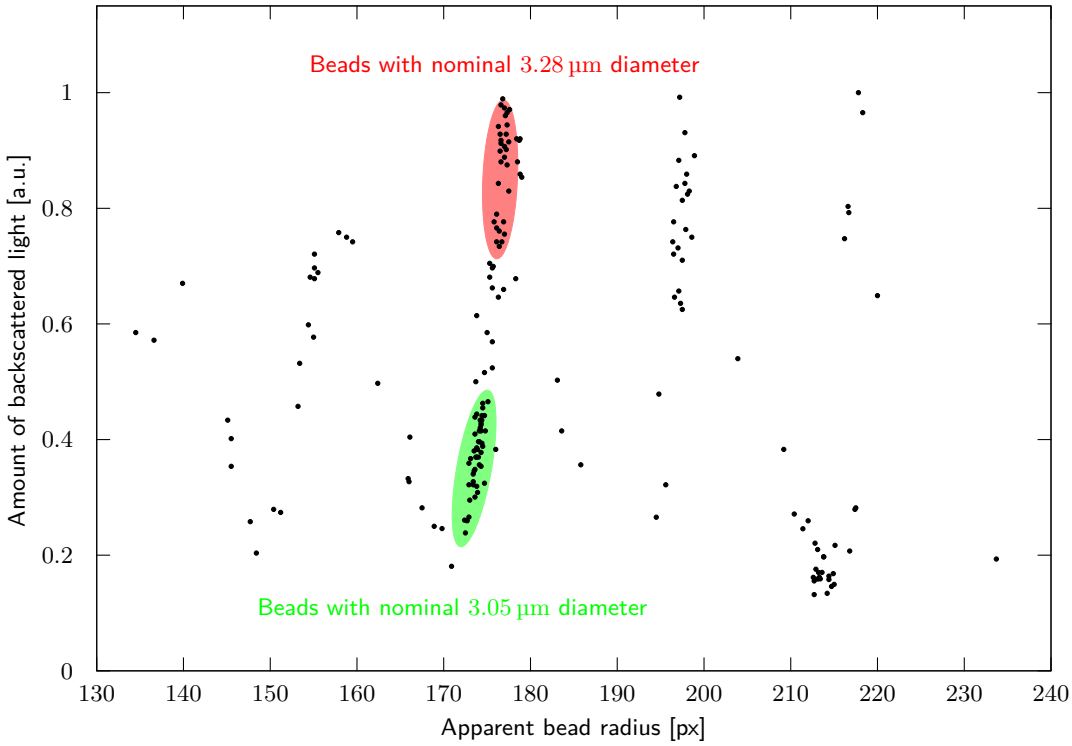

Fig. 2.9.: Dependency of the amount of backscattered light on the apparent bead size. Measurements performed by A. Spiering, 2012[14]

Of course, one might as well try to increase the reflectivity of the bead, e. g. by using special coatings. Also, especially for beads whose size approaches the wavelength of the trapping laser, interference effects based on internal reflection give rise to a strong dependency of the reflectivity on the bead size. Fig. 2.9 illustrates that dependency. The apparent bead size in pixels used on the abscissa can be considered linear to the real bead size.

It should be noted that for backscattered light analysis of beads trapped in the vicinity of a (even weakly) reflecting surface (such as a membrane), interference artefacts can occur. This effect is especially problematic for axial force measurements, since on an applied force the force signal will be subject to interference. Spatial filtering[29], as in confocal microscopy, as well as a central obstruction filter[13] (CO), creating a TEM_{01}^{*}-like intensity profile, can be used to lessen the problem.

The interference artefacts in backscattered light analysis near interfaces also masks a fundamental trap interference effect discussed in the next section.

2.4.2. Video-based analysis

Since the classical scattered light analysis approach suffers from some inherent disadvantages, a fundamentally new force analysis method is sought. Video-based analysis is such a method, relying on the tracking of a particle (the trapped bead) in a video image by software. Whilst that task is rather trivial from a software point of view, with first publications dating back to the mid 1990s[33], they suffered from the slowness of both data acquisition and computation. Typically, 25 Hz PAL cameras were used. In contrast, scattered light analysis is an analogue technique, being only limited by the speed of AD converters and, ultimately, by the rate of photons and internal detector decay processes. Therefore, typical data rates of dozen or hundreds of kilohertz are achieved.

With the recent rise in computation power, storage capacity and speed, and the advances in high-speed, high-sensitivity CCD and CMOS cameras (the latter allowing for arbitrary regions of interest), higher detection rates are achievable[34,35].

Most video-based analysis methods are only used for tracking the position of the bead in the focal plane, i. e. they are suitable for *radial force* detection. Here, any particle tracking algorithm can be used. The deflection of the bead is simply the difference between the current bead position and the zero-force bead position.

For *axial force* detection, i. e. detection of bead movement along the optical axis, the defocussing of the bead as it leaves the focal plane must be analysed. This is usually done by detecting the airy disk pattern and matching it, either analytically by fitting

a Bessel function to the image, or by correlating the image with a set of calibration images taken at different, known deflections[36]. However, both methods work best for detecting displacements in the micrometer range of an already defocused bead. Since in our case, the bead is displaced by only a few tens to hundreds nanometers, these methods are not practical.

Another possibility, developed during my Bachelor thesis, is to use the minute changes of the apparent bead size caused by defocusing. It should be noted that the change of size cannot be explained by the thin lens formula, as it is stronger by a factor of 100. Instead, the change is a result of the combination of defocusing blur, changed lighting conditions and internal interference. This, in combination with the fact that due to radiation pressure, the zero force point is already slightly defocused, allows for a linear approximation for both positive and negative displacements / forces:

$$\Delta z = \beta \cdot \left(\frac{r}{r_0(z)} - 1 \right) \tag{2.24}$$

Here, β is a conversion factor, typically in the range of $\beta = 10\,\mu\text{m}$, r is the apparent bead radius in pixels and $r_0(z)$ is the radius at zero force, which used to be linearly approximated due to changed lighting conditions. However, the chip layout necessary for novel material membranes introduces a strongly non-linear behaviour of the zero force radius, which is explained in detail in section 7.3.3.

Since usually both conversion factor β and trap stiffness k are not known exactly and since $F \propto k\beta$, in force calibration the product $k\beta$ is calibrated.

The detection of the apparent bead size is illustrated in fig. 2.10. First, regions of interest for the falling (inner, red) and rising (outer, green) edges are selected manually. As the trap position remains constant except for long-term (mechanical) drift, this selection only has to be performed periodically and can be auto tracked on demand. Then, the strongest falling and rising edges along 360 spokes are calculated by gradient approach. For each spoke, the middle point between the two detected edges is calculated. Finally, a circle is fitted through these middle points, providing both position (x and y) and apparent radius (r) of the bead.

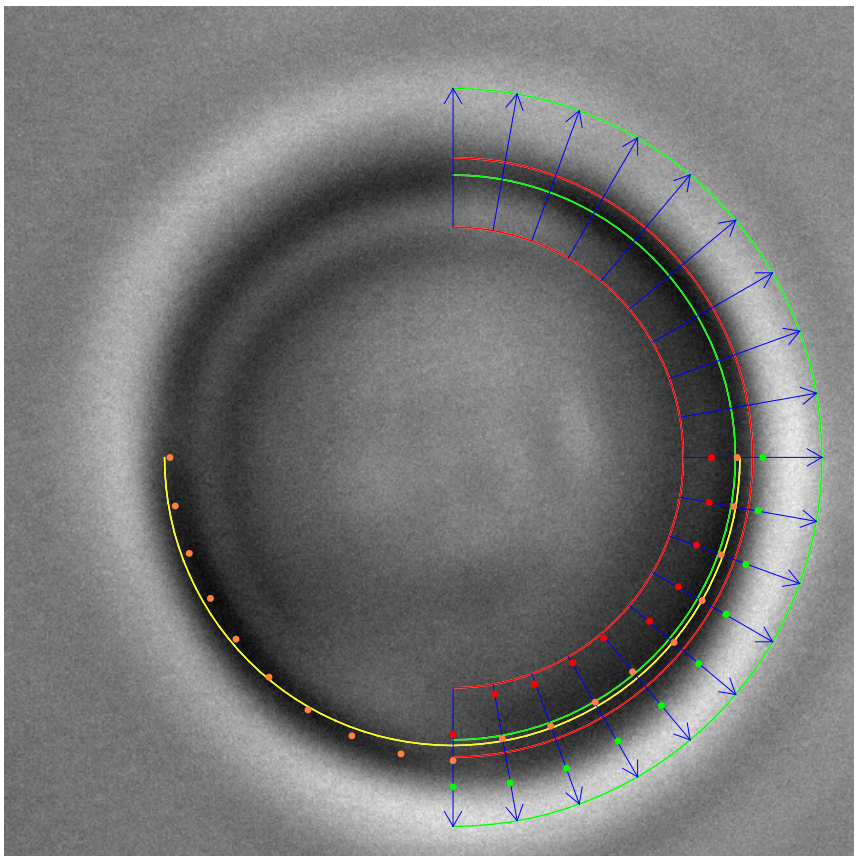

Fig. 2.10.: Still frame of a PS bead with manually selected circular region of interest for falling (red) and rising (green) edge with search spokes (blue). The red and green dots are the recognized falling and rising edges. The orange dots are the resulting mid-points between the two edges, through which the yellow circle is fitted. For clarity, only every tenth spoke with corresponding edges is shown.

2.5. Interference effects in the vicinity of weakly reflecting surfaces

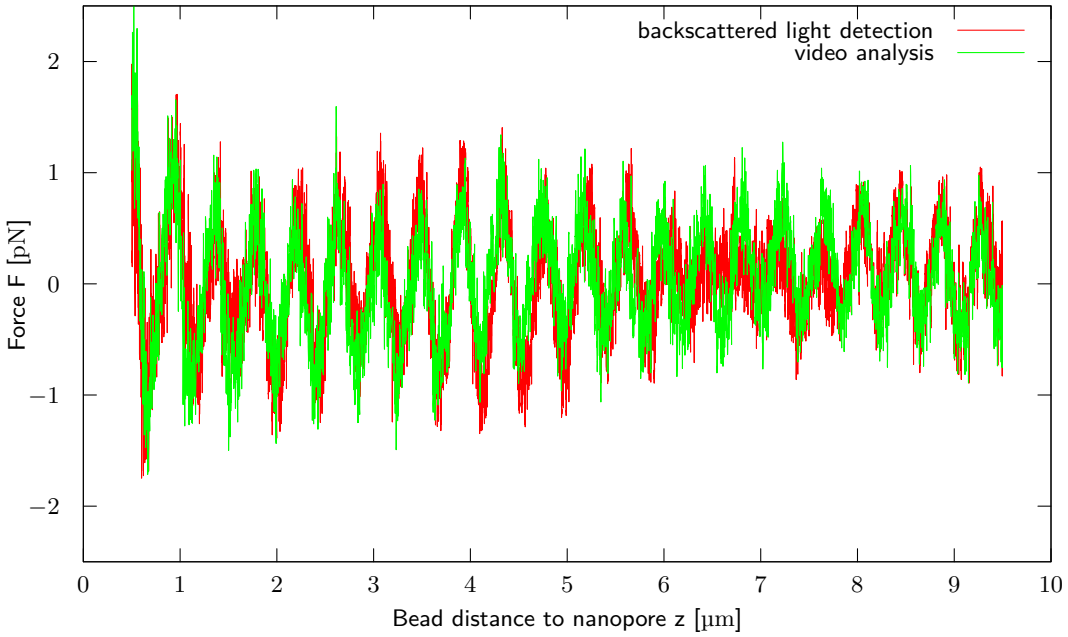

Fig. 2.11.: 3.28 µm polystyrene bead approaching a 20 nm thick Si_3N_4 membrane, measured with backscattered light detection and video-based analysis. Optical trap stiffness is $k \approx 50\,\mathrm{pN\,\mu m^{-1}}$

As mentioned above, approaching a weakly reflecting surface with a trapped bead leads to interference effects. Both bead and surface act as the "mirrors" of an optical resonator. Therefore, a standing wave obeying the resonator condition $j\lambda/2n$ with the index of refraction n and an integer j is created. This standing wave leads to a pseudo-force measured both with scattered light and with video-based force analysis. In fact, the trap position shifts, which is misinterpreted as a force.

In the case of a 3.28 µm polystyrene bead and a 20 nm thick Si_3N_4 membrane, the reflectivities are 0.75 % and 1.08 %[13], respectively. The interference pattern for this setup can be seen in fig. 2.11. The measured resonator condition $j \cdot 418\,\mathrm{nm}$ fits quite well with the theoretical $j \cdot 402\,\mathrm{nm}$. With a trap stiffness of $k \approx 50\,\mathrm{pN\,\mu m^{-1}}$, the resulting pseudo force of $\pm 1\,\mathrm{pN}$ corresponds to a shift of the trap position of $\pm 20\,\mathrm{nm}$.

2.6. Force calibration

Until now, force values have been acquired in arbitrary units. Whilst a direct conversion might theoretically be possible, it would require exact knowledge of trap geometry and laser power. Both values are constantly fluctuating and not readily available. Therefore, empirical calibration protocols are employed. They commonly fall into two categories: drag force based analysis and analysis of the Power Spectral Density (PSD).

2.6.1. Stokes Law

As mentioned before, spherical particles in a laminar flow are subject to a force according to Stoke's Law:

$$\vec{F} = -6\pi\eta r\vec{v} \tag{2.25}$$

Laminar flow as a prerequisite for the validity of Stoke's Law is characterised by a Reynolds number $Re = v\,r\rho/\eta \ll 100$, with fluid density ρ. In our case, for a 3.05 µm polystyrene bead in water ($\eta = 0.89\,\mathrm{mPa\,s}$ at 25 °C), the velocity corresponding to a force of 10 pN is $391\,\mu\mathrm{m\,s^{-1}}$. In that case, the Reynolds number would be $Re = 0.67 \times 10^{-3}$. Thus, the assumption of laminar flow holds true[37].

Additional attention has to be paid for movement parallel to a surface. If the distance to the surface h is in the order of magnitude of the bead size, the drag coefficient must be adjusted[37]:

$$F = \frac{6\pi\eta r v}{1 - \frac{9}{16}(a/h) + \frac{1}{8}(a/h)^3 - \frac{45}{256}(a/h)^4 - \frac{1}{16}(a/h)^5 + \mathcal{O}((a/h)^6)} \tag{2.26}$$

Similarly, when moving the bead perpendicular to a surface, a correction factor λ with $F = 6\pi\eta r v\lambda$ is introduced, with[38]

$$\begin{aligned} \lambda &= \frac{4}{3}\sinh\alpha \\ &\quad \cdot \sum_{n=1}^{\infty} \frac{n(n+1)}{(2n-1)(2n+3)} \left(\frac{2\sinh((2n+1)\alpha) + (2n+1)\sinh 2\alpha}{4\sinh^2((n+\frac{1}{2})\alpha) - (2n+1)^2\sinh^2\alpha} - 1 \right) \end{aligned} \tag{2.27}$$

In this equation $\alpha := \operatorname{arccosh}(h/r)$ with the bead radius r and the distance between bead centre and surface h. The correction factor λ is plotted in fig. 2.12.

In practice, the bead is moved back and forth between two points at a speed corresponding to a force of 5 pN or 10 pN (or both). It is usually sufficient to estimate the conversion factor between measured data (voltage, size change, ...) and force, check by moving the bead back and forth a few times again and repeating as necessary.

The advantages of the Stokes method are it's speed, intuitiveness and that it is performed *in real time*, i. e. it's results are available immediately and not only after (sometimes extensive) calculations.

However, the bead needs to be moved, potentially leading to a few problems: First and foremost, it is very easy to accidentally trap another bead or dirt in addition to the bead currently being calibrated. This renders the currently trapped bead useless. Furthermore, a typical movement for 10 pN takes only about 75 ms for axial forces, due to the limited piezo range. Slow data rates, primarily from the piezo itself, thus severely limit the amount of usable data. Additionally, on a more hypothetical note, the method relies on correctly calibrated piezos. However, calibration performed on an approximately 10 years old piezo stage showed accuracy within 1 %. Therefore, at least this concern can be neglected.

Overall, I am certain that the calibration error introduced by this method is less than 5 %, given that calibration is performed far away from a surface.

2.6.2. Power Spectral Density (PSD) analysis

In contrast to Stokes based calibration protocols, the analysis of the PSD does not require movement of the bead apart from that induced by Brownian motion. Since Brownian motion is a fundamental principle of thermodynamics, it is obvious that it

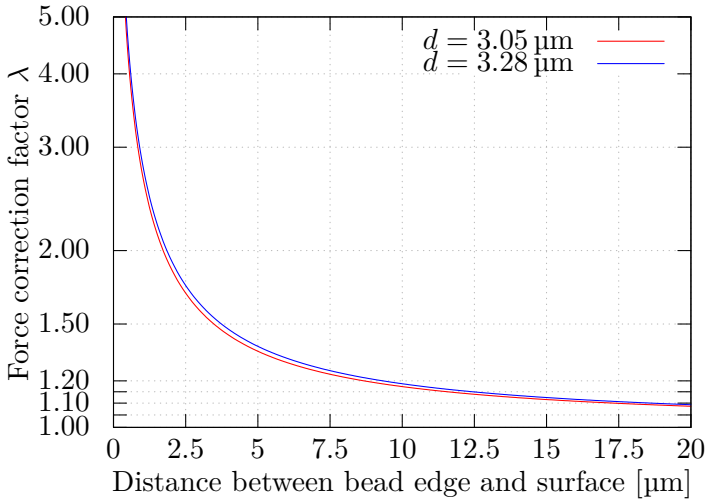

Fig. 2.12.: Correction factor for movement perpendicular to a surface for 3.05 µm and 3.28 µm beads. Values are calculated up to the 100th term with Gnuplot 5.0

should be utilised for calibration. The basis of such a calibration is the description of the bead movement by the Langevin equation, as shown in section 2.2.6.

2.6.2.1. Fourier transformation

As seen before, Fourier transformation of the Langevin equation leads to the power spectrum, given as

$$P(f) = \frac{k_B T}{2\pi^2 \gamma (f^2 + f_c^2)} \tag{2.28}$$

with the corner frequency $f_c = k/2\pi\gamma$.

The power spectrum of a trapped bead is easily obtained. Calibration therefore simply is a fit of equation 2.28.

However, this form of the power spectrum assumes for the sampling rate f_s that $f_s \gg f_c$. In a typical setup f_c is in the range of 100 Hz. For scattered light analysis, we achieve $f_s = 100\,000$ Hz and thus $f_s \gg f_c$. For video-based force detection however, in our setup $f_s = 120$ Hz. Therefore, low pass corrections must be introduced.

Assuming that the sampling frequency is the inverse of the shutter time τ_s, the resulting image is an average between two sampling points. For ease of mathematics, I assume that the measured data (be it position or bead size) x_i from frame i at time t_i is given as

$$x_i = \frac{1}{\tau_s} \int_{t_i - \tau_s/2}^{t_i + \tau_s/2} x(t)\ dt \tag{2.29}$$

Using a boxcar function, this can be simplified as the convolution

$$x_i = [x * \Pi_{\tau_s}](t_i) \qquad \Pi_{\tau_s}(t) = \begin{cases} 1/\tau_s & \text{if } |t| < \tau_s/2 \\ 0 & \text{otherwise} \end{cases} \tag{2.30}$$

In such a case, also called *aliasing*, the low-pass correction yields[25]:

$$P^*(f) = \frac{2k_B T\gamma}{k^3} \left(k + \frac{2\gamma f_s \sin^2\left(\frac{\pi f}{f_s}\right) \sinh\left(\frac{k}{\gamma f_s}\right)}{\cos\left(\frac{2\pi f}{f_s}\right) - \cosh\left(\frac{k}{\gamma f_s}\right)} \right) \tag{2.31}$$

The effects of the low pass correction are illustrated in fig. 2.13.

In addition to the necessary low pass corrections, fitting itself proves to be difficult due to the low sampling rate. Fig. 2.14 shows fourier-transformed data from video-based analysis. The low pass-corrected spectrum was fitted to the data with Origin and Gnuplot with the same starting values. It is not directly obvious which fit is better. However, the results vary by 15 %.

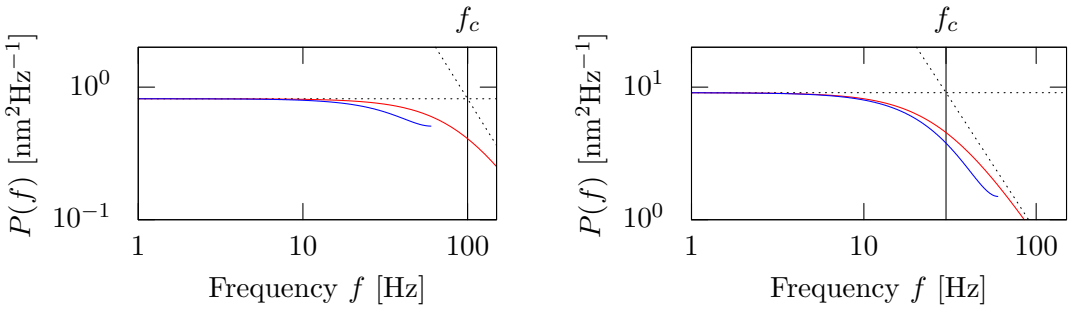

(a) $f_c = 100\,\mathrm{Hz}$ (b) $f_c = 30\,\mathrm{Hz}$

Fig. 2.13.: Exemplary differences between the PSD with (blue) and without (red) low pass correction (sampling frequency $f_s = 120\,\mathrm{Hz}$)

Therefore, whilst fitting the power spectrum is perfectly suitable for scattered light based force analysis, it is unsuited for video-based force analysis or other methods providing only low sampling rate.

2.6.2.2. Allan variance

In contrast to classical power spectrum analysis, Allan variance is perfectly suited for the analysis of low frequency signals. It is defined as one half times the variance of the averaged difference between two consecutive local averaged position samples[39]:

$$\sigma_A^2(\tau) = \frac{1}{2}\left\langle (\bar{x}_{\tau,j+1} - \bar{x}_{\tau,j})^2 \right\rangle \qquad \bar{x}_{\tau,j} = \frac{1}{\tau}\int_{\tau(j-\frac{1}{2})}^{\tau(j+\frac{1}{2})} x(t)dt = [x * \Pi_\tau](j\tau) \tag{2.32}$$

Comparison of eq. 2.32 with eq. 2.30 strongly suggests that Allan variance is inherently suited for power spectral analysis of video-based and other aliased signals.

Since the underlying process, Brownian motion, is stationary, the following relation holds true:

$$\langle \bar{x}_\tau^2 \rangle := \langle \bar{x}_{\tau,j}^2 \rangle = \langle \bar{x}_{\tau,j+1}^2 \rangle \tag{2.33}$$

This can be used to derive the relationship between Allan variance and variance and autocorrelation:

$$\sigma_A^2(\tau) = \langle \bar{x}_\tau^2 \rangle - \langle \bar{x}_{\tau,j+1}\bar{x}_{\tau,j} \rangle \tag{2.34}$$

The Wiener-Kinchin theorem[40] can then be used to relate the Allan variance to the PSD[41]:

$$\sigma_A^2(\tau) = \int_{-\infty}^{\infty} \frac{4\sin^4(\pi f\tau)P(f)}{(\pi f\tau)^2} df \tag{2.35}$$

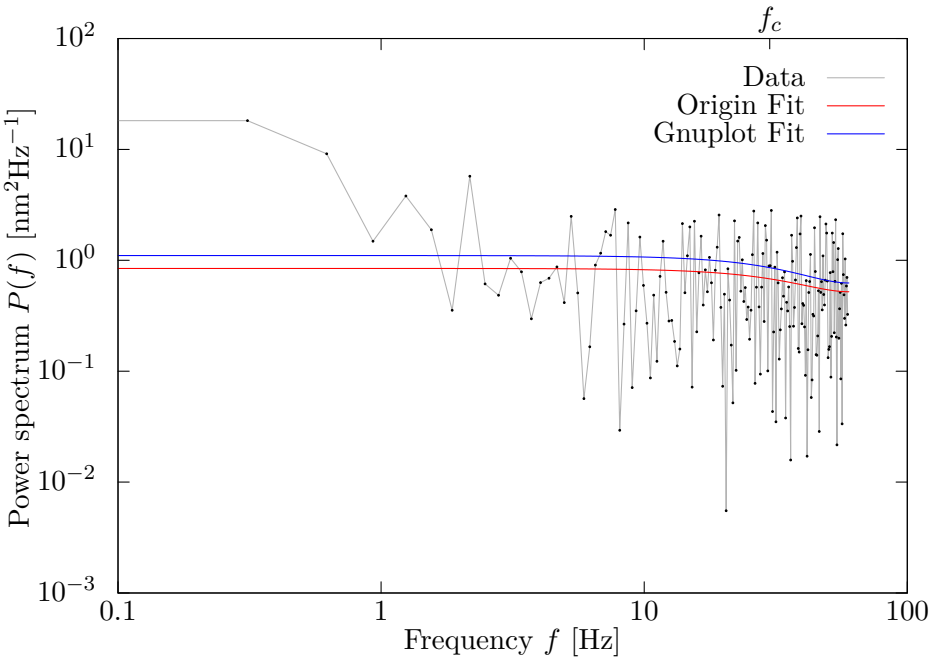

Fig. 2.14.: Example of two Lorentzian fits to Fourier-transformed video-based data.

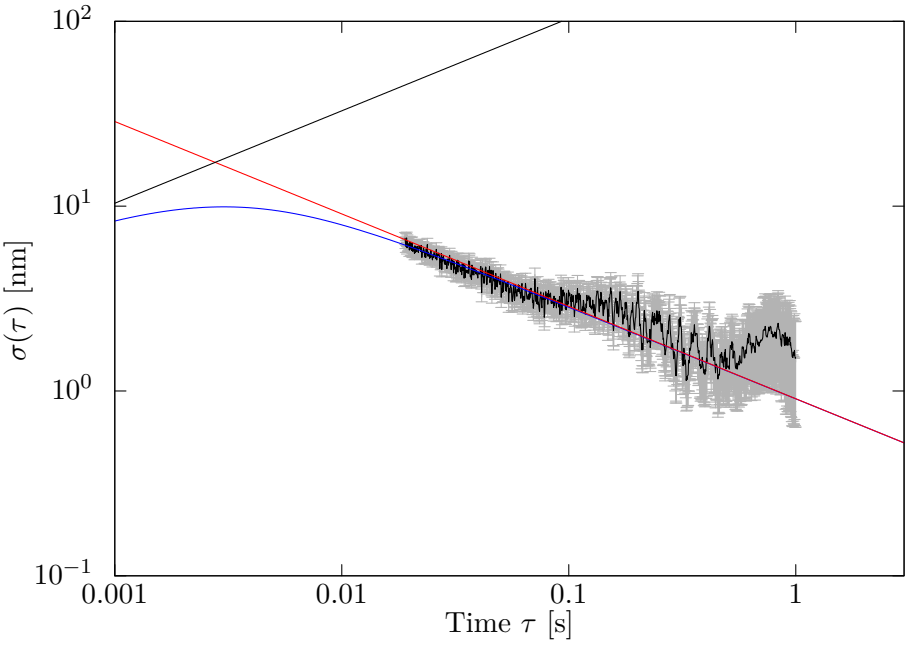

Fig. 2.15.: Exemplary Allan deviation fit. The Allan deviation of the data (converted to real-world units) is shown in black with error bars in grey, the fit is shown in blue and the approximation according to eq. 2.37 is shown in red

which, with $P(f)$ from eq. 2.28 gives us

$$\sigma_A^2(\tau) = \frac{2k_BT\gamma}{k^2\tau}\left(1 + \frac{2\gamma}{k\tau}\,\mathrm{e}^{\frac{-k\tau}{\gamma}} - \frac{\gamma}{2k\tau}\,\mathrm{e}^{\frac{-2k\tau}{\gamma}} - \frac{3\gamma}{2k\tau}\right) \tag{2.36}$$

Here, a critical time τ_c can be defined as $\tau_c = \gamma/k = 1/2\pi f_c$. For times $\tau \gg \tau_c$, which for video-based analysis is almost always given, the bracket becomes 1 and the Allan deviation (the square root of the Allan variance) reduces to[25]

$$\sigma_A(\tau) = \frac{1}{k}\sqrt{\frac{2k_BT\gamma}{\tau}} \tag{2.37}$$

Fitting $\sigma_A(\tau)/\beta$, which is the Allan deviation in camera units, to the data then gives us the calibration factor $k\beta$.

An exemplary Allan fit using the same data as in fig. 2.14 is shown in fig. 2.15. Obviously, the data can be described more precise by Allan deviation than by the Lorentzian fit of the Fourier transformation.

To sum up, as Allan variance allows for very precise calibrations without the need to move the bead and as it is directly suitable for low sampling rates, it is the favoured method of calibration. However, calculation is rather complex and cannot be done in real time. In practise, this means that around 5 s of data need to be acquired, whose calculation takes about another 5 s. Furthermore, a description of the long term drift of the system is easily available.

3. DNA translocation through solid-state nanopores

The mechanics of the translocation of macromolecules through nanopores is one of the fundamental research fields in biophysics. Potential applications for transport through nanopores include separation, diagnostics and biosensing. The study of translocation behaviour of DNA is of particular interest. DNA serves as the primary sample system within single molecule analysis in general and optical tweezers in particular. Solid state nanopores offer the advantages of tuneablility in both diameter and thickness, versatility to a wide range of environmental conditions, stability and integrability into microelectronic devices.

It should be noted that the term *translocation* is used here in the meaning of controlled translocation or stalled translocation, as is usual for experiments involving optical tweezers[1,13,29,42–44]. The DNA in threaded into the nanopore, the translocation is halted by trapping a bead attached to one end of the DNA, and then the DNA is slowly pulled out of the pore. This pulling out process is meant when speaking of translocation in conjunction with optical tweezers and nanopores.

3.1. DNA

DNA, deoxyribonucleic acid, is a macromolecule that acts as the carrier of the genetic information of all organisms and many viruses. It is a polymer of nucleotides, as illustrated in fig. 3.1a. They consist of the sugar 2-deoxyribose and are joined by phosphate groups forming phosphodiester bonds between the 5'- and 3'-C atom of two adjacent sugars. Attached to the 1'-C atom is the nitrogen atom of a nucleobase. Possible nucleobases are the purines adenine (A) and guanine (G), and the pyrimidines cytosine (C) and thymine (T). The order of those bases encodes the genetic information.

Two pairs of anti-parallel nucleotide strands are forming the double-helical dsDNA, which is illustrated in fig. 3.1b. Both strands are held together by hydrogen bonds, where A only binds to T via two hydrogen bonds and G only to C via three hydrogen bonds. Therefore, the two strands are complimentary to each other.

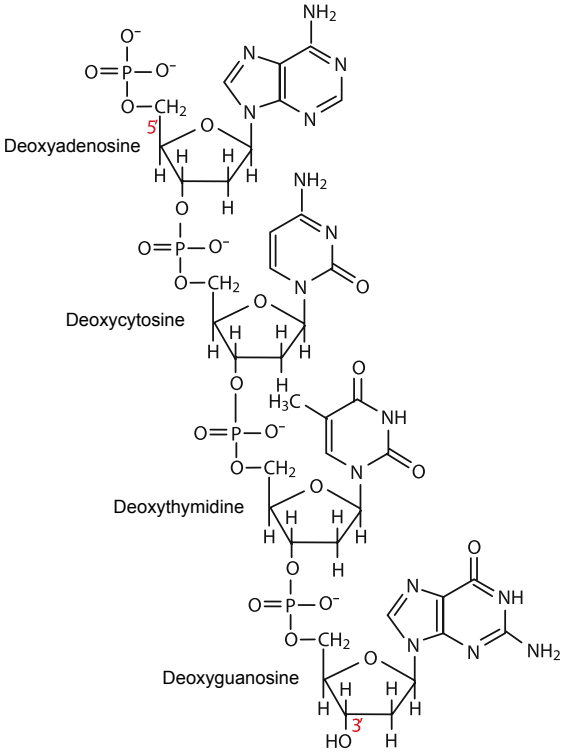

(a) The four bases in a single strand of DNA

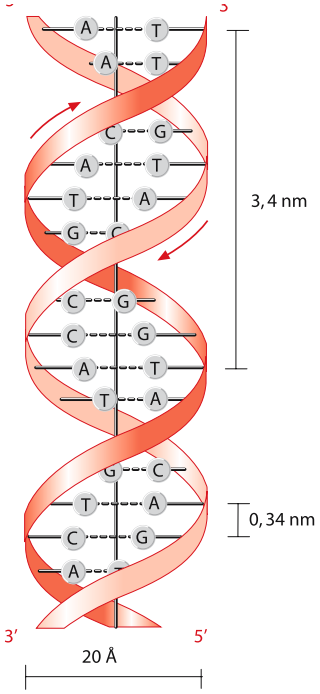

(b) Double-helical structure of B-DNA

Fig. 3.1.: Components and structure of DNA, from [45]

In physiological conditions, dsDNA forms a right-winded double helix called B-DNA. In this form, neighbouring base pairs are distanced 0.34 nm apart from each other and turned by 35.9°. The helix has a diameter of 2.37 nm.

Without applied force, DNA curls itself into a small bundle due to entropic forces. dsDNA is best described by the *worm like chain* (WLC) model[46,47]. It can be considered as a flexible rod, with the *persistence length* l_p the characteristic length for which the molecule has no significant curvature. It is defined as

$$l_p = \frac{\kappa}{k_B T} \tag{3.1}$$

with the bending stiffness κ. For dsDNA in physiological conditions, $l_p = (53 \pm 2)\,\text{nm}$.

The mean squared end to end distance $\langle L^2 \rangle$ for a molecule with contour length L_0 can be calculated as

$$\langle L^2 \rangle = \int_0^{L_0} ds \int_0^{L_0} ds' \, \exp\left(\frac{-|s-s'|}{l_p}\right) = 2 l_p L_0 - 2 l_p^2 \left(1 - \exp\left(-\frac{L_0}{l_p}\right)\right) \tag{3.2}$$

The force required to stretch dsDNA to length x can be modelled as[11]:

$$F(x) = \frac{k_B T}{l_p} \left(\frac{1}{4(1 - x/L_0)^2} - \frac{1}{4} + \frac{x}{L_0} \right) \tag{3.3}$$

For low forces ($F < 20\,\mathrm{pN}$), this model holds true. For larger forces ($F \approx 65\,\mathrm{pN}$), the double strand begins to melt, giving rise to a large elongation without significant more applied force. Once the strand is completely molten, resulting in two parallel ssDNA strands, the force rises again exponentially, until the strands rip apart.

In all our experiments, the dsDNA of the bacteriophage λ of *E. coli* with a contour length of $L_0 = 16.5\,\mu\mathrm{m}$ (corresponding to the 48 502 bp in the DNA) is used. It is biotinylated on one end, allowing for it to specifically bind to the streptavidin coated polystyrene beads.

3.1.1. DNA sequencing

DNA sequencing is the process of reading out the sequence of bases in a given strand of DNA. Sequencing is performed by utilising a variety of different techniques, which are described in detail elsewhere[48]. Common to all methods is a limitation of the maximum read length in the range of 1000 bp[49]. Since typical genomes are much larger (e. g. 48.5 kbp for the viral DNA of bacteriophage λ or 3.2 Gbp for the homan genome), the resulting short pieces have to be assembled. Since many genomes contain a large amount of repeating sequences, this assembly step is the most challenging in DNA sequencing nowadays[50]. In *de novo* genome assembly, this challenge is even more prominent since there is no reference to compare against.

DNA sequencing by nanopores could enable the sequencing of arbitrary long DNA strands[2], which would remove the need for assembly or at least make it significantly easier.

3.2. Translocation theory

Translocation of DNA through nanopores is a complex process with theoretical understanding currently still developing[51,52]. However, as with all hydrodynamic effects, the governing equations are the Navier-Stokes equations, which describe the general motion of viscous fluids.

The derivation of the Navier-Stokes equations is explained in detail in most theoretical books covering hydrodynamics (e. g. Landau & Lifschitz[24], §15). In short, the hydrodynamic continuity equation and Euler equations are inserted into a momentum

current equation, resulting in a momentum current density tensor. This tensor needs to be adjusted by introducing an additional summand, the viscous stress tensor, which can be derived from some basic principles: It has to be dependent only, and only linearly, from the first derivations of the velocity field (and therefore vanish for constant velocities), it has to vanish for vortex movements ($\vec{v} = \vec{\omega} \times \vec{r}$), and it has to account for an isotropic fluid. This results in the following form for the viscous stress tensor:

$$\sigma'_{ik} = \eta \left(\frac{\partial v_i}{\partial x_k} + \frac{\partial v_k}{\partial x_i} - \frac{2}{3}\delta_{ik} \frac{\partial v_l}{\partial x_l} \right) + \xi \delta_{ik} \frac{\partial v_l}{\partial x_l} \tag{3.4}$$

As a final results, one gets the Navier-Stokes equation describing the motion of a viscous fluid with applied external force $\vec{F_{\text{ext}}}$ as follows:

$$\rho \left(\frac{\partial \vec{v}}{\partial t} + (\vec{v}\vec{\nabla})\vec{v} \right) = -\vec{\nabla}\vec{p} + \eta \Delta \vec{v} + \left(\xi + \frac{\eta}{3} \right) \vec{\nabla}(\vec{\nabla}\vec{v}) + \vec{F_{\text{ext}}} \tag{3.5}$$

This equation proves to be difficult for two reasons: Firstly, the external forces arise from a multitude of sources, often with non-trivial forms. Secondly, even without external forces, the Navier-Stokes equations are both mathematically and physically challenging. On the mathematical front, it remains still unproven whether smooth and globally defined solutions exist for all initial velocity fields at all. This problem is one of the seven famous Millenium Prize Problems, six of which (including the Navier-Stokes existence and smoothness problem) remain unsolved at the time I write this thesis. Physically, this relates especially to our still very limited understanding of the internal structure of turbulent flow.

Therefore, for most practical cases, numerical solutions are gained from simulations. In our case of a DNA moledule passing through a nanopore, the main external driving forces are electrophoresis on the DNA and electroosmotic flow of the surrounding electrolyte fluid. Additional forces from a variety of sources like self-energy, concentration polarization, counterion pressure and electrokinesis have to be considered[51]. The electric potential within the electrolyte solution is subject to Poisson's equation

$$\epsilon \Delta \Psi(x) = -F_c(c_+(x) - c_-(x)) \tag{3.6}$$

with ion concentrations $c_\pm(x)$, Faraday's constant F_c and the solution's permittivity ϵ. Furthermore, the Nernst-Planck equation describes the flux densities of the ions as

$$J_\pm(x) = c_\pm(x)v(x) + \mu_\pm c_\pm(x)E(x) - D_\pm \nabla c_\pm(x) \tag{3.7}$$

with the ion diffusion coefficients $D_\pm$ and their mobilities $\mu_\pm$.

Those two equations are coupled with the Navier-Stokes equations, from which the convective acceleration term can be neglected due to the low Reynolds numbers encountered. Together, they form a coupled framework which can be used to either simulate the forces acting on the DNA during translocation through a well-known nanopore. Of course, a large number of boundary conditions as well as some special assumptions and simplifications are used to obtain meaningful data in a reasonable amount of time. However, those are beyond the scope of this thesis and have been described in the original papers[51–53]. Suffice to say that when modelling the DNA as a simple, homogeneously charged rod, a no-slip condition can *not* be imposed a priori. The no-slip condition is usually applied to microfluidical problems and states that the fluid at a surface does not move parallel relative to the surface. Comparison of simulated data with the large data base for silicon nitride nanopores gathered in our group reveals that in fact, a slip length has to be introduced. The results are presented briefly in section 4.4.3.

3.3. Electric current analysis

In addition to force measurements, nanopores also offer the possibility to measure the electric current across the nanopore if a voltage is applied, which is always the case for translocation experiments. This works as a Coulter counter[54], a device that is commonly used to measure and classify the amount and size of cells in a sample, e. g. red and white blood cells. As a particle passes the nanopore, it briefly obstructs the conductivity, leading to a current peak. The current data is particularly interesting since the ionic current through a nanopore blocked by DNA is dependent on the specific bases within the nanopore[2], possibly enabling DNA sequencing[55].

In the context of DNA translocation through nanopores, the direction of the current peak is not necessarily downwards. Since the surface of DNA is charged, depending on the used buffer concentrations, it is well possible that a passing DNA induces a momentarily increase in the current.

In addition to being used as a Coulter counter, measuring the electrical current through the nanopore also offers a way to indirectly determine the size of the nanopore. Describing both the nanopore and the funnel leading to the membrane as cylindrical, which is a reasonable approximation for the nanopore and a rather rough one for the funnel, the resistance can be described[56] as a function of the actual pore resistance R_P,

the access resistance at each side of the pore* R_{AP}, the resistance of the cylindrical funnel R_C and its access resistance R_{AC} (just on one side). Assuming a series circuit, adding these resistances gives the total resistance[56]

$$R = R_P + 2R_{AP} + R_C + R_{AC} = \frac{\rho l_p}{\pi r_p^2} + \frac{\rho}{2r_p} + \frac{\rho l_c}{\pi r_c^2} + \frac{\rho}{4r_c} \tag{3.8}$$

with the specific resistance ρ of the buffer solution, the membrane thickness l_p, the pore radius r_p, the depth of the funnel l_c and its radius r_c.

Since the size of the funnel is usually three orders of magnitude larger than the pore size, its resistance contribution can be neglected, which also solves the problem of it being based on a rather rough approximation. The resulting resistance is then

$$R = \frac{\rho l_p}{\pi r_p^2} + \frac{\rho}{2r_p} = \frac{\rho d}{\pi r^2} + \frac{\rho}{2r} \tag{3.9}$$

This can be rewritten to give the diameter of a pore with known resistance as

$$d = 2r = 2\left(\frac{\rho}{4R} + \sqrt{\left(\frac{\rho}{4R}\right)^2 + \frac{\rho d}{\pi R}}\right) \tag{3.10}$$

3.4. Nanopore preparation

Even though I use a range of nanopore materials, the preparation process is always very similar. I will therefore present the general preparation here and only add specific instructions, annotations or deviations from this workflow in the specific material sections.

3.4.1. Chip setup

The setup of the chip containing the nanopore varies in details, as multiple chip batches are in use. Here, I describe the chip I used for all experiments with nanopores in membranes I transferred onto the chip myself.

Rectangular silicon chips with clipped edges fitting into a 3 mm circle (commonly called a TEM frame size) containing a membrane window are used. The chips are illustrated in fig. 3.2. The frame of the chip has a thickness of 200 µm with a rectangular funnel etched into the centre of the chip. This funnel leads to a 500 nm thick silicon

*Since the pore opening is very small, this additional access resistance has to be taken into account. It is the resistance along convergent paths from the buffer to the pore opening and equals $R_{AP} = \frac{\rho}{4r_p}$. A more detailed explanation is available in [57, p. 352]

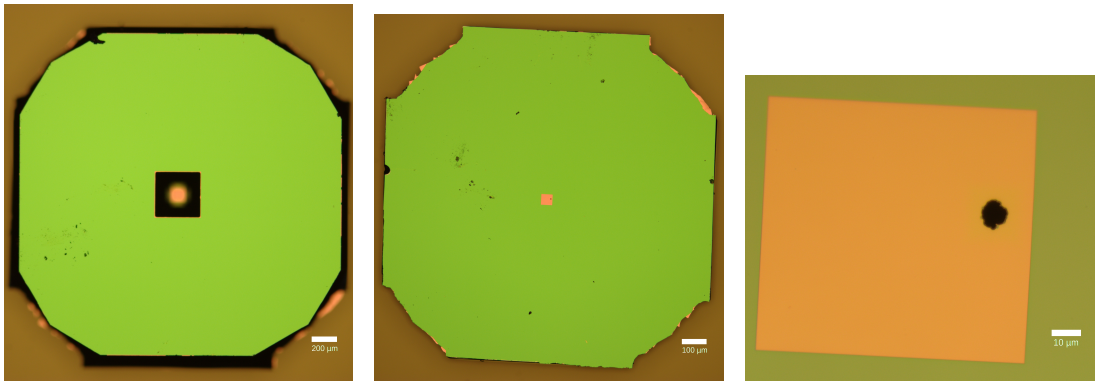

(a) funnel side up; scalebar 200 µm (b) window side up; scalebar 200 µm (c) detail view of the hole; scalebar 10 µm

Fig. 3.2.: Reflected-light microscope images of a typical chip. Here, the silicon appears green, the silicon nitride membrane appears pink and the hole in the membrane is black

nitride membrane window of 70 µm × 70 µm. This membrane contains a, sometimes irregularly formed, hole with approx. 7 µm diameter.

For measurements with nanopores in silicon nitride, the chips contain a thinner silicon nitride membrane (typically 20 nm) without a prefabricated hole.

3.4.2. Mechanical exfoliation

Single layers of solid state materials are used as a nanopore material. However, for our purposes only bulk material is available commercially. Therefore, single layers have to be extracted somehow.

Graphene as a model single layer material was first produced in 2004 by K. Novoselov, A. Geim et al.[58], leading to the Nobel Prize in Physics being awarded to Gaim and Novoselov in 2010. Their production method is as simple as it is ingenious. To quote:

> Our graphene films were prepared by mechanical exfoliation (repeated peeling) of small mesas of highly oriented pyrolytic graphite.[58]

For exfoliation, first adhesive nitto tape is placed on the bulk material. I press the nitto tape onto the material with one thumb at low force for approximately one second. The nitto tape is then slowly pealed away from the material. Afterwards, I fold the nitto tape near the edge of the material pealed from the bulk block, therefore overlapping a portion of the material and blank nitto tape with the material. This

process is repeated eight to ten times, creating a patch of approximately one by three centimetre size.

I then placed the nitto tape on a piece of silicon wafer with a 90 nm silicon oxide (SiO_2) layer (MTI Corporation, CA), so that the patch is in contact with the wafer. I press the tape with both thumbs at high force for approximately two seconds to the wafer. Afterwards, I slowly remove the nitto tape from the wafer. For documentation, I place the nitto tape on a piece of paper (material side down) and mark the position of the chip (which is still visible as a faint outline for a few minutes) on the backside of the tape with a marker. It should be noted that the silicon wafer is reusable. Immediately prior to use, I clean it for 10 min in acetone in an ultrasonic bath. Removal from the acetone has to be done very slowly, as otherwise blue stains remain on the silicon. I found it helpful to place the wafer in isopropyl alcohol for a few seconds after the acetone bath, since this seems to remove the typical acetone stains.

It should be noted that this method is not limited to graphene but suitable to a large number of layered materials, as I show in this work.

3.4.3. Flake detection

The silicon wafer now contains a large number of flakes of varying size and thickness. Some thick and large flakes are even visible to the naked eye. However, we are interested in small monolayered flakes which are not as easily accessible.

For detection of single layered flakes of material on a substrate and especially for measuring the thickness of the flakes and thus verifying the number of layers, a multitude of methods can be employed. One notable method is *atomic force microscopy* (AFM), which allows the direct measurement of the thickness of a flake by scanning the surface of the substrate with a piezo-controlled cantilever, but is limited by its very low throughput.

Another method that is primarily used with graphene is localised Raman spectroscopy (also called *Raman microscopy*). Here, inelastic scattering of a laser beam on the material is analysed, with the Rayleigh scattering filtered out. The resulting Raman shift, a shift in the frequency of the reflected light, is caused by inelastic scattering as the photon couples with molecular oscillations, e. g. vibrational or electrical. This method provides a fingerprint of a material. Due to the special electronic properties of graphene, a distinct Raman peak is obtained, which shifts depending on the thickness of the graphene, thus allowing the identification of monolayers[59]. The problem with this method however is the necessity for a complicated Raman microscopy setup, with typical costs in the range of a quarter million Euro. Fortunately, for our purposes, a

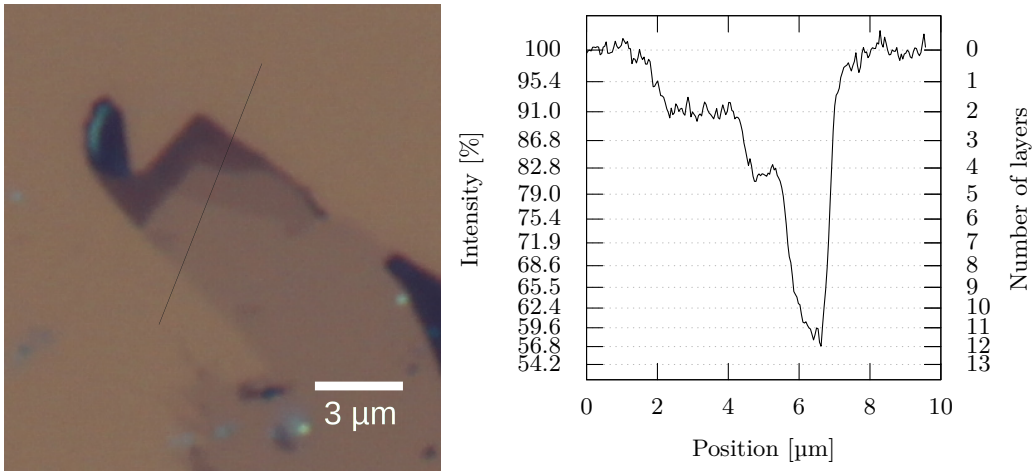

(a) Reflecting microscopy image of a wafer with graphene

(b) Intensity profile along the marked line

Fig. 3.3.: Graphene detection by opacity analysis. Note that what appears to be a monolayer in the image is actually a bilayer.

simple and cheap optical microscopy based method can be employed.

The first possible method to detect single layers of material in an optical microscope is by analysing the opacity of those layers. Whilst one might expect the opacity of single layer materials to be negligible, this is not the case for all materials. For graphene, theoretical predictions and experimental confirmation show an opacity of[60]

$$(1 - T) = 1 - (1 + \frac{1}{2}\pi\alpha)^{-2} \approx \pi\alpha = 2.3\,\% \tag{3.11}$$

per layer, with the fine structure constant $\alpha \approx 1/137$. Therefore, in a reflected-light microscope, a single layer of graphene appears 4.6 % darker than the substrate, a double layer 9.2 % darker, and so on. This can be reproduced, as illustrated in fig. 3.3. For detection of graphene, it would therefore be sufficient to scan a substrate and simply look for distinct patches of reduced brightness. However, the following second direct optical method proves to be even more promising.

As a second possibility, shifts in the colour of reflected light from the underlying silicon wafer can be detected[58]. Due to the only 90 nm thick silicon oxide coating of the wafer, it normally appears violet-blue. Minute changes to the thickness of the coating layer, e. g. by placing an additional layer of graphene or another material on the wafer result in noticeable changes in colour, even if the additional material is normally transparent or nearly transparent.

Detection of suitable flakes consisting of single, double or triple layers and able to cover a hole of at least 7 µm diameter is therefore performed by scanning the wafer in a reflected-light microscope (Olympus BX51, Olympus, Japan). Suitable flakes are marked by placing one dot with a marker onto the wafer on either side of the flake.

Since manual scanning of a 1 cm × 1 cm wafer in reasonable magnification (at least 10x for experienced users, 20x magnification is recommended) takes at least one hour and is very tiring to the eyes, I developed an automated flake detection system, using a DSR (EOS 600D, Canon, Japan), a two-axis stage and a LabView control program. It is described in detail in appendix A. This system scans the wafer, creating a giant image (roughly 540 million pixel / 1.5 GB per square centimeter) and searches that image for flakes with specific colour and minimal size. With it, after initial focus calibration and selecting the region of interest, scanning is performed automatically without any necessary user intervention. After the scanning process and subsequent flake detection is finished, an overview image with marked locations of possibly usable flakes is presented. The user can select any point in the overview image, which leads to a corresponding movement of the stage so that the selected point is centred in the field of view. Usually, the user then verifies the usability of the flake manually in larger magnification, notes the coordinates and proceeds with the next flake location. In the end, as with manual search, usable flake positions are marked on the wafer.

3.4.4. Transfer

Fig. 3.4.: Coated wafer after transfer

At this point, we have a silicon wafer containing a marked, usable flake of our membrane material, which needs to be transferred onto the chip. As a first step, the water reservoir of the transfer apparatus (see fig. 3.5) is completely filled with water and the hydrophobic chip is placed, membrane side up, into the chip holder.

Then, the wafer is coated with a thin layer of cellulose polymer by placing the edge of the wafer vertically into a solution of 30 mg mL^{-1} cellulose acetate butyrate in ethyl acetate in such a way that the marked flake is approximately 3 mm below the surface of the solution and then pulling the wafer slowly out of the solution. The resulting interference pattern of the dried polymer indicates a rise in coating thickness in the uppermost few millimeter, which should be centred on the flake. This positioning is illustrated in fig. 3.4.

A rectangle of 2 mm × 2 mm size centred on the flake is cut into the polymer coating.

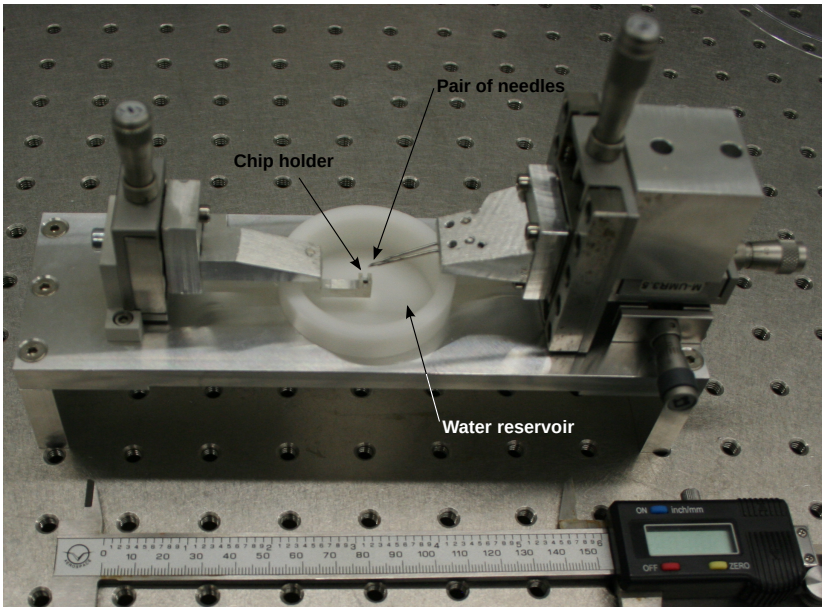

Fig. 3.5.: Transfer apparatus

The wafer is then, at a very shallow angle, lowered into the water reservoir of the transfer apparatus. With careful help with a pair of tweezers, the rectangular patch of polymer detaches from the wafer and swims on the water surface. It is of utmost importance that the polymer does not fold during this step. As soon as it swims on the water surface, it can be easily manoeuvred by dipping the tweezers into the water in front of the polymer patch. Using this technique, the polymer is pulled away from the area of wafer immersion allowing for the wafer to be pulled out of the water without pulling the polymer back onto the wafer.

Next, the whole transfer apparatus is carefully placed onto a reflected-light microscope, which in turn stands on a vibration dampening table. The free-floating polymer patch is then manoeuvred below the pair of needles, which are lowered to trap the patch. In this trapped state, the flake should be in between the two needles. If this is not the case, the process has to be repeated until it is. Then with the two other screw gauges, the flake is placed over the chip. The chip is then slowly raised up towards the water surface. At the same time, the needles need to be slowly moved down (at an approximate ratio of 1:10) to balance the sinking water level. It is very important to not move the needles to far down, pulling the polymer patch under water, and also to not move them to slowly down, since the patch then escapes and the process has to begun anew.

Once the chip is very near the polymer patch (indicated by the chip coming into

focus whilst focused on the patch), the position of the patch is fine tuned again to make sure that the flake is centred over the hole in the chip. Then, the chip is slowly pulled further up. At some point, the chip touches the water surface and thus the patch, the patch adheres to the chip and the water between chip and patch rapidly dries. Then, the water reservoir can be emptied with a syringe. Depending on the size of the patch, potential folds in the patch and luck, the drying process takes between a few minutes and a whole day, during which any movement of the chip and polymer (even by air drafts) is avoided.

Once the chip has completely dried and one has waited 24 hours, the polymer can be removed by placing the chip in ethyl acetate for a few minutes. Upon dipping and leaving the ethyl acetate, the chip should be held vertically.

After removal of the polymer, the chip should be imaged in a reflected-light microscope to make sure that the hole is covered completely and to determine the number of layers of the membrane. Often, what starts out as a triple layer on the wafer ends up as a mono- or bilayer membrane on the chip, which is another reason (apart from yield) why multilayer should not be discarded immediately during the flake detection process.

3.4.5. Pore drilling

Pores are drilled into the membranes by helium ion microscopy. The chip is placed in a helium ion microscope (ORION Plus, Carl Zeiss AG, Germany), which uses positively charged helium ions to image or - if a high localised intensity is applied - drill into the surface. Surface charging is avoided by simultaneously using an electron flood gun.

For drilling pores with a helium ion microscope, three practical modes exist. For larger holes, a circle is drawn with an intense helium ion beam, thus *cutting* the hole. For smaller, rectangular holes, a small region is scanned (e. g. imaged) repeatedly, until the material has been dissipated. Especially for drilling small holes in very thin membranes, simply focussing the ion beam onto a single spot is sufficient. All pores in molybdenum disulphide were drilled in that way. Except for the very thick membrane M4 (approx. 10 layers), the spot was held for 2 min at 0.5 pA. A comparison of the MoS_2 membrane M3 before and after pore drilling is shown in fig. 3.6. For membrane M4, the spot was held for 10 min at 0.5 pA.

For larger holes in thick membranes, simply focussing the beam onto a single spot or regularly scanning the same area is not sufficient. In these cases, the spot is moved slowly in a circular pattern, thus cutting a round hole in the material.

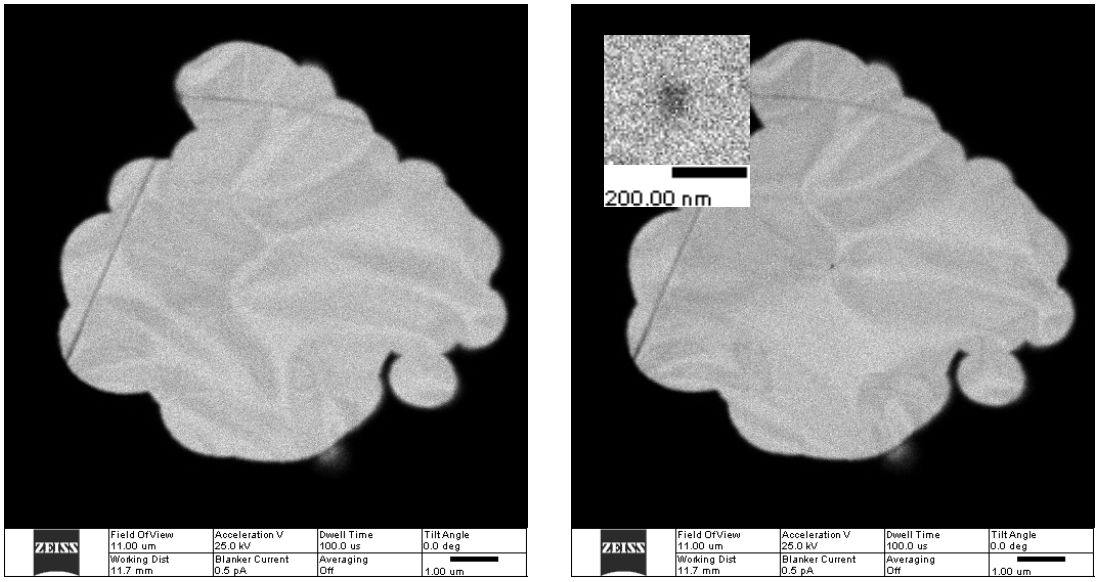

(a) Before (b) After

Fig. 3.6.: Helium ion microscopy images of a MoS_2 membrane (M3) taken before and after the pore was drilled.

3.5. Sample chamber preparation

The layout of the sample chamber is illustrated in fig. 3.7. Its main part consists of PDMS (polydimethylsiloxane), which has to be hydrophilised before use. A cover slip *#1* (24 mm × 60 mm, approx. 0.15 mm thickness) is spincoated with 40 µm of PDMS. A 26 mm × 1 mm strip in the centre is removed, forming a channel with a glass bottom. Additionally, a silanised glass slide is spincoated with 40 µm PDMS as well. Both slide and cover slip are placed for 30 s in an oxygen plasma (nitrogen atmosphere reduced to 8×10^{-3} mbar, afterwards flooded with oxygen to 0.1 mbar with active vacuum pump, ignition via 500 kHz AC between 20 kV to 45 kV).

The sample chamber consists of a metal base with a 0.20 mm deep slot, into which the cover slip is placed. In the PDMS on the object plate, an approx. 50 mm × 20 mm rectangle is cut out, with a centred 1.5 mm diameter hole. The rectangular PDMS patch is then carefully lifted from the object plate with two tweezers, turned upside down (so that the hydrophilized surface points downwards) and placed, with the hole precisely centred, onto the PDMS channel on the cover slip. Then, centred at the ends of the channel, two 3.0 mm diameter holes are created in both layers of PDMS, leading to a channel with two end reservoirs (open to the air) and one hole in the top layer

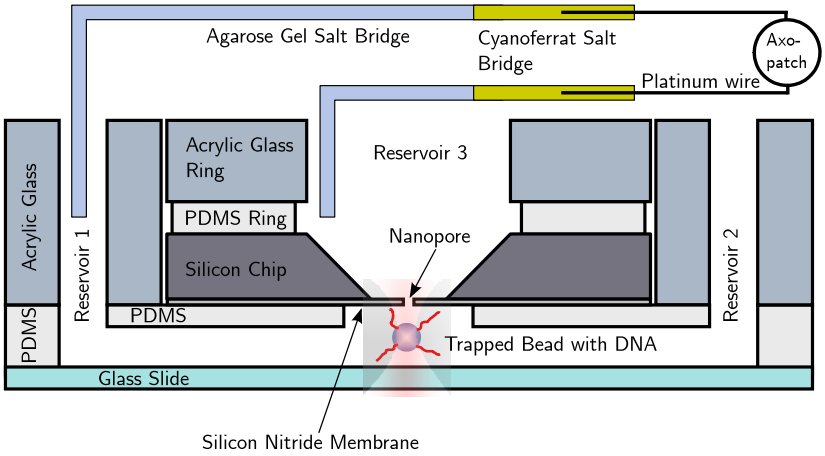

Fig. 3.7.: Schematic layout of the sample chamber

in the centre of the channel. A droplet of filtered, degassed water from the MilliQ reverse osmosis purification unit is placed onto that centre hole, which should lead to the water immediately travelling to the end reservoirs, filling the channel completely without any included air. Making sure not to introduce any air into the ends of the channel, droplets are then placed onto both end reservoirs.

Depending on the sensitivity of the used chip, the following step can either be performed inside the water droplets (leading to potentially high capillary forces and pressure gradients), or with the whole sample chamber completely submerged in water. For all nanopore materials except silicon nitride, the latter method was used.

The chip is now placed centred over the middle hole. Then, the first part of the acryllic glass cover is placed onto the channel, leaving three large reservoirs open to the air. Onto the centre reservoir (containing the chip), a second piece of acryllic glass is placed. This piece presses the chip onto the channel via a 0.62 mm thick PDMS seal ring (1.5 mm inner diameter, 3.0 mm outer diameter), sealing the system in such a way that any particles, ions etc. travelling from the outer reservoirs to the inner reservoir must cross the nanopore.

Finally, the water is replaced by our filtered and degassed buffer solution containing 20 mM KCl and 2 mM Tris/HCl at pH 8.0.

4. Silicon nitride

4.1. Introduction

Silicon nitride (in principle any material with the formula Si_xN_y, here specifically Si_3N_4) is a ceramic with a high melting point (around 1900 °C) and mostly chemically inert. It was first synthesised in 1857[61] by heating silicon in ammonia atmosphere, a method that is still used today for CVD. Being an insulator and mostly inert, it is used in microelectronics as an insulating layer in microchip fabrication. Additionally, it is used in a wide range of areas in which high temperatures are encountered, e. g. in combustion engines and in bearings. Orthopaedic applications are another use case for silicon nitride ceramics.

In research, silicon nitride is well known as a material for AFM cantilevers due to its elastic properties, and as a carrier membrane for transmission electron microscopy.

For DNA translocation experiments with optical tweezers, silicon nitride is the standard nanopore material, due to its ease of use and it being commercially available. In Bielefeld, silicon nitride nanopores have been used almost exclusively until now. Therefore, this chapter serves two purposes: On the one hand, it presents the current standard material to enable a comparative analysis of the new materials presented in this thesis. On the other hand, very small nanopores are analysed.

4.2. Preparation

Silicon nitride membranes are readily available from a number of commercial supplies. For our purposes, chips with a 20 nm thick silicon nitride membrane (according to section 3.4.1) were purchased from Silson Ltd. (Northampton, UK) and from SPI Supplies / Structure Probe, Inc. (West Chester, PA). Some measurements were also performed with 50 nm thick membranes from the same suppliers and with 10 nm thick membranes from Norcada Inc. (Edmonton, Canada). Preparation of the nanopores was performed as outlined in section 3.4.5.

4.3. Lipid coating

Optionally, the silicon nitride membrane can be coated with a lipid bilayer. The preparation has been described in detail elsewhere[51,56] and shall be described only briefly here: Small unilamellar vesicles (SUV) consisting of 99.2 mol % POPC (1-Palmitoyl-2-oleoyl-*sn*-glycero-3-phosphocholine) and 0.8 mol % DOPE (1,2-Dioleoyl-*sn*-glycero-3-phosphoethanolamine) are created using a rotary evaporator in a buffer with 2 mM concentration. The coating process itself is done in the fully assembled sample chamber. The chamber is first rinsed with the buffer used for the preparation of the SUV. Then the buffer containing the SUV is inserted into the bottom channel. Upon contact with the hydrophilic membrane, the SUV burst on the surface and merge to a bilayer coating the surfaces. The nanopore itself is not spanned by the bilayer, but its inner sides are coated as well. After about 15 min, the channel is rinsed with deionised water. Using fluorescent labelled DOPE in the production of the SUV allows for the inspection of the coating by fluorescence microscopy, which shows that both sides of the membrane and the pore itself are coated with a lipid bilayer. Comparing the conductivity of the nanopore prior to coating with the coated nanopore, an increased resistance is observed, which is expected due to the reduced pore size.

4.4. Results

4.4.1. Typical DNA translocation process

A typical DNA translocation measurement through an uncoated silicon nitride membrane is illustrated in fig. 4.1. First, the trapped bead approaches the membrane whilst a transmembrane voltage of 50 mV is applied. At some small distance between bead and membrane, typically in the range of 1 µm to 5 µm, the DNA is pulled into the nanopore. Simultaneously, the measured force jumps from zero to a pore-size and voltage dependent force in the range of a few piconewton. The force is independent of the distance between bead and nanopore, and therefore remains constant until the DNA is threaded out of the pore again.

This threading out does not necessarily happen at the force dependent distance expected from the worm-like chain model as per eq. 3.3. In fact, reaching the full length according to the WLC model is a rare occurrence, as usually the DNA sticks to the bead for a few hundred nanometer, or, as is the case in the illustrated measurement, even multiple micrometer. Theoretically, this could be prevented by modifying the coating of the beads to discourage unspecific binding and by changing the DNA modification

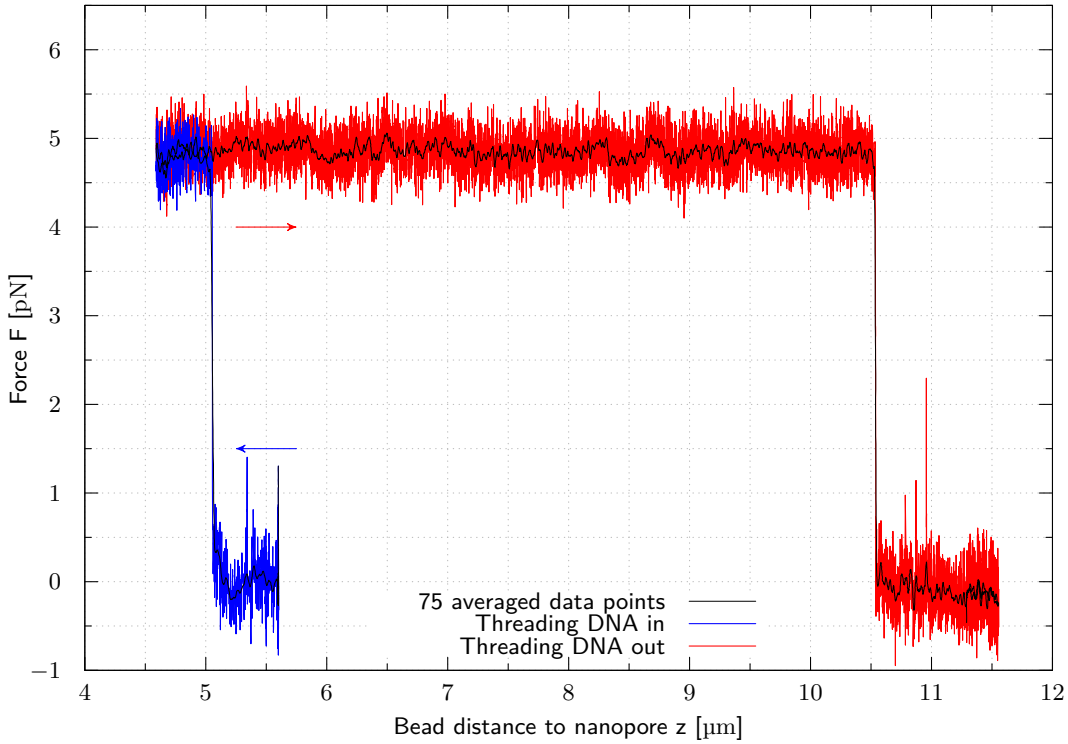

Fig. 4.1.: Typical DNA translocation measurement through a silicon nitride membrane. Pore diameter: 55 nm. Transmembrane voltage: 50 mV

accordingly to recreate a specific binding. However, since there is no direct need to translocate the complete DNA through the pore, the simple biotin-streptavidin system is utilised. If the need to translocate the complete DNA should arise at some point, e. g. for sequencing purposes, one could simply biotinylate the other end of the DNA in a second batch and perform the experiment twice.

Apart from the measured force, such a simple DNA translocation experiment through a thick nanopore for itself usually does not provide much insight. However, it is the basis for all further experiments. Combining the results of multiple experiments with different pore sizes or with modified surfaces, as shown in subsections 4.4.2 and 4.4.3, enables meaningful insights. Also, modifying the DNA itself, e. g. by introducing binding ligands, can lead to new insights with such *simple* experiments[31,62]. And of course thinner and smaller nanopores could result in new findings gained from a single DNA translocation experiment, which is the motivation of this thesis.

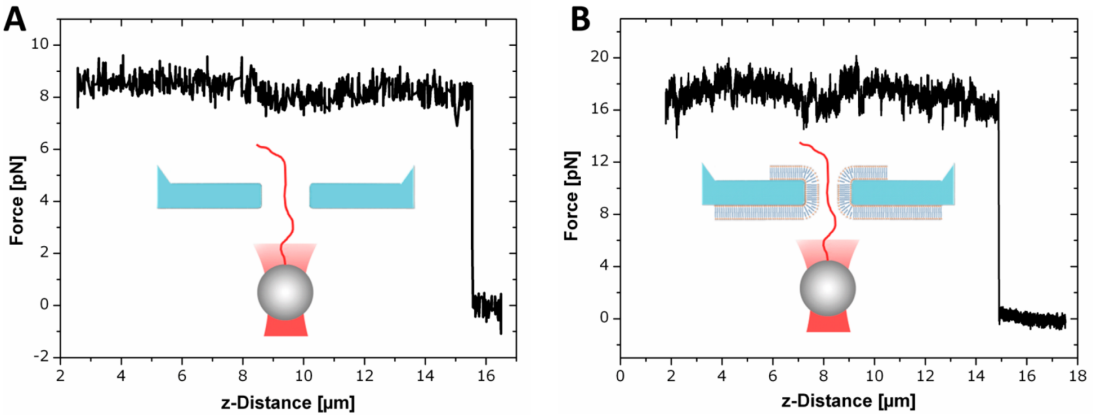

Fig. 4.2.: Typical measurements of DNA translocations through a 41 nm nanopore, both uncoated (A) and lipid-coated (B). Measurements performed by A. Spiering and L. Galla[51]

4.4.2. DNA translocation through uncoated and lipid-coated membranes

Typical DNA translocation measurements through uncoated and lipid-coated silicon nitride membranes are illustrated in fig. 4.2. Whilst the measurements are remarkably similar at first glance, two differences stand out. On the one hand, the force is approximately doubled by the introduction of the lipid coating. This effect is explained on a more general scale in subsection 4.4.3. On the other hand, the force noise during the translocation more than doubles as well as long as the DNA is within the pore. This could be explained as follows: Even though the lipid coating forms a stationary, immoveable bilayer, the single lipid molecules can still move within the stationary bilayer. Respective diffusion coefficients in the range of $1\,\mathrm{nm^2\,\mu s^{-1}}$ to $2\,\mathrm{nm^2\,\mu s^{-1}}$ measured by FRAP have been reported[56]. Since the net movement within the bilayer has to be zero, individual Brownian movement might induce an increased noise in the measured force by weak interactions between the individual bilayer molecules and the DNA molecule. Also, the region of interest for video-based analysis should be adjusted for higher forces. If this is neglected, some edges fall outside of the region of interest, therefore limiting the number of available edges for circle fitting and thus increasing the noise as well.

4.4.3. Hydrodynamic slip and membrane surface charge

Analysing the numerous DNA translocation measurements performed in the last years in Bielefeld, mostly by A. Spiering and A. Sischka, indicates a strong dependency of the force acting on the DNA molecule at a constant applied voltage on the size of the

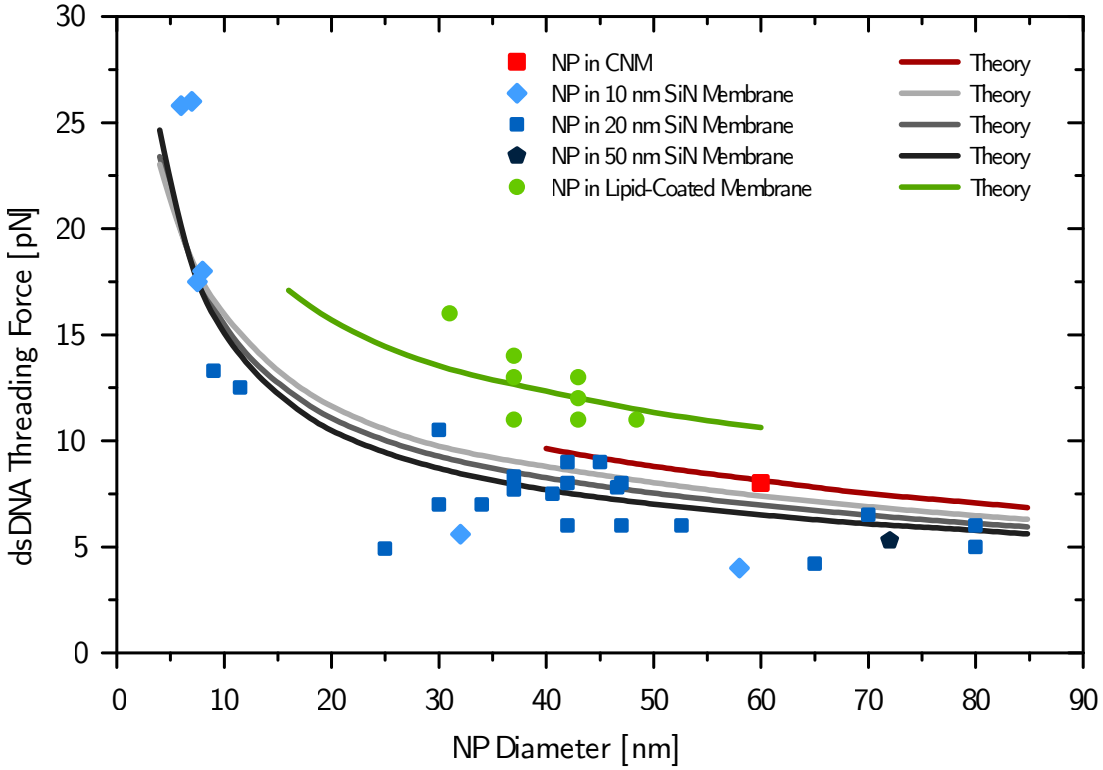

Fig. 4.3.: Dependence of the dsDNA threading force on nanopore size and membrane thickness and material

pores. With the introduction of lipid-coated membranes and nanopores and subsequent measurements on them primarily by L. Galla, a broad data base was available for A. Meyer and P. Reimann of the Theoretical Physics Department in Bielefeld to test their theories of the DNA translocation behaviour (as briefly outlined in section 3.2) against. One paper on this subject has already been published in 2014[51], another paper with a broader data base is scheduled to be published in a special issue and available as an advance article online[52].

The data and theoretical results are illustrated in fig. 4.3. A first result is that obviously the threading force increases for smaller pore sizes. Since the electrostatic force component is independent of the pore size, this can only be explained by the effects of the electroosmotic flow, which couples with the threaded DNA molecule.

Another immediately obvious result is the higher force for lipid-coated nanopores. Whilst the lipid coating does reduce the pore size by 9.6 nm[56], this effect alone does not explain the strong increase in force. In fact, the dominating effect was found to be the surface charge σ_m: Since there is a 1 nm to 2 nm thick water layer between

the membrane and the lipid bilayer[56,63,64], the surface charge of the silicon nitride membrane is shielded by the counterions in the water layer, resulting in an effectively electrically neutral surface of the bilayer, since it itself does not exhibit any surface charge. Thus, for lipid-coated membranes, $\sigma_m = 0\,\mathrm{mC\,m^{-2}}$.

In contrast, for bare silicon nitride membranes, the negative surface charge is not screened. The best fit results in $\sigma_m = -60\,\mathrm{mC\,m^{-2}}$.

Finally, it was found that only by introducing a slip-length boundary condition on the DNA (as mentioned, modelled as a homogeneously charged rod), reasonable force values are obtained. This is illustrated in fig. 4.4. Good quantitative agreements between theoretical simulations and experimental data is obtained for a slip length of $l_{\mathrm{slip}} = 0.5\,\mathrm{nm}$. This can be easily explained by the gross oversimplification in modelling the DNA as a simple rod, instead of taking into account e. g. the major and minor groove. Additionally, molecular dynamic simulations show that the water velocity is indeed not vanishing at the major groove of DNA[65,66], thus further supporting the assumed slip length.

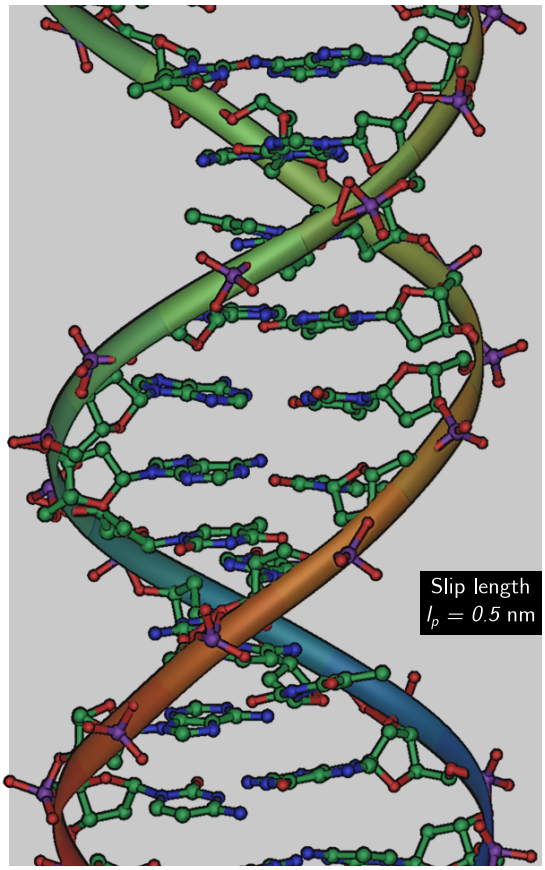

Fig. 4.4: Illustration of the slip length in the theoretical DNA model. The theoretical model simplifies the DNA (coloured) as a simple rod (grey) with diameter 2.2 nm. The slip length is shown in the major groove as the black bar. Ball-and-stick model of DNA by M. Ströck[67]

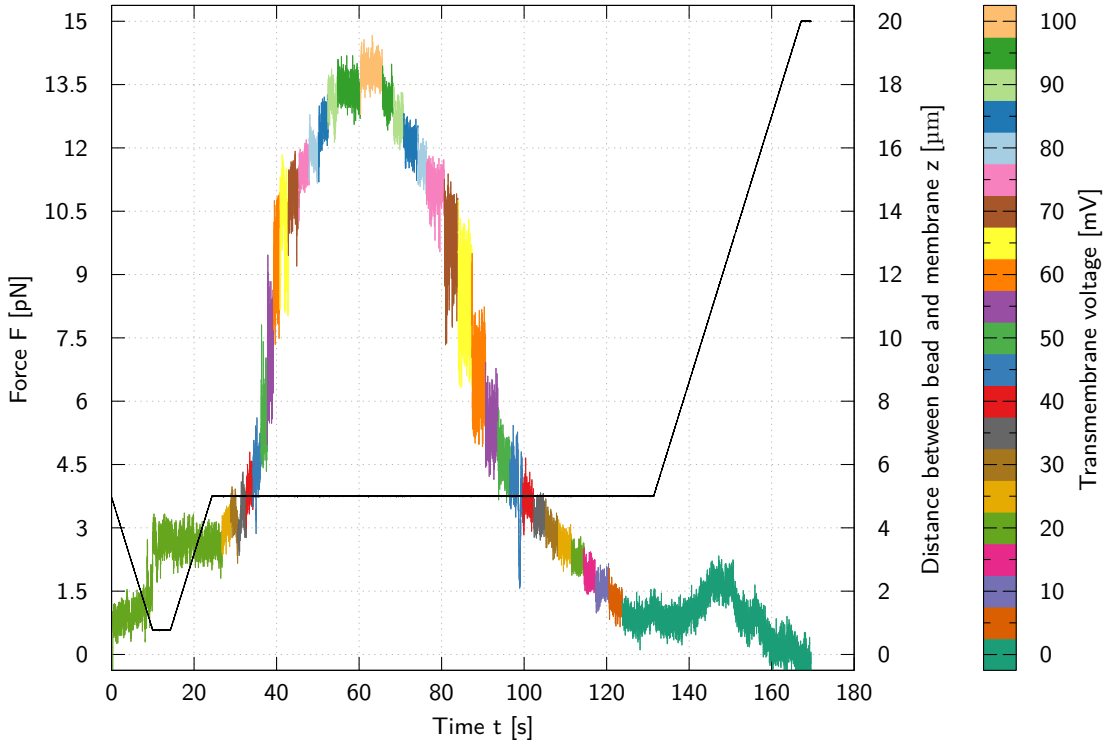

Fig. 4.5.: Force measurement of a DNA translocation through a 70 nm TEM-drilled nanopore in 20 nm thick Si_3N_4. Coloured data: force (left axis) with colour-coded transmembrane voltage (varied in 5 mV steps). Black line: distance between bead and membrane (right axis)

4.4.4. Non-linear force behaviour, force hysteresis, threading out at low voltage and non-linear zero force behaviour

In contrast to the measurements shown until now, the measurement of a DNA translocation through a 70 nm TEM-drilled nanopore in silicon nitride illustrated in fig. 4.5 is atypical and raises some interesting questions, which will be discussed in this section.

The measurement consists of three phases. The first phase, spanning the first 25 s of the measurement, is the threading of the DNA molecule into the nanopore at an applied transmembrane voltage of 20 mV. In the second phase, the voltage is slowly increased in steps of 5 mV to a maximum value of 100 mV and then slowly decreased in steps of 5 mV to 0 mV. In the third phase, the bead is slowly ($v = 0.42\,\mu m\,s^{-1}$) pulled away from the membrane, until a threading out event occurs at a distance of 13.12 µm at 150 s.

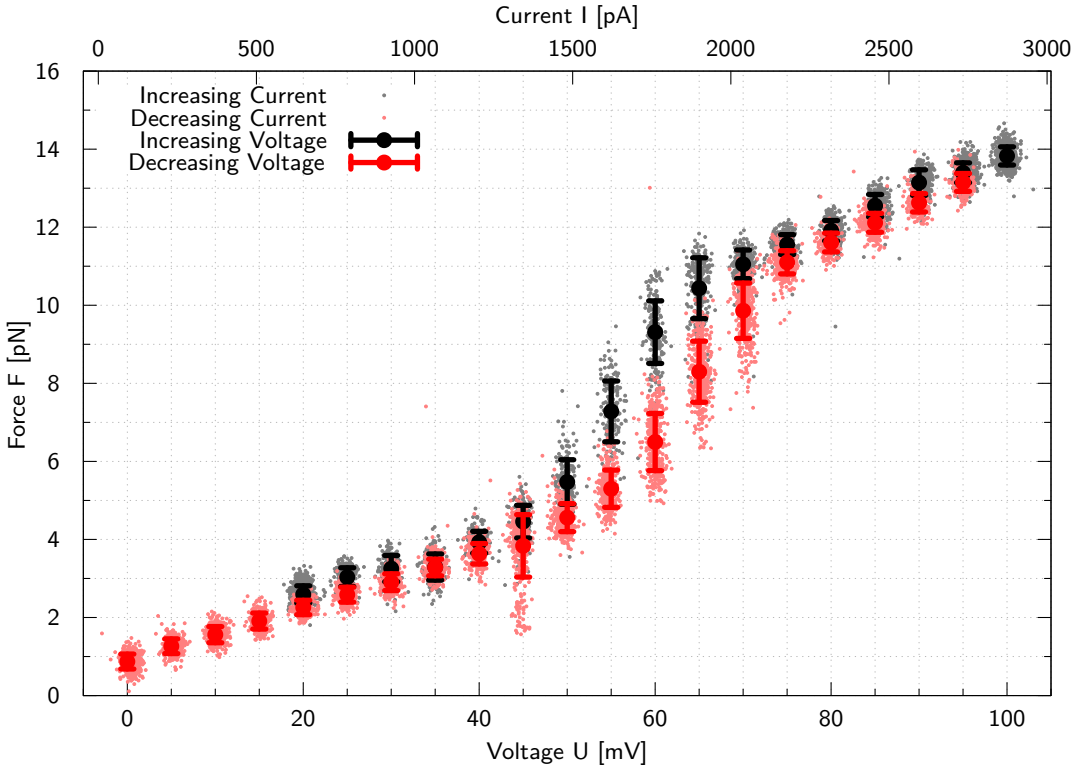

Fig. 4.6.: Non-linear force behaviour and force hysteresis upon increasing and then decreasing the transmembrane voltage. Data points with error bars are averaged values for one voltage (errors bars indicate standard deviation, bottom x-axis). Dots are single data points of force versus current (top x-axis)

4.4.4.1. Non-linear force behaviour

The overview graph in fig. 4.5 reveals a distinct non-linearity in the force behaviour in the range between 5 pN and 10 pN. This behaviour becomes obvious on plotting the force versus the applied voltage as in fig. 4.6. Here, we would expect a strongly linear dependency. Instead, it seems like the range between 5 pN and 10 pN should actually be the range between 5 pN and 7 pN. In fact, it is highly unlikely that the measured forces are truly the forces the bead was subjected to.

The explanation of the effect is simple. Video-based force detection is based on the assumption that the axial deflection of the bead and therefore the force can be described by equation 2.24:

$$\Delta z = \beta \cdot \left(\frac{r}{r_0(z)} - 1 \right)$$

For most beads, sample chambers and lighting conditions, this is true. However, some

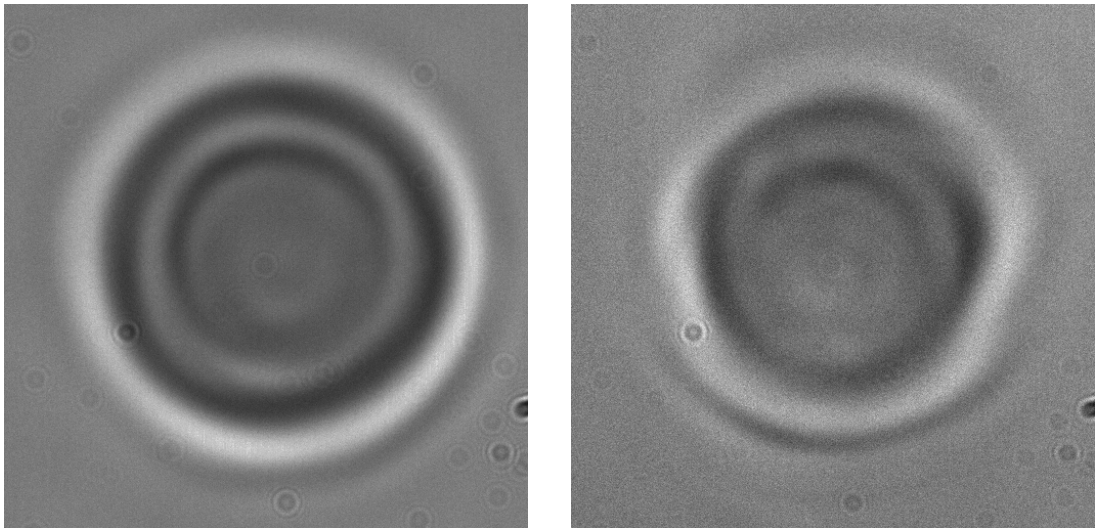

(a) Normal bead image (b) Bead next to air bubble

Fig. 4.7.: Normal and distorted image of a bead. The very small bead-like particles (next to the lower right corner and at 8 o'clock from the bead) are dust particles on the post-magnification lenses

beads exhibit a peculiar behaviour if defocused, due to small irregularities. Also, some sample chamber setups and lighting conditions are known to distort the image of the bead in certain situations. One easily explained example is an air bubble forming in the channel below the chip right next to it, as illustrated in fig. 4.7. The surface of the air bubble reflects light to the side of the bead, causing distortion.

Since this non-linear behaviour is atypical and not systematic, the simplest solution is to test for linear behaviour during force calibration, e. g. by moving the bead with velocities corresponding to 5 pN, 10 pN, and 15 pN according to Stokes' law. If a non-linear behaviour is observed, the bead should simply be discarded. If multiple subsequent beads exhibit such a non-linear behaviour, the system should be checked for any irregularities, like non-vertical lighting or air bubbles.

4.4.4.2. Force hysteresis

Another effect noticeable in fig. 4.6 is a force hysteresis, which has only been encountered once in our lab

One possible explanation is that the current might take some time to come into equilibrium. However, as indicated by the small dots, the current is the same for both increasing and decreasing voltages.

Other possible explanations are based on the time between the increasing voltage measurements and the subsequent decreasing voltage measurements. On the one hand, due to the intense lighting necessary in the experiments and subsequent localised heating, the membrane typically moves in the vicinity 0.5 µm downwards during the first 20 min of an experiment. Whilst the distance between bead and pore (which is of course lowered by this effect) should have no noticeable influence on the force, the movement of the membrane might also change the lighting conditions and therefore induce a shift in the zero-force bead size and therefore the measured force.

On the other hand, it seems plausible that the length of DNA between bead and membrane increased slightly, maybe due to the loosening of remaining DNA strand aggregations.

It would be interesting to see whether this effect can be reproduced and if so, whether it is a true hysteresis. Since the phenomenon was not discovered during the experiment but only afterwards, the voltage increase/decrease was not performed repeatedly. In further experiments, this should be done, with varying increase/decrease speeds. Since Brownian motion is already quite strong in the encountered force range, increasing the force for a better signal to noise ratio should be considered. This can be done by performing the measurements in smaller nanopores. Lipid-coating as a means to increase the force does not seem viable since the lipid-coating also increases the noise in the system and introduces another potentially voltage-dependent parameter.

4.4.4.3. Threading out at low voltage

After the measurements of the force-voltage dependency were performed, the bead was slowly pulled away from the membrane with a speed of $0.42\,\mu m\,s^{-1}$. During this time, the applied voltage was set to 0 mV. Both due to offsets in the voltage by the Axopatch controller and due to pressure difference induced flow, the current was non-zero at (102 ± 16) pA, which, with the resistance of $(35.95 \pm 0.05)\,M\Omega$, leads to a remaining effectively applied voltage of (3.7 ± 0.6) mV.

Despite this very small applied voltage, we still see a sudden force decrease by 0.5 pN at 13.12 µm distance between bead and membrane, which is a clear indicator that the DNA threaded out of the nanopore at this point.

4.4.4.4. Non-linear zero force behaviour

As is visible both in the overview plot in fig. 4.5 and especially in fig. 4.8, the force is not measured as constant as the distance between bead and membrane is varied, both

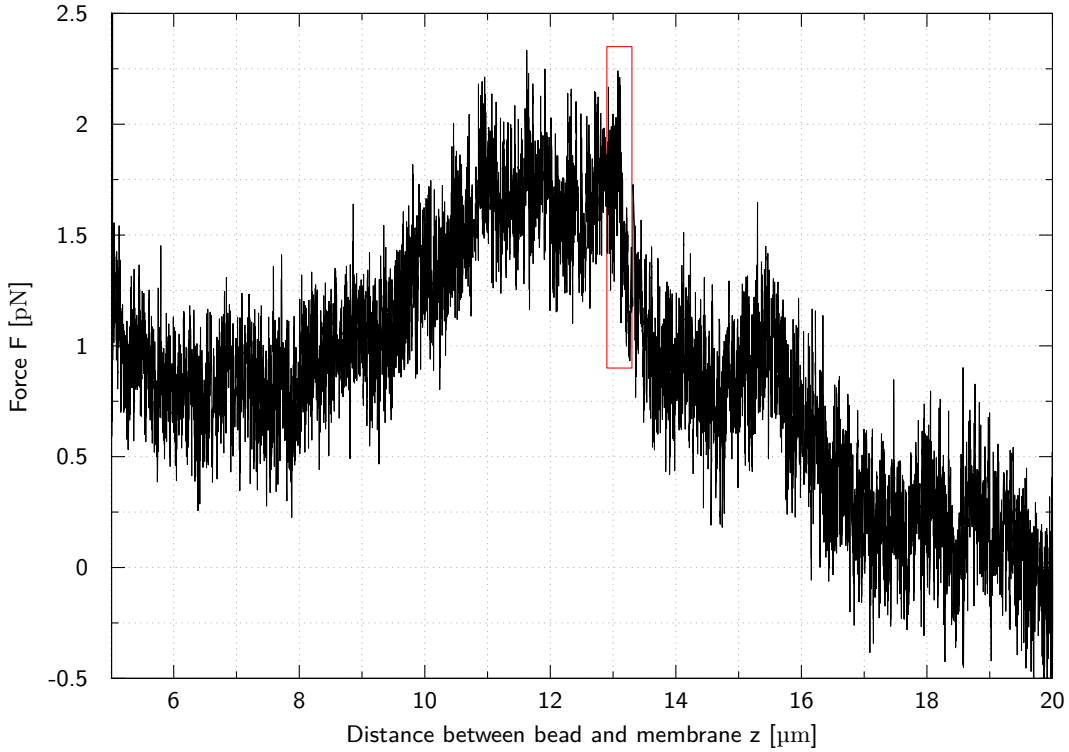

Fig. 4.8.: Threading out event at low transmembrane voltage occuring at 13.12 µm distance between bead and membrane

without a DNA in the pore (where a zero force is expected) and with DNA in the pore (where, with constant voltage, a constant force is expected).

Looking back at eq. 2.24, we see that the displacement and thus force is calculated by comparing the current apparent bead radius with the zero force bead radius. In most cases, the zero force bead radius is dependent on the distance between bead and membrane, due to different lighting conditions. To account for this effect, the zero force bead radius is linearly interpolated between two calibration measurements performed near and far away from the membrane.

It seems that this linear interpolation is not valid in all cases. In this measurement, the zero force radius varies non-linearly and aperiodically dependent on the current distance between bead and membrane. It seems that in the future, more reference measurements at different distances need to be performed, to allow for a finer interpolation. Since this is necessary anyway for molybdenum disulphide and other 2D material nanopores due to the chip setup, this change has already been integrated in the optical tweezers control software, as described in detail in section 7.3.3.

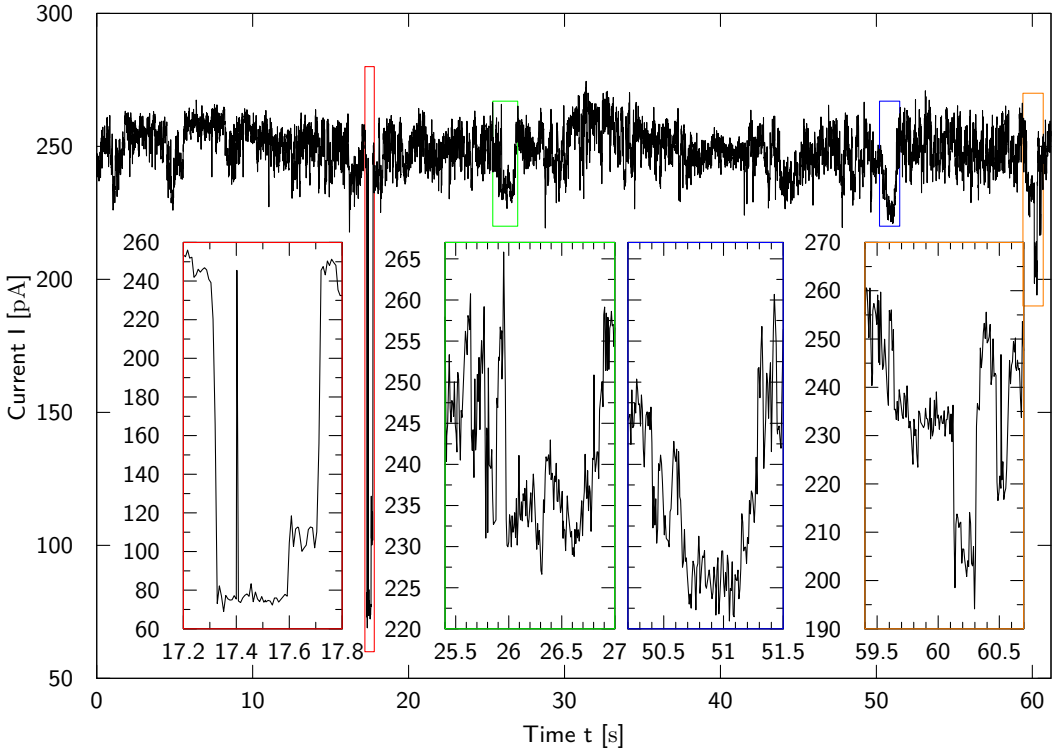

Fig. 4.9.: Coulter counter measurements on 2.5 nm nanopores, $U = 100$ mV, buffer of 1 M KCl and 10 mM Tris/HCl at pH 8.0. Insets show magnifications of the most prominent peaks, marked by colour.

4.4.5. Very small nanopores

As illustrated in fig. 4.3, the smallest pores measured in our lab were about 6 nm in diameter. M. Wanunu from Northeastern University kindly supplied 20 nm thick silicon nitride membranes with 2.5 nm to 3 nm pores. For such small nanopores, one would expect a very high force once the DNA is in the pore, but a difficult threading in process, since the diameter of the DNA double helix of 2.37 nm is only minimally smaller than the pore diameter.

In total, I tried to perform a controlled DNA translocation through five of these pores. Unfortunately, I did not succeed in performing controlled translocations. However, introducing DNA without attached beads into the sample chamber resulted in some short current dips as are typical for Coulter counter experiments. Especially when changing the buffer to 1 M KCl and 10 mM Tris/HCl at pH 8.0, translocation events occured somewhat frequently. An exemplary measurement is illustrated in fig. 4.9.

Unfortunately, due to the use of platinum wire contacts, the current signal is quite

noisy and the bandwidth is limited. Therefore, a quantitative analysis in the form of a current peak versus translocation time histogram is not feasible. Additionally, the contacts are very light sensitive. Since the Faraday cage in which the sample chamber is placed is not completely light-proof, as it has an opening in the top to allow access for the fibre optics light source, small 50 Hz oscillations and corresponding harmonics can be measured. Additionally, fourier analysis of the *open* noise at the analogue-digital-converter, i. e. without attached signal source, reveals prominent peaks at 50 Hz and harmonics, with one prominent peak at 1000 Hz. These peaks are independent from the sample rate and likely stem from insufficient shielding and/or grounding.

The four most distinct signal peaks of an exemplary measurement are highlighted in the insets in fig. 4.9. The first inset actually shows two drops in the current, first for 0.1 s by 170 pA, then the current momentarily returns to the normal value of 250 pA to then again decrease by 170 pA. In the second peak, however, the current stays at the lower value for 0.2 s to then increase by only 30 pA, where it remains for another 0.1 s. Only then does it return to the normal value. This result is in so far remarkable as it usually indicates that the DNA translocated in a folded form: The near-centre of the DNA translocates first, followed by both ends. If the fold occurs non-centred, the observed behaviour occurs: First, the current is greatly reduced. Then, when the first end is threaded out of the pore, the current increases suddenly to a higher level, where it remains for a short time. Only then does it return to the non-translocating value. The short first decrease could theoretically be another DNA fragment, but it seems unlikely that two DNA pieces translocate such a small nanopore immediately after another. Therefore, the most likely explanation is that the DNA first entered the nanopore in the bent state, then left it again for a moment and finally got pulled through the nanopore.

Since the pore size is only in the range of 2.5 nm to 3 nm and the persistence length $l_p = \kappa/(k_B T)$ of dsDNA is (53 ± 2) nm, this indicates that the DNA is subjected to high forces, as otherwise such a tight bending of the DNA would not be observed.

The second and third inset show longer and shallower events, with current decreases of only approx. 20 pA for 1 s. Especially in comparison of the third inset with the first, the gradual decrease of current is obvious. All together, this is an indication that we are in fact not witnessing a DNA translocation. Rather, the DNA approaches the vicinity of the nanopore opening in the membrane, thereby blocking the current slightly. After some time, the DNA diffuses away from the opening, releasing the current gradually.

In contrast, the fourth inset shows a shorter, more prominent and more abrupt peak

of at least 30 pA for 0.2 s. A prior decrease at 59.63 s might be inferred from the data, however the signal to noise ratio for this decrease is in the range of 1 and therefore not significant. Whilst the abrupt changes in current indicate at least a threading into the nanopore, both the missing depth and short duration of the peak suggest that a complete translocation did not take place. Instead, most likely one end of a DNA strand entered the opening of the nanopore and left it shortly afterwards.

5. Graphene

5.1. History and general properties

Graphene, since it's first isolation by A. Geim and K. Novoselov in 2004, has become a material of great interest mostly because of three highly interesting properties.

First, it is the strongest material known to mankind, with a tensile strength of 130 GPa and a Young's modulus of 1 TPa[68]. As the Nobel prize committee illustrated in the Nobel announcement, a $1\,\mathrm{m}^2$ sheet of graphene would be capable of holding an average cat ($m = 4\,\mathrm{kg}$) whilst being almost invisible and only weighting 0.77 mg, as much a a cat's whisker. Graphene nanotubes are also one of the few materials (another being boron nitride nanotubes) capable of being used as the cable for a space elevator.

Second, since every atom is available for reaction from both sides, graphene monolayers are highly reactive, especially the atoms near the edge and near defects, with chemical processes showing a high selectivity towards monolayers[69].

Third, graphene is a zero-gap semiconductor with six points in moment space where the Fermi surfaces for conduction and valence band form connecting double-cones (see fig. 5.1). The description of the excitation near those points is formally equal to the Dirac equation, giving rise to the name *Dirac points*. Thus, graphene is not only suitable as a material in integrated semiconductor circuits, but also as an experimental analogue for many questions in theoretical particle physics. Furthermore, an anomalous quantum Hall effect with added plateaus at strong magnetic fields and a strong Casimir effect are observed.

Of course, for our purposes, the most important property of graphene is simply its thickness of just a single atom, or 3.35 Å. In the context of DNA translocation through nanopores in graphene this is highly interesting, since the thickness of graphene equals the distance between subsequent bases in DNA. Therefore, only one (or two in the case of dsDNA) bases are inside the pore during a non-looped translocation event. For sequencing, if there are n bases within the nanopore at a given time, we have to distinguish 4^n different base combinations. With graphene, $n = 1$ and therefore only the four bases have to be distinguished.

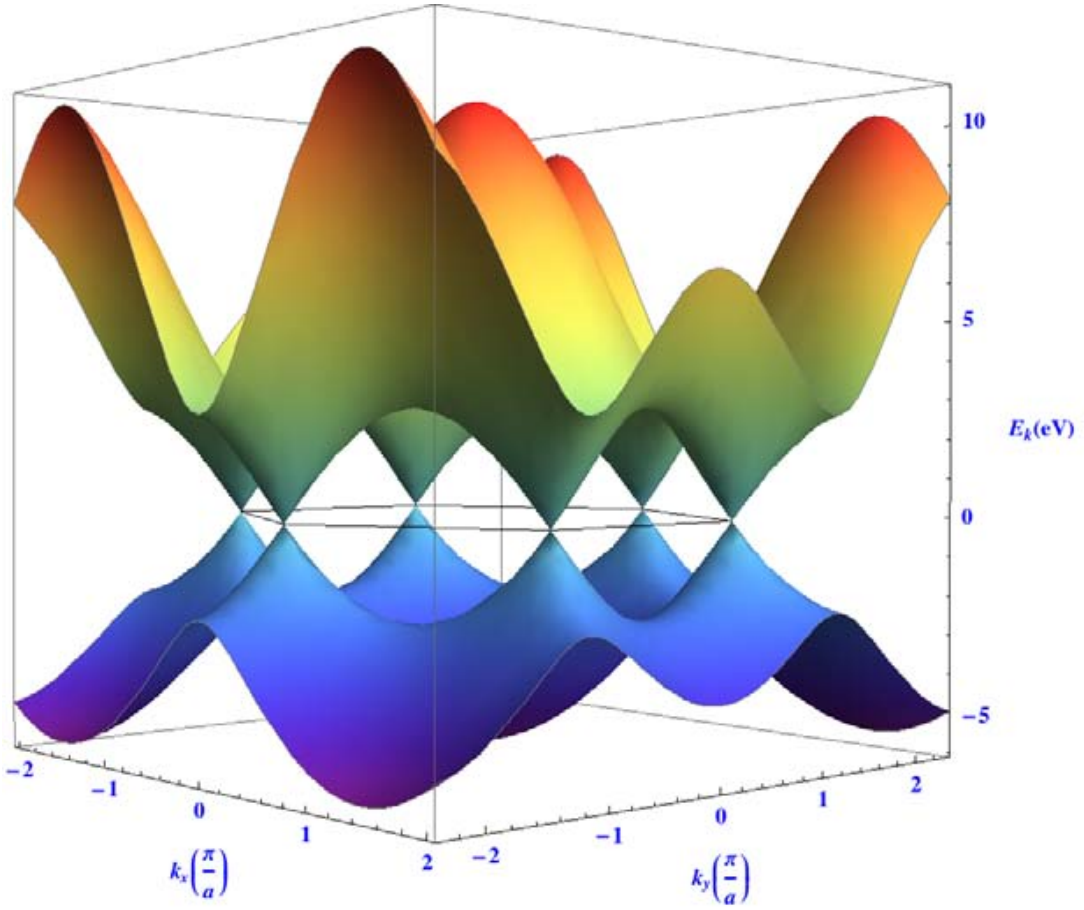

Fig. 5.1.: Energy for the excitations in graphene as a function of the wave numbers k_x and k_y. The black line represents the Fermi energy for an undoped graphene crystal. Image taken from [70]

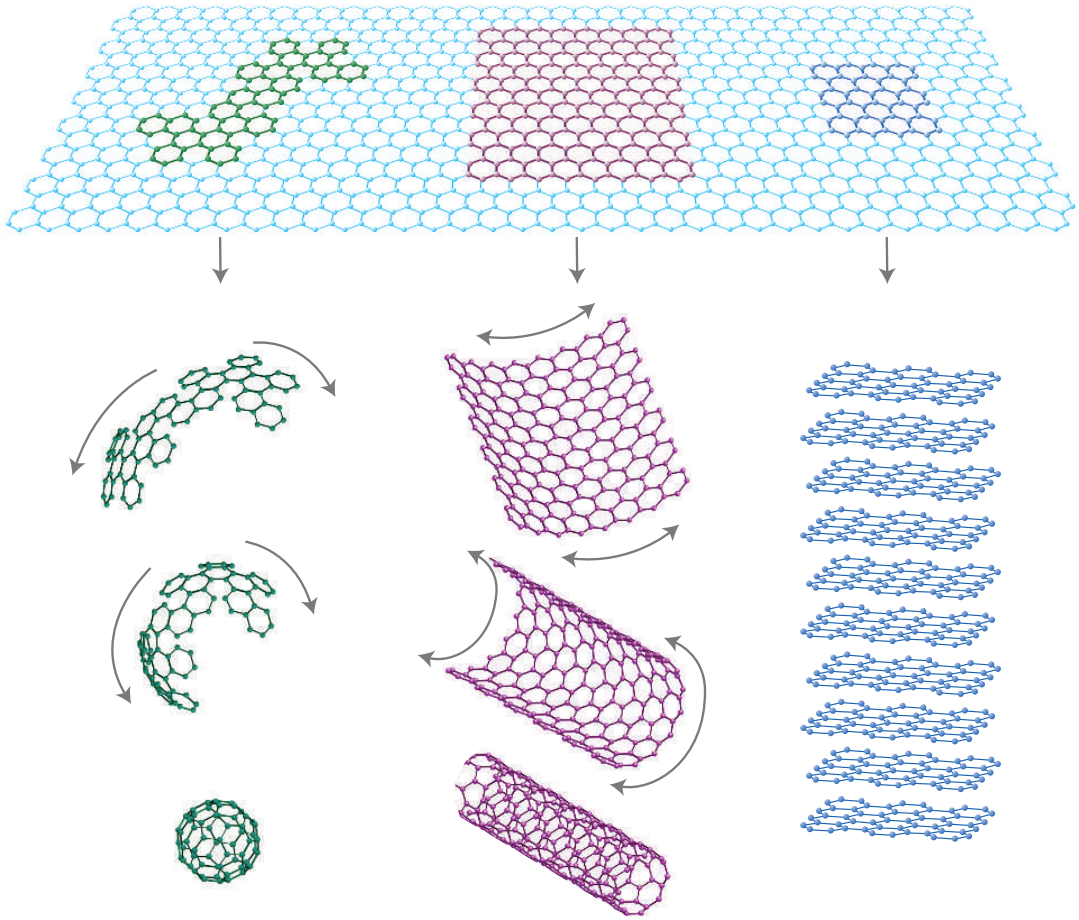

Fig. 5.2.: C60 fullerenes, carbon nanotubes, and graphite are all made up of graphene, from [71]

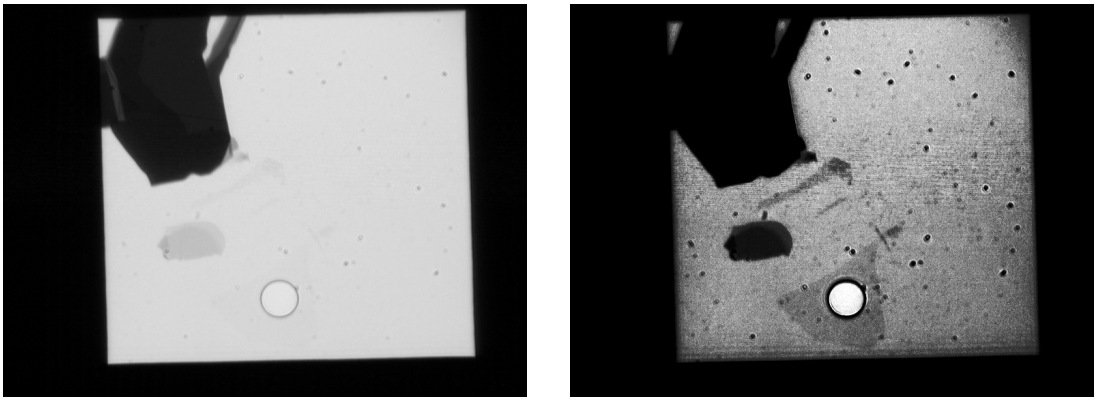

(a) Unmodified image (b) Increased contrast

Fig. 5.3.: Image of a chip with free-standing graphene monolayer membrane without nanopore. $R = (26.4 \pm 1.0)\,\mathrm{G\Omega}$

Graphene is a cystalline carbon allotrope with a hexagonal (honeycomb) pattern. As illustrated in fig. 5.2, C60 fullerenes, carbon nanotubes, and graphite can all be thought of as made up of single layers of graphene, either rolled into a sphere, rolled into a tube or stacked above each other. The graphene atoms, spaced 1.42 Å apart, are sp^2 hybridised, resulting in flat sheets. The three links to the neighbouring atoms consist of σ-bonds, the π-bond is directed perpendicular to the plane.

5.2. Preparation

Since the machanical exfoliation process described in section 3.4.2 was adopted from the original paper by Novoselov, Geim, et al.[58], no changes are necessary. Preparation therefore is performed as described in section 3.4 from a source of *highly ordered pyrolytic graphite* (HOPG). Since graphene is the thinnest material used in this work, finding graphene originally proved very challenging, since the light absorption of monolayers is quite low, as illustrated both in fig. 3.3 for a reflected-light microscope image of a bilayer and in fig. 5.3 for a transmission microscope image of a chip with a circular hole covered by a free-standing graphene monolayer membrane.

5.3. Results

Free-standing graphene monolayers both with and without nanopores have been produced. Resistance measurements on free-standing graphene membranes without pores

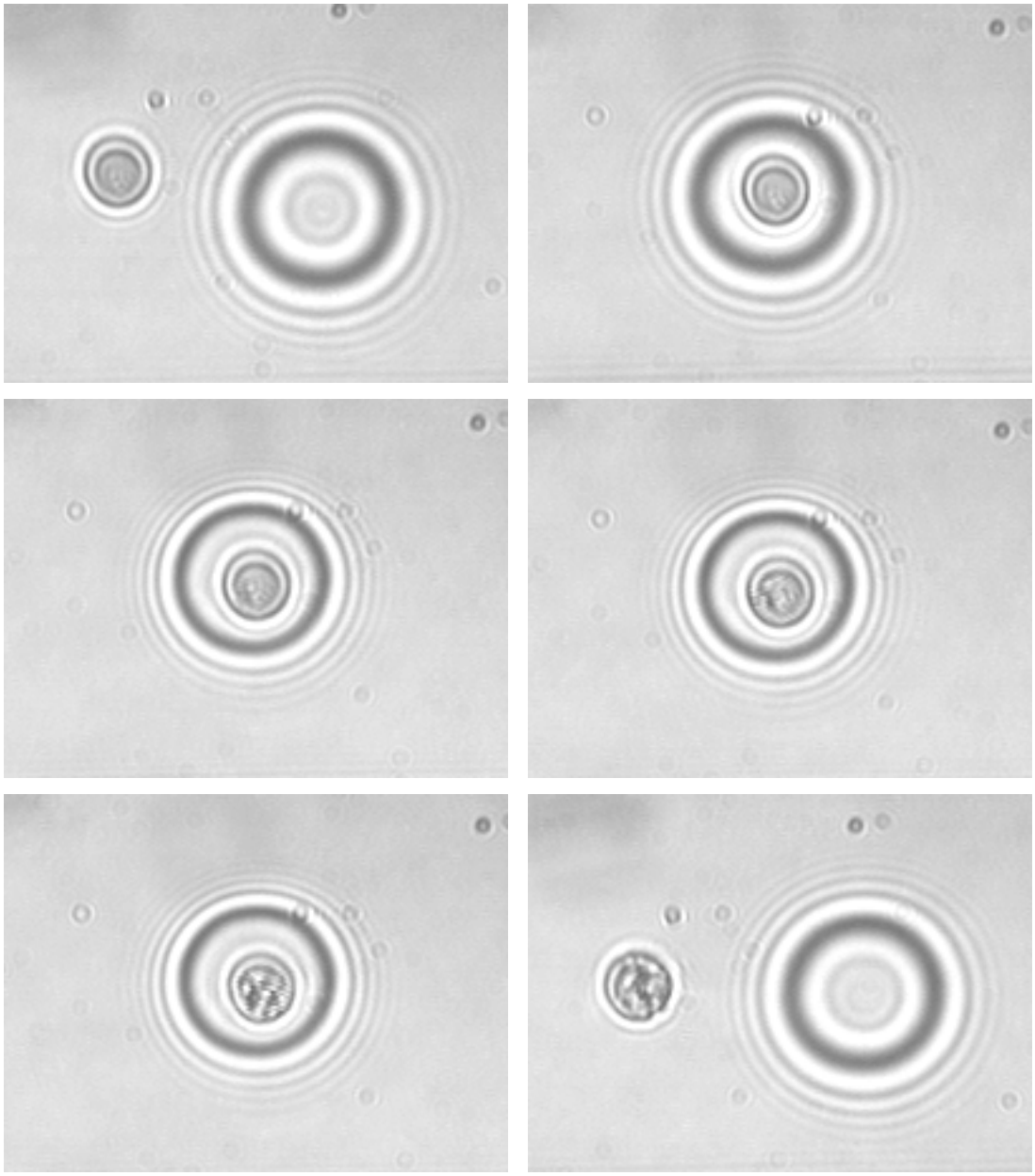

Fig. 5.4.: A trapped PS bead (laser power 750 mW) heats up in the vicinity of a free-standing graphene membrane

resulted in resistances above 1 GΩ, a sure indicator that the membrane is intact and there are no leaks.

Whilst Coulter counter measurements have been performed successfully both in our lab and in other groups[72–74], controlled translocation experiments pose significant challenges.

When approaching a membrane with an optically trapped polystyrene bead, an interesing localised heating effect occurs, as illustrated in fig. 5.4. Regarding the special electronic properties of graphene, it seems likely that this effect is caused by plasmon resonant coupling between the infrared trapping laser and the graphene surface in conjuction with the trapped polystyrene bead.

Since on the one hand, the glass transition temperature for polystyrene is 100 °C[75] and on the other hand, no bubbles from boiling water are observed, it seems likely that the heating either occurs localised within the bead or that initially the bead surface is heated and concurrently cooled by the surrounding water (which has a four times higher heat capacity[76] and a ten times higher thermal conductivity[76] than the bead). This would lead to an effectively localised heating within the bead as well.

Of course, a number of possible ways to quench this behaviour come to mind. As a first possibility, one might try to use a different trapping laser wavelength, which does not induce a resonant behaviour. Care must be taken to adjust the dichroic mirror and eye/camera protection in the setup accordingly. Alternatively, other bead materials could be utilised, e. g. silica glass. This might not quench the heating effect itself, but the melting behaviour of the beads. In such experiments, it should be verified whether the DNA is still attached to the bead after it was trapped near the surface, since surface heating at the bead will dissolve the binding to the DNA. Also, modifications of the graphene, e. g. doping, might reduce the heating effects.

However, it can be concluded that unmodified graphene is not a suitable membrane material with the current optical tweezers setup. Whilst there are some ideas to enable successful experiments with graphene, it is probably more reasonable to instead investigate other membrane materials.

6. Carbon nanomembranes (CNM)

6.1. General properties

Self-assembled monolayers (SAM) are organised layers of amphiphilic molecules, which orient spontaneously on surfaces[77,78]. SAM offer three possibilities to tune the properties according to ones specific requirements: The head group is responsible for (mostly covalently) binding to the surface and can be selected accordingly. The spacer determines the thickness of the SAM and can be selected from a wide range of available lenghts. Finally and most importantly, the terminal group is responsible for the properties of the resulting surface. Whilst this allows for countless kinds of SAM, some specific classes can be irradiated with electrons to form carbon nanomembranes. In Bielefeld, the working group *Physics of supra-molecular systems and surfaces* by Prof. Dr. Armin Gölzhäuser is studying them extensively.

6.2. Preparation

The preparation of the CNM was kindly performed by the Gölzhäuser group and is illustrated in fig. 6.1. 4'-nitro-1,1'-biphenyl-4-thiol binds covalently to the gold surface with its thiol group. The sample is then irradiated with 50 eV electrons to induce

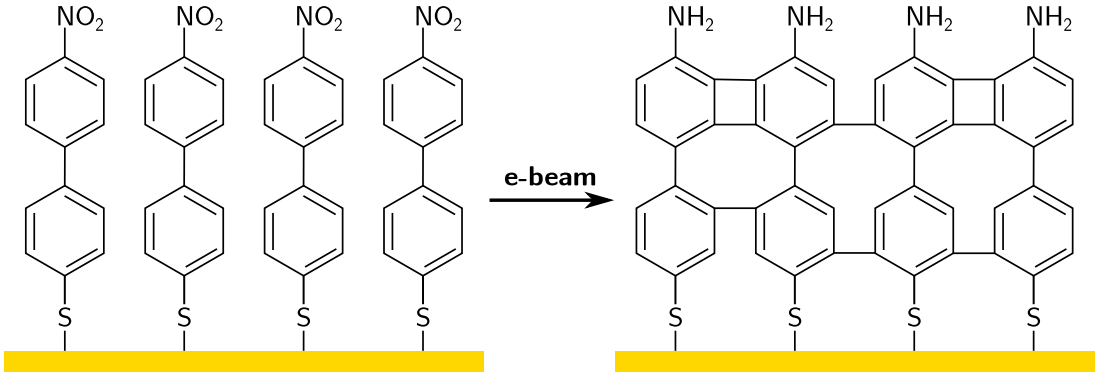

Fig. 6.1.: Schematic of the CNM preparation process on a gold surface[79]

cross-linking and converts the terminal nitro groups into amino groups[80]. It has been found that approximately 650 primary electrons per molecule are necessary to produce a completely cross-linked molecular network[79].

To transfer the CNM to the silicon chip, the following process has been developed in the Gölzhäuser group[81]: Two layers of Poly(methyl methacrylate) (PMMA) are spin coated onto the gold with the CNM. The first layer is created with PMMA with a chain length of 50 monomers. Spin coating with 4000 rpm for 90 s results in a layer approximately 90 nm thick. The CNM is dried after coating for five minutes at 90 °C. The second layer is formed with PMMA with a chain length of 950 monomers. The same parameters for the spin coating are used, resulting in a 310 nm thick layer. Again, the layer is dried for five minutes at 90 °C.

Afterwards, the coated CNM is cut into appropriately sized squares. Afterwards, the gold is completely removed in Lugol's solution (a solution of iodine and potassium iodine in water), and the PMMA with the CNM is again rinsed in water and placed onto the chip, similar to the usual process with cellulose polymer coated monolayers as described in section 3.4.4. Finally, the PMMA is removed with acetone and the chip carefully dried at the critical point for two hours.

6.3. Results

Unfortunately, almost all CNM samples did not achieve a gigaohm seal and were therefore not water-tight. Only one sample, which was thrice as thick as usual (3 nm thickness), resulted in a 4.1 GΩ seal. A 60 nm pore was drilled into the CNM and a DNA translocation has been successfully performed by A. Sischka, which is illustrated in fig. 6.2. Obviously, there are two DNA strands with different lengths in the pore. When the first strand is pulled out of the pore, the force suddenly decreases from 18 pN to 9 pN. The force then slowly decreases to 7 pN as the bead is pulled further away from the DNA. This is an artefact caused by the specific chip geometry, which was investigated extensively with molybdenum disulphide membranes. It is therefore discussed in detail in section 7.3.3, as is the interference-like pattern in the raw data. The force then suddenly drops to zero as the second DNA strand is pulled out of the pore[52].

The fact that two strands of DNA were in the pore simultaneously enables further discussion. First, it is noteworthy that the noise apparently increases when two strands of DNA are in the pore at the same time. This can be explained in part analogue to the increased noise during the DNA translocation through lipid-coated silicon-nitride

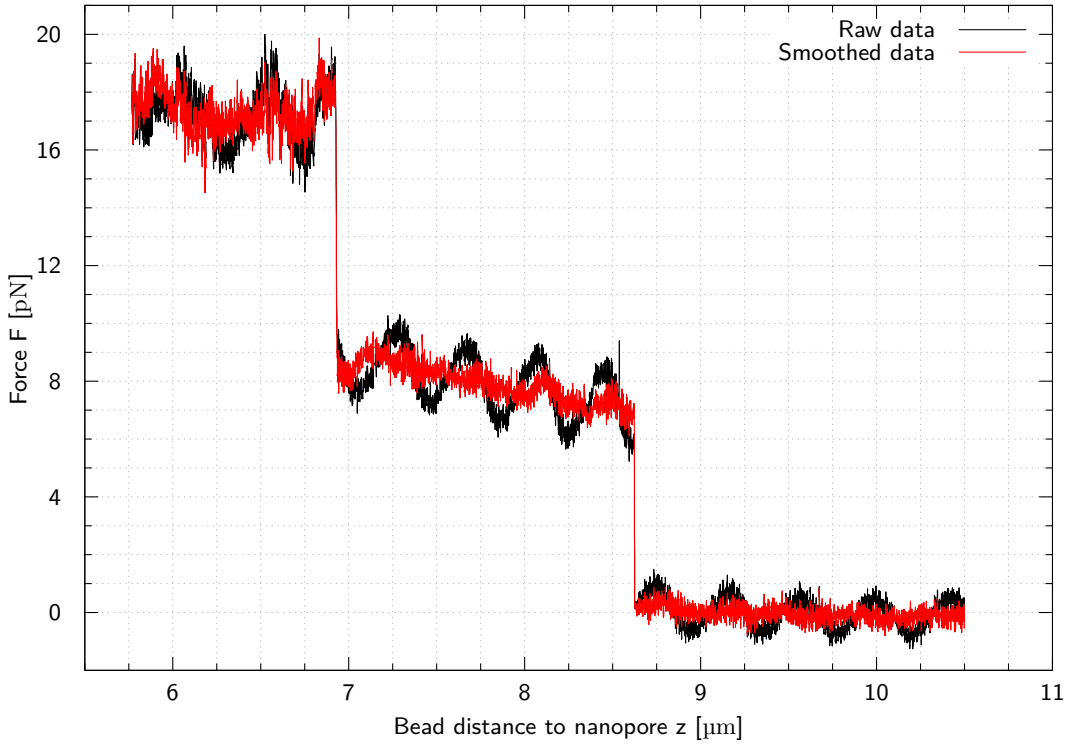

Fig. 6.2.: DNA translocation through a 3 nm thick CNM. Pore diameter: 60 nm. Transmembrane voltage: 50 mV

membranes, as described in section 4.4.2. On the one hand, two DNA strands in the pore slightly increase the noise due to interactions between the two strands. Even minute interactions lead to an increased noise, since the normal background noise is caused by Brownian motion of the trapped bead and thus has a completely different source. Therefore, additional noise caused by interactions between the two strands act additively. On the other hand, the high forces measured with two DNA strands within the pore lead to additional noise in the video-based analysis if precautions are not taken.

It is noteworthy that the force decrease caused by the threading out of the first strand is 9 pN, whilst the second decrease is only 7 pN. This behaviour is expected, since the two strands share a single nanopore of constant size, whilst having non-negligible thickness themselves.

7. Molybdenum disulphide

7.1. General properties

Molybdenum disulphide is a transition metal dichalcogenide with a trigonal prismatic structure, which is illustrated in fig. 7.1: Each molybdenum atom is connected to six sulphide atoms, three above and three below. Each sulphide atom in turn is connected to three molybdenum atoms, thus giving rise to a layered sandwich structure with the molybdenum lying between two layers of sulphide. Structurally, it can be thought of as graphene, with half the atoms being replaced by molybdenum atoms, and the other half being replaced by two sulphide atoms each, one above and one below the molybdenum layer. As with graphene, interactions between the sheets are only van der Waals', therefore allowing easy mechanical exfoliation.

7.2. Preparation

Preparation is very similar to graphene. In contrast to it, even single layers of molybdenum disulphide are easily visible under a reflected-light microscope, since the material reflects light. A sample chip with a molybdenum disulphide bilayer membrane, which has a small patch of a monolayer attached at the bottom, is illustrated in fig. 7.2.

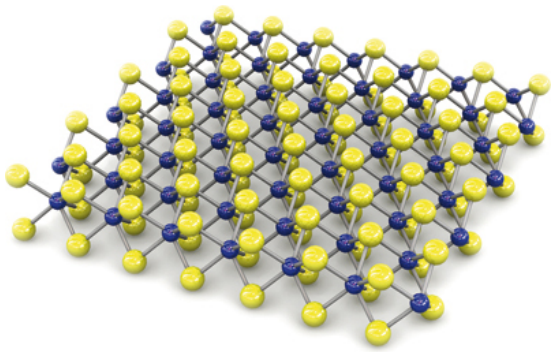

Fig. 7.1.: Structure of MoS_2. Blue: Molybdenum; Yellow: Sulphide.[82]

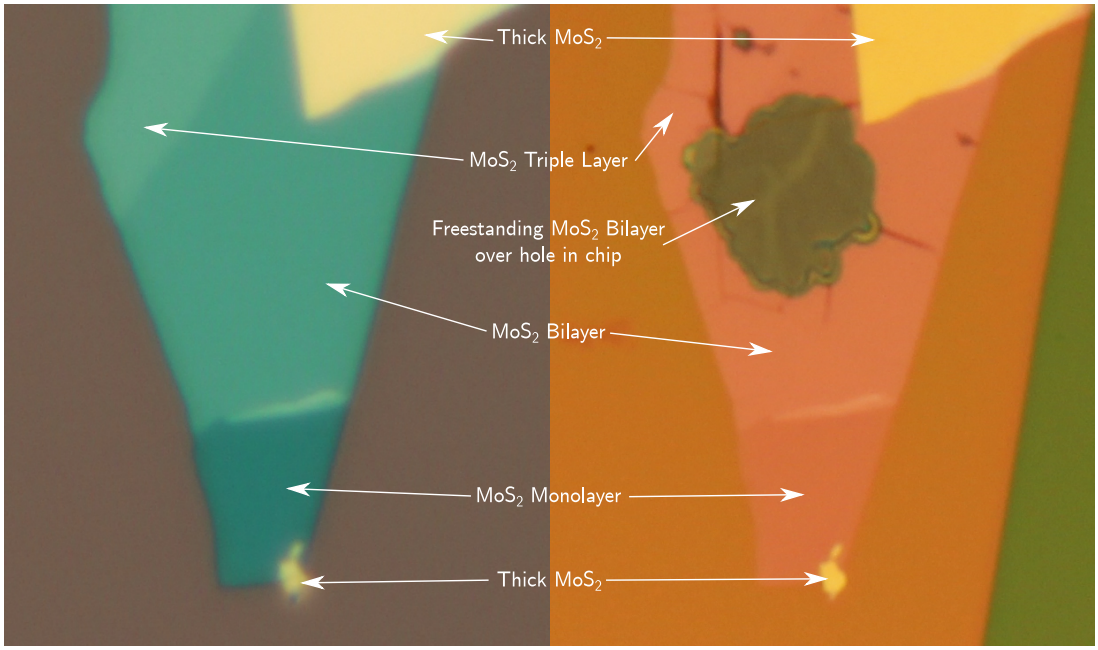

Fig. 7.2.: Wafer (left) and resulting chip (M3; right) with a free-standing MoS_2 bilayer membrane with a monolayer patch at the bottom

7.3. Results

In total, I was able to perform six transfers of molybdenum disulphide membranes to chips (M2 – M7). Together with one chip prepared by A. Sischka (M1), this gives seven chip with MoS_2 membranes. Inspection in an optical microscope revealed that of those seven chips, the hole was completely covered in five cases, namely chips M1, M3, M4, M5, and M7. Approx. 40 nm pores were drilled into these chips with the helium-ion microscope as described in section 3.4.5.

7.3.1. Mechanical stability

As a precaution, preparation of the sample chamber was performed under water to prevent membrane destruction by capillary forces. During one preparation, a water droplet accidentally formed at the edge of the chip window, thus exposing the membrane to capillary forces. Nevertheless, the membrane was still intact afterwards.

However, during the experiments, all five membranes were destroyed eventually. In three cases, the destruction was caused by the attempt to remove a bead that adhered to the membrane surface with optical tweezers. In the moment of bead capture, the bead was forced against the membrane, rupturing it. In at least on case, the flapping

remains of the membrane were visible in the microscope afterwards.

In one case, removal of a bead adhered to the membrane directly in front of the nanopore, blocking it, was attempted by introducing a 20 % solution of sodium hydroxide in the lower reservoir. Since the bead was not dissolved within two hours, the solution was left in the lower reservoir over night. The next day, the membrane and therefore the bead too were gone. The last sample chamber was destroyed by boiling buffer solution in the immediate vicinity of the membrane, as detailed below in section 7.3.5.

7.3.2. Electrical resistance

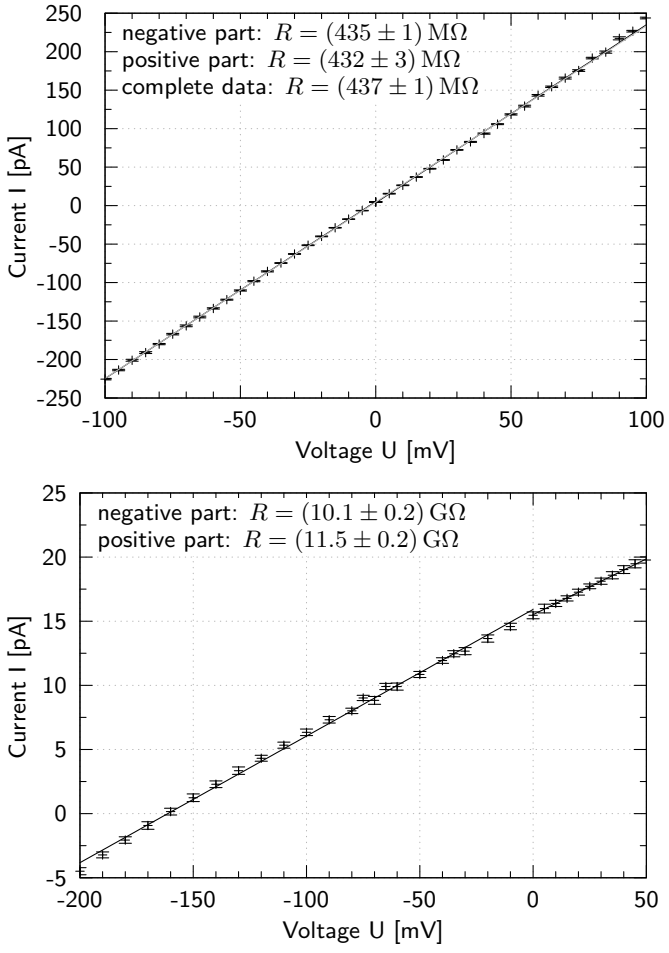

Fig. 7.3.: Resistance measurement of an approx. 40 nm MoS_2 nanopore without (top) and with (bottom) bead placed directly in front

Measurements of the electrical resistance of a pore (here, chip M1) shows a very ohmic behaviour, i. e. the current depends linearly on the voltage in the measured range from $-100\,\mathrm{mV}$ to $100\,\mathrm{mV}$, showing a resistance of $(437 \pm 1)\,\mathrm{M\Omega}$ for an approximately 40 nm pore.

Placing a polystyrene bead on the membrane directly in front of the nanopore increases the resistance over $10\,\mathrm{G\Omega}$, with a slightly diode behaviour: For negative voltages, the resistance is $(10.1 \pm 0.2)\,\mathrm{G\Omega}$, for positive voltages it is $(11.5 \pm 0.2)\,\mathrm{G\Omega}$. This result proves that the membrane is indeed completely intact. The slight diode behaviour can be easily explained by the mechanical setup: for negative voltages, the current presses against the bead away from the membrane, whereas for posi-

tive voltages, the current presses the bead against the membrane, sealing the pore even more tightly.

7.3.3. Non-linear zero force bead radius behaviour

As already mentioned in section 4.4.4.4, with video-based analysis the force is calculated by comparing the current apparent bead radius with a bead radius at zero force. Until now, the zero force bead radius was linearly interpolated between two measurements taken at different distances between bead and membrane to account for different lighting conditions and resulting changes in the apparent bead radius. However, the chip geometry used for all measurements on new membrane materials requires a different approach.

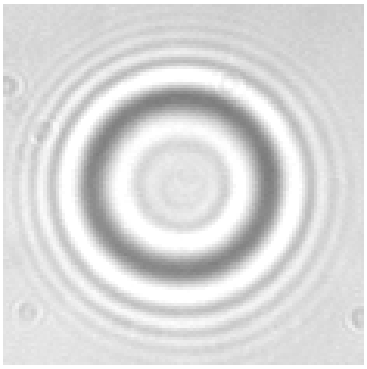

Fig. 7.4.: Interference pattern of defocused hole in chip

The fundamental problem is illustrated in fig. 7.4: The chip contains a hole about twice as large as the bead. Since the trapped bead and the membrane are never in the same focal plane, interference pattern of the hole edge emerge, smearing into the image of the trapped bead. This interferes with the bead size detection, leading to highly non-linear zero force bead radius behaviour, as exemplified for chip M1 in fig. 7.5.

There are two possible solutions to this problem. In the long term, a different chip layout featuring much smaller holes in the range of 0.5 µm could be used. Such holes are still visible in a microscope, as required for the membrane transfer process. However, they might be small enough that the visible interference pattern does not reach the edge of the bead and therefore it does not influence the bead size detection. As an added benefit, such chips would support much smaller membrane flakes. This would increase the yield for membrane preparation, since currently the limiting factor is the required size of the flakes.

As a short term solution, which also generally improves the data quality, I implemented a more advanced zero force radius interpolation algorithm. Instead of relying on the user to calibrate the zero force radius at two different distances between bead and membrane, the new system automatically moves the bead away from the membrane in adjustable steps (default: 0.1 µm, this is typically increased to 0.25 µm at around 5 µm distance between bead and membrane and then further increased to 0.5 µm at around 12 µm distance, in accordance with the typically increasing linearity for larger distances

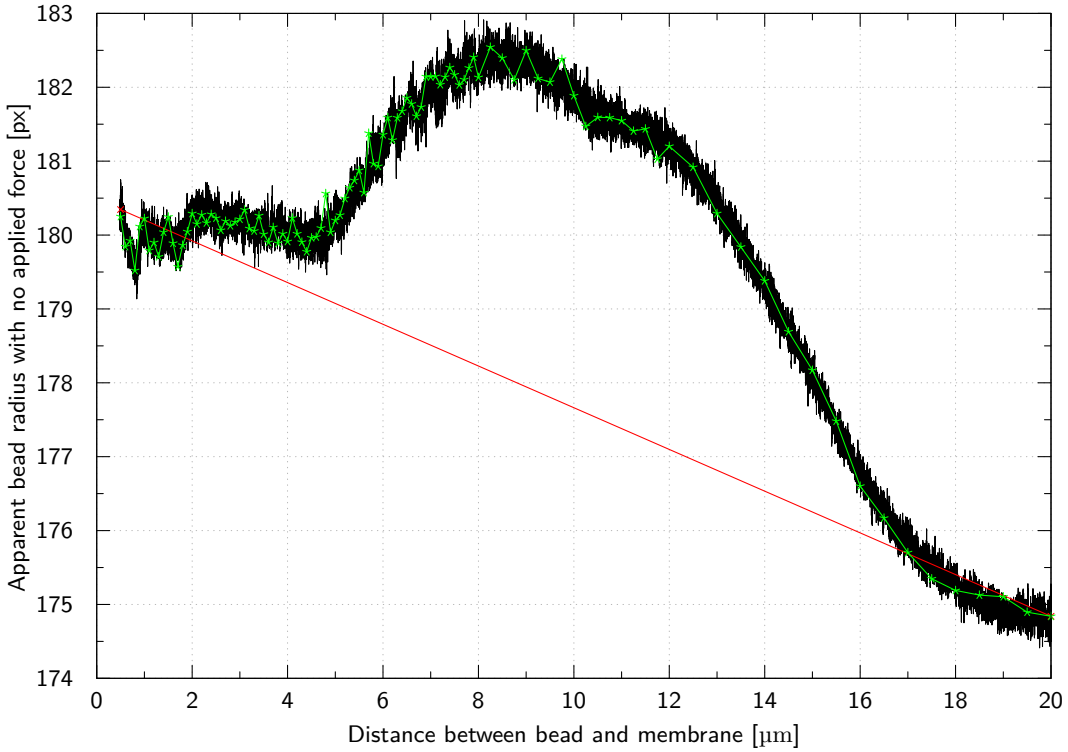

Fig. 7.5.: Dependency of the zero force bead size on the distance between bead and membrane (black). Previously, a linear dependency was expected (red), leading to large artefacts. With piecewise linear interpolation (green), the complex behaviour can be approximated very well

as per fig. 7.5). It averages the bead size for each step for an adjustable amount of time (default: 5 s). From this data, a piecewise linear interpolation is generated and used in subsequent measurements.

7.3.4. Controlled translocation

During the experiments with molybdenum disulphide nanopores, I successfully performed one translocation, which is shown in fig. 7.6. The measurement starts at a distance of 3.03 µm between bead and membrane. After 4.20 s the transmembrane voltage of 50 mV is applied. At 8.80 s, the force suddenly increases by 1.6 pN. From 17.53 s to 68.03 s, the bead is pulled away from the membrane with a speed of $0.30\,\mu m\,s^{-1}$, reaching a maximum distance of 18.00 µm. At 74.21 s, the transmembrane voltage is switched off. Shortly afterwards, at 75.43 s, the force suddenly decreases from 3.9 pN to 0.1 pN. Immediately after the measurement, the bead was moved back to the mem-

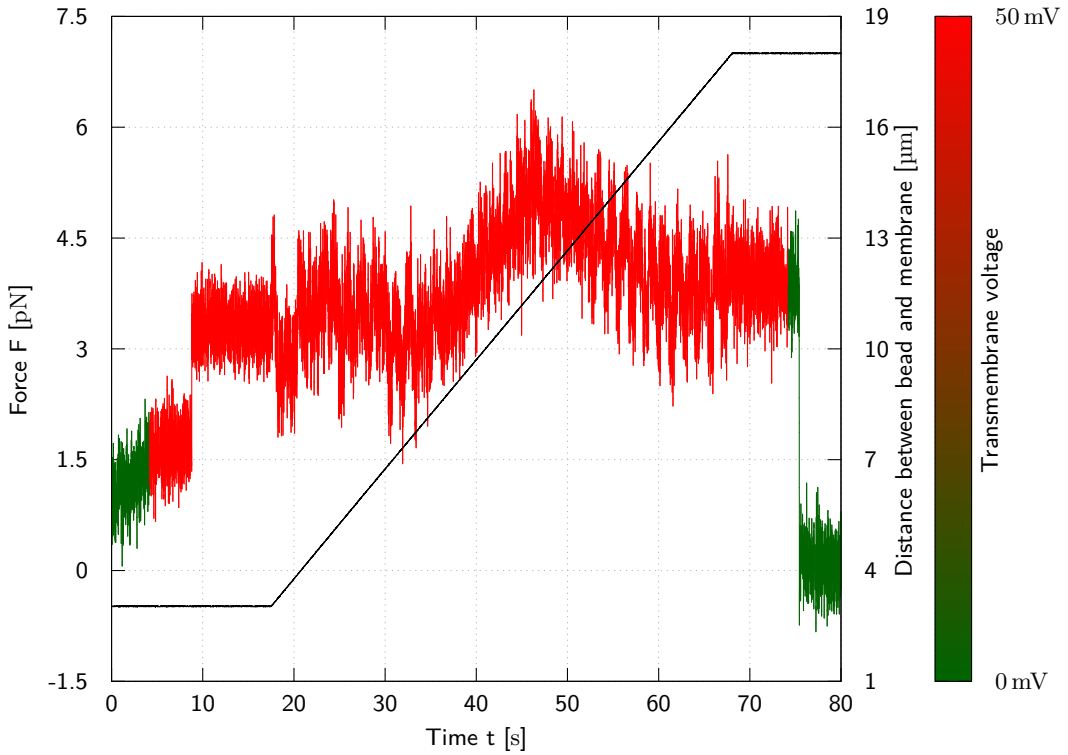

Fig. 7.6.: Translocation through a 40 nm MoS_2 nanopore. Force signal with colour-coded transmembrane voltage. Black line: Distance between bead and membrane.

brane. The data acquired during this approach was used to perform a high-detail zero force non-linearity correction of the data.

Although one might assume that the measurement shows a translocation of a normal DNA molecule, this seems unlikely. The used λ-DNA has a contour length of 16.5 µm. However, we still measure a force at a distance of 18 µm. This could be explained in principle by two DNA strands sticking to each other. However, in such a case we would expect a doubling of the force signal somewhere in the middle of the translocation, as both DNA strands are within the pore at the same time. This doubling would occur without transition as a sudden increase and then decrease in the force, just like the threading in and out at the beginning and end of the measurement. We do not measure such behaviour. There are three possible explanations: On the one hand, the translocating object could be something else than λ-DNA, which is longer than 18 µm. On the other hand, the distance could be off. This option will be discussed below. The most likely explanation however is that we measured one of the rare DNA

dimers. Those are a by-product of the DNA fabrication process and filtered out by the manufacturer. However, that filtering process is not perfect. Therefore, very rarely we measure DNA fragments that are longer then the contour length of a single strand. In the last eight years, this has been observed approximately three times.

Distance calibration, as mentioned before, is carried out by approaching the bead to the membrane until they touch. Since the MoS_2 membrane is quite fragile, this approach is performed not on the free-standing membrane but right next to it. If the free-standing membrane however is not stretched tightly across the hole but is instead sagging down, this introduces a systematic over-estimation of the distance between bead and membrane. Additionally, previous experiments on 20 nm thick silicon nitride windows have shown that the window tends to sag downwards with time under intense illumination, as required for video-based analysis. Here, we used 500 nm thick silicon nitride membranes. It can be assumed that the effect is much less pronounced in such thick membranes, but it can still be argued that the direction of any potential deformation should stay the same, i. e. downwards. Additionally, ionic pressure by the electroosmotic flow might induce a slight deformation in the direction of the flow, which is downwards here as well[51].

In this measurement, the bead was moved to a distance of 3.03 µm after initial distance calibration. Then, zero-force radius and force calibrations were carried out, which took approximately four minutes. Then, the presented measurement was performed. However, seven minutes after the start of this measurement, the bead was moved to a distance of just 0.50 µm, without touching the membrane. One can therefore safely assume that the maximum systematic distance offset is 0.50 µm. This would still require an object at least 17.5 µm long. Therefore, it seems highly unlikely that the translocation measured here was normal λ-DNA but a dimer.

Another interesting effect is that the force stays the same upon turning off the transmembrane voltage for about 1.22 s. This can easily be explained by the object adhering to the membrane surface near or in the pore. Due to random fluctuations, this unspecific binding loosens after some short time.

Also, the force behaviour in the beginning of the measurement is quite interesting. Instead of remaining zero, the force steadily increases, until the threading in event is observed. Then, it remains at the constant value of 3.3 pN (of course with Brownian noise). That value is also similar to the force directly before threading out of 3.9 pN. The difference between those two forces is likely caused by some minor non-linearity in the force calculation.

The increasing force at the beginning of the measurement could be explained by

pressure-driven or ionic flow from the lower to the upper reservoir through the nanopore, which also acts on the object attached to the bead and pulls it nearer to the nanopore, where the flow is stronger. Whilst it seems like the force increase slows once the transmembrane voltage is applied, this could also be attributed to asymptotic behaviour. Unfortunately, the low signal to noise ratio does not allow a more detailed analysis. This explanation is problematic in so far as the applied transmembrane voltage also induces an electroosmotic flow, which is directed from the top to the bottom reservoir[51]. If the increasing force were indeed induced by a flow, we would expect a sudden decrease in the force at switching on the transmembrane voltage, which is not the case. Another possible explanation is that the increase is simply a measurement artefact, caused e. g. by dirt particles near the trapped bead.

It is also noteworthy that regular interference oscillations every $(420 \pm 20)\,\mathrm{nm}$ can be observed. On the one hand, the used bead was on the larger end of the bead size distribution for the nominally 3.05 µm beads and thus reflects more light, according to fig. 2.9. On the other hand, molybdenum disulphide is very reflective. Combined, this creates the interference effect in the vicinity of a membrane as discussed in section 2.5.

7.3.5. Boiling effects

During experiments with chip M3, an interesting boiling effect was observed, which immediately ruptured the membrane. Unfortunately, the first boiling effect was not recorded. However, the effect was reproducible and could therefore be analysed in detail.

The general setup of this specific chip is illustrated in fig. 7.9. In the left image and in the following time series, the timestamp (relative to the boiling event) and the distance between bead and membrane are displayed in the top left corner of the image.

The chip consists of a free-standing MoS_2 bilayer, to which a dirt particle has adhered. Since a boiling has already occurred, the membrane is no longer intact and only some pieces, amongst them the part with the dirt particle, are remaining. Interestingly, the remaining parts of the bilayer are stable and not flapping around, which can be attributed to tension in the bilayer.

The actual boiling process is illustrated in fig. 7.7 and fig. 7.8. At a distance of 1 µm, the bead is slowly moved to the dirt particle. Once the bead is directly next to the particle, an air bubble is forming (5th frame, 0.00 s) and very rapidly expanding (6th frame at 0.08 s), slowly approaching the final size around 3 s.

The bead remains trapped through the entire process. Also, it is not melting or being deformed in any noticeable way. This is expected, since the heating is caused

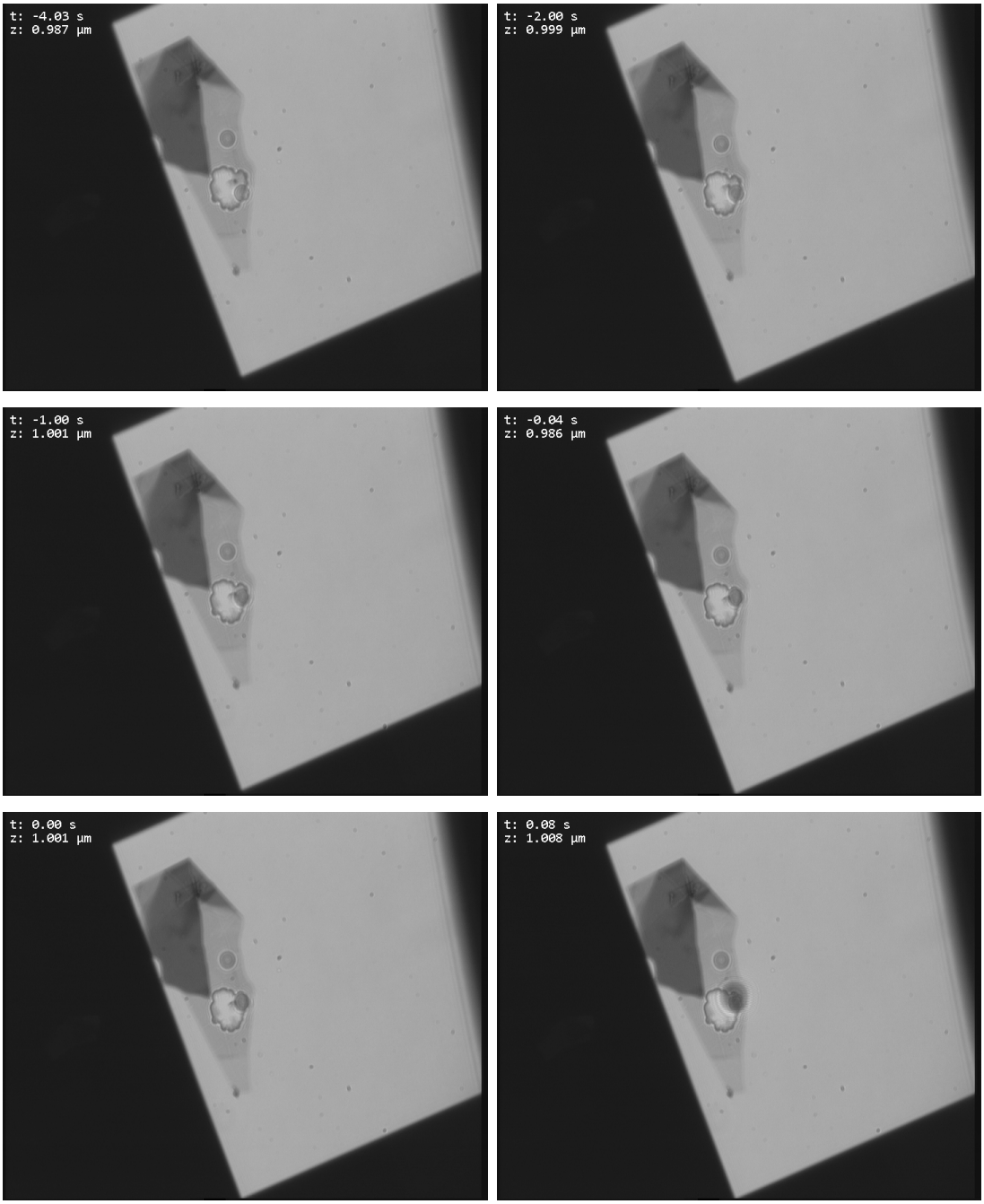

Fig. 7.7.: Still frames from the boiling process. t indicates time before/after the start of the boiling, z denotes the distance between trapped bead and membrane. Laser focus is approx. 1.5 µm further away.

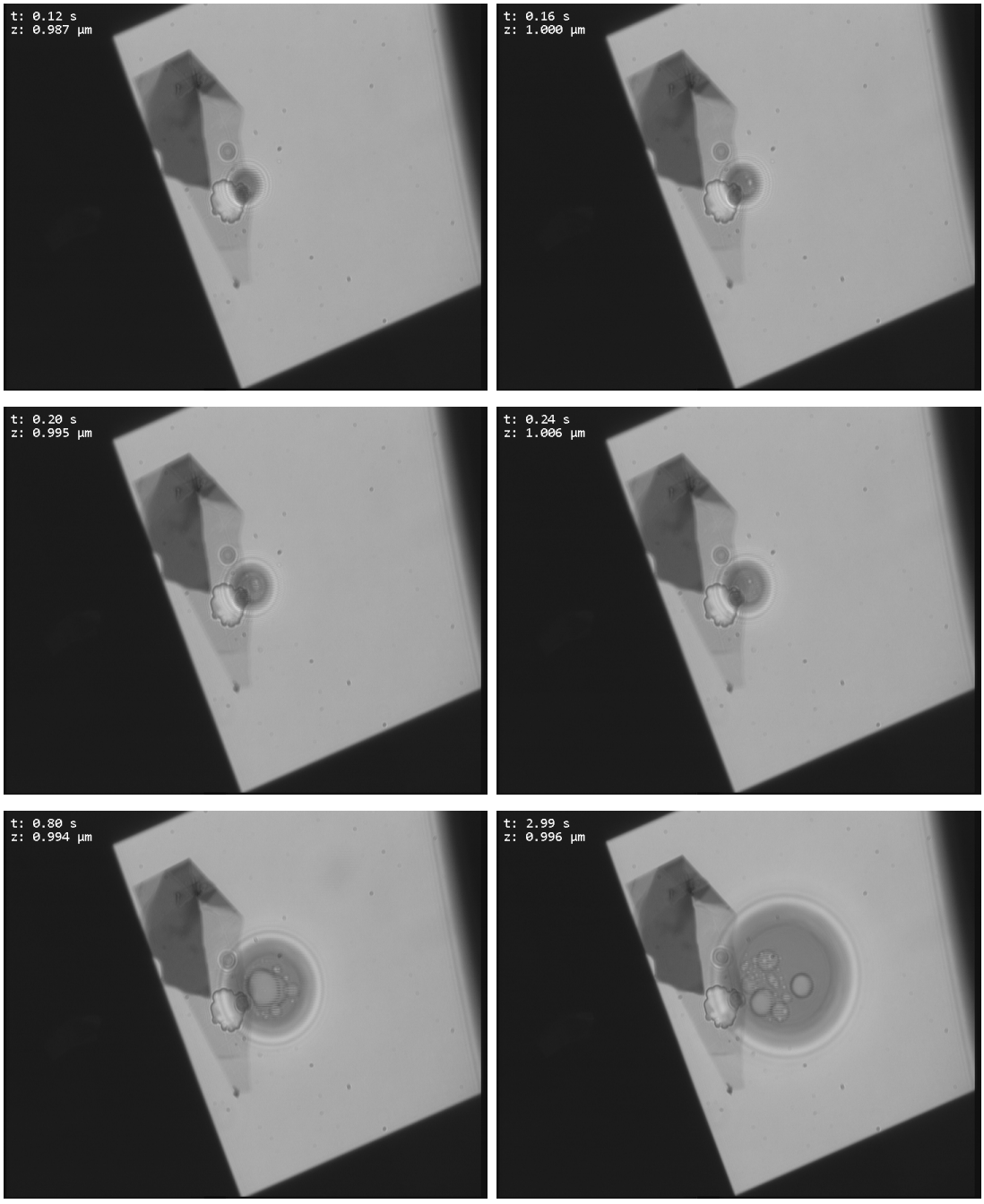

Fig. 7.8.: Cont.: Still frames from the boiling process. t indicates time before/after the start of the boiling, z denotes the distance between trapped bead and membrane. Laser focus is approx. 1.5 µm further away.

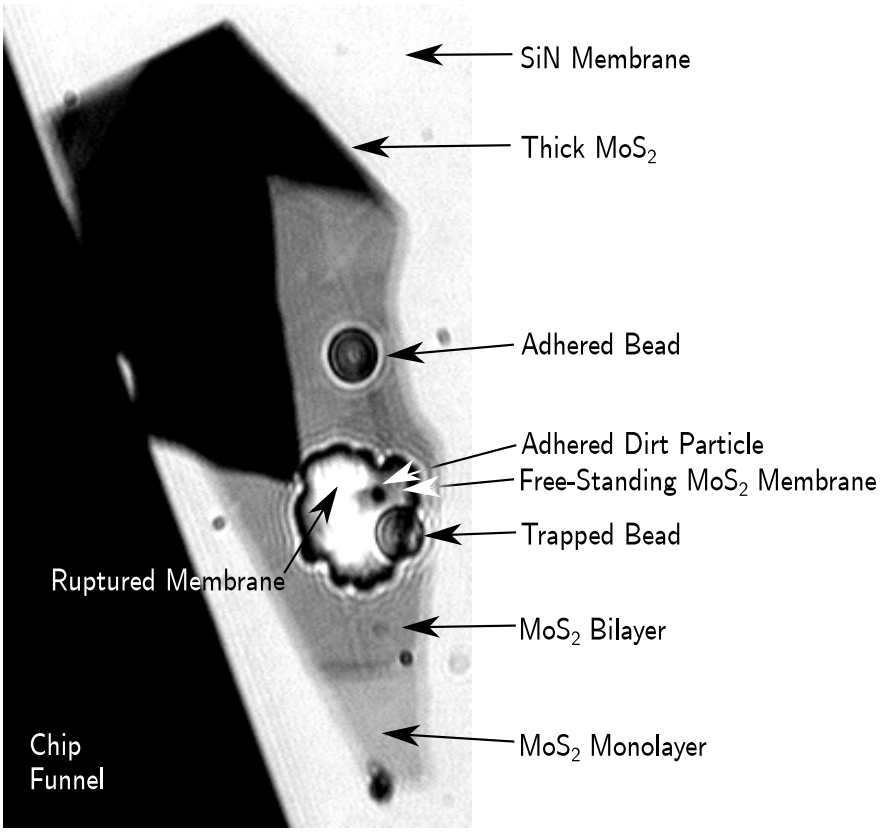

Fig. 7.9.: Contrast-enhanced overview of the setup for chip M3. Notice that the membrane was already ruptured by a previous short boiling

by illuminating a highly absorptive (dirt) particle with a focused infra-red laser beam. The heating is therefore not related to the trapped bead.

As a consequence, care must be taken to ensure that the membrane remains dirt-free at all times.

8. Molybdenum diselenide and tungsten diselenide

8.1. General properties

Just like molybdenum disulphide, molybdenum diselenide ($MoSe_2$) and tungsten diselenide (WSe_2) are transition metal dichalcogenides with a trigonal prismatic structure. For molybdenum diselenide, compared to molybdenum disulphide, the sulphide atoms are replaced by selenium atoms; the molybdenum atoms still form the center layer. For tungsten diselenide, the center layer is formed by tungsten, respectively. Since these two materials are in the same chemical class and form the same crystal structure, we expect similar properties regarding our application. This proves to be the case.

8.2. Preparation

As with molybdenum disulphide and graphene, molybdenum diselenide and tungsten diselenide are commercially available in bulk crystal form. However, for this thesis I used samples provided by Prof. Dr. Sebastian Fiechter from the *Helmholtz Zentrum*

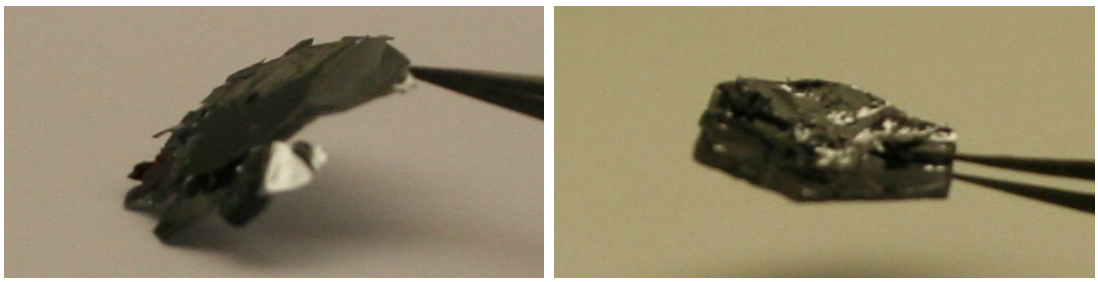

(a) $MoSe_2$ source (b) MoS_2 source

Fig. 8.1.: Comparison of the sources for $MoSe_2$ and MoS_2. The source for WSe_2 looks similar to the $MoSe_2$ source; the HOPG source for graphene looks similar to the MoS_2 source

Berlin für Materialien und Energie. These samples are very thin flakes, as illustrated in fig. 8.1. Since it is difficult to perform the initial exfoliation from the bulk material as usual, the preparation process is adjusted slightly. Instead of the initial exfoliation from the bulk crystal, a small flake (approx. $10\,\mathrm{mm}^2$) is placed with a pair of tweezers directly on the nitto tape. Then, as in the usual process, the nitto tape is folded eight times and the transfer is performed as usual.

8.3. Results

Preliminary preparations have been performed with both materials to analyse the general suitability for our experiments. Both resulting wafers show a larger number of small ($1\,\mu\mathrm{m}^2$) and thick (probably dozens of layers) material patches than usual. Thin layers could not be found in significant sizes. Also, the patches were not distributed quasi-uniformly but in localised clusters.

Therefore, the available samples of molybdenum diselenide and tungsten diselenide are unsuitable for our experiments, according to preliminary results. Of course, changed parameters for the distribution of the materials on the nitto tape could be investigated. However, the initial exfoliation from the bulk crystal seems to be of utmost importance for good results. Thus, it seems more reasonable to try to perform the initial exfoliation from the available material despite the difficulties posed by their flake-like consistency, or to simply buy corresponding crystals from commercial sources (typical prices are in the range of 150 EUR for a $5\,\mathrm{mm} \times 5\,\mathrm{mm} \times 1\,\mathrm{mm}$ crystal).

9. Other possible solid state membrane materials

The membrane materials presented herein are but a small excerpt of possible materials. This chapter shall provide a short overview of the range of possible materials.

9.1. Graphene analogue materials

Graphene analogue materials are two-dimensionally interlinked, atomically-thin materials. They stand in contrast to layered materials like molybdenum disulphide, in which a single layer is multiple atoms thick.

Boron nitride is an anorganic compound material strikingly similar to carbon. Like carbon, it exists in amorphous and in three crystalline forms: α-BN is the most stable crystalline allotrope, with a layered structure similar to graphite. Additionally, diamond analogue cubic boron nitride and and lonsdaleite analogue wurtzite boron nitride exist. α boron nitride is a semiconductor like graphene, but with a band gap in the UV range.

Phosphorene, which designates single layers of *black phosphorus*, is another material that can be considered graphene analogue, albeit with a slightly different structure. Due to the orthorhombric structure, it does not consist of a hexagonal flat sheet, but of interlinked rings in chair confirmation[83].

Additionally, graphene analogues of silicon and germanium, called *silicene*[84,85] and *germanene*[86] could be considered as possible membrane materials. However, until now, these materials have only been produced by epitaxy on a substrate and have not been observed as free-standing layers.

9.2. Halides and Chalcogenides

The halides and chalcogenides form a large group of materials with a large amount of layered materials. Some of them are poisonous of water soluble, which has to be taken into account.

Mercurous halides or mercury(I) halides Hg_2Cl_2, Hg_2Br_2 and Hg_2I_2 are interesting, since they form linear chains, which in turn form flat layered structures. Unfortunately, being mercury compounds, they are all highly toxic. Similarly, the *gallium dichalcogenides* Ga_2S_2, Ga_2Se_2[87] and Ga_2Te_2 as well as two *indium dichalcogenides* In_2S_2 and In_2Se_2[87] form linear layered chains similar to the mercurous halides and should therefore be suitable for exfoliation.

Of the group IV halides, tin(II) chloride (or *stannous chloride*) $SnCl_2$ is quite interesting, since it forms long, layered but not completely flat chains and could therefore be suitable for exfoliation.

Also, the class of transition metal chalcogenides is interesting, as is evident by the fact that three materials from that group have been investigated in this thesis. Besides the ordinary transition metals from groups 4 to 6, other chalcogenides could be of interest. Recently, monolayers of iron selenide FeSe have been successfully fabricated[88].

10. Conlusions

The goal of this thesis was to evaluate ultra thin solid state membrane materials for use as a standard nanopore material for DNA translocation experiments with optical tweezers. Additionally, the viability of translocation experiments with very small nanopores has been evaluated.

To enable an independent analysis of those two questions, small (2.5 nm to 3 nm) nanopores in our current standard material silicon nitride were evaluated. I succeeded in performing Coulter counter measurements of DNA translocation events. This shows that dsDNA is capable of passing through such small pores. However, a threading of DNA into the pore whilst attached to a bead could not be performed, showing the increased difficulty of performing *controlled* translocation through small nanopores.

For analysis of different solid state membrane materials, our current standard material silicon nitride has been investigated thoroughly. To showcase the ability of surface modifications, translocations through both bare and lipid-coated nanopores were measured. These measurements also lead to the development of a theoretical model[52], which introduced a slip length at the DNA.

Additionally, a threading out event at very low transmembrane voltage has been observed, showing that the system is indeed capable of detecting force changes as low as 0.5 pN.

As the first novel material, free-standing graphene membranes were investigated. To facilitate the preparation of those membranes, I developed an automated graphene flake detection software, which was subsequently used for other materials as well.

Experiments with unmodified free-standing graphene membranes show that DNA translocation with our current setup is still impossible, since the trapped polystyrene beads melt upon approaching the membrane. Whilst it might be possible to solve these challenges with surface modifications, changes in the setup or by using different bead materials, they prompted me to analyse other possible membrane materials.

Carbon nanomembranes, prepared by the Gölzhäuser group, were investigated as an alternative membrane material. Unfortunately, regular carbon nanomembranes were not water-tight. Only one sample resulted in a sealed membrane and allowed

for a subsequent successful DNA translocation measurement. As this membrane was apparently a result of some mistake in the preparation process, it is impossible to reproduce it.

Therefore, Molybdenum disulphide as a typical transition-metal dichalcogenide was investigated. With a single layer thickness of 1.0 nm it is only three times as thick as graphene. I successfully prepared molybdenum disulphide membranes with nanopores and was able to measure a controlled translocation through such a nanopore. Therefore, molybdenum disulphide proves to be a promising material for further analysis and translocation experiments.

As comparison, alternative materials such as tungsten diselenide and molybdenum diselenide were analysed briefly as well. In the form currently available to us, they are a bit more difficult to handle than molybdenum disulphide. Therefore, whilst further research with these materials is expedient, currently molybdenum disulphide is clearly more favourable.

The experiments presented herein not only serve to evaluate the corresponding membrane material or size. They also showed that video-based force detection for optical tweezers still has some room for improvement. The method performs very well for silicon nitride membranes, although even there some results prove to be more challenging then others. For other materials however special care must be taken to account for changed environmental conditions. Especially the holes in the supporting silicon chip over which the membrane is spanned can introduce unwanted artefacts. Nevertheless, video-based analysis was still capable of coping with all membrane materials and setups investigated in this thesis.

11. Outlook

11.1. Future research

The mechanics of the bead melting in front of free-standing graphene monolayers is of interest. Especially, it could be analysed whether free DNA translocation through a graphene nanopore measured with the Coulter counter method is reduced if the laser focus is brought to the vicinity of the nanopore, both with and without trapped bead. If the rate of translocation events decreases, this would indicate a localised thermal heating near the focus, which could be analysed further by introducing temperature dependent particles, e. g. vesicles that rupture at a certain temperature. If the translocation rate does not decrease, one might try controlled translocation experiments with other bead materials, like glass.

Additionally, one might try different methods to change the surface of the graphene, e. g. plasma oxidation. Both approaches are being carried out by S. Kißmer for her bachelor thesis. Additionally, changing the trapping laser wavelength might help alleviate the problems. Of course, a theoretical treatment of the effects would be interesting as well.

As an alternative to graphene not investigated in this thesis, boron nitride membranes should be evaluated as potential membrane materials. Alternatively, phosphorene could be utilised. In contrast to the investigated transition metal dichalcogenides, these materials are even thinner and could therefore enable DNA sequencing.

Regarding other novel membrane materials, many experiments present themselves. Those experiments should be performed with a changed chip layout featuring a much smaller hole, in the range of 500 nm. This would drastically reduce the challenges for video-based analysis and also increase the yield in membrane preparation.

Especially for molybdenum disulphide, future experiments should be performed. In those experiments, it should be of utmost importance to verify the fact that DNA is within the pore by varying the transmembrane voltage. Since the stability challenges are understood, it should be easier to avoid rupturing the membrane during the experiments.

As for the novel diselenide materials, future studies should show whether they are viable alternative membrane materials. Regarding ease of preparation, membrane stability and impermeability, a comparative analysis with molybdenum disulphide should be performed to find the best material for thin membranes.

Regarding silicon nitride membranes, the very small nanopores by M. Wanunu warrant more experiments. Also, the force hysteresis effect encountered in section 4.4.4 should be investigated further.

Finally, theoretical simulations show an interesting non-linear voltage-force dependency for small transmembrane voltages ($U \lesssim 20\,\mathrm{mV}$) especially for molecules with a low persistance length ($l_p \lesssim 2\,\mathrm{nm}$) like ssDNA, as discussed personally with A. Meyer. Of course, it would be very interesting to verify these findings in experiment.

11.2. Changes to the experimental setup and software

Recently, funding for a new camera for video-based force analysis has been granted. The new camera will allow force measurements with the current accuracy with 600 Hz sample rate instead of the current 123 Hz sample rate. With reduced accuracy by reducing the region of interest from a square covering the whole bead to a rectangular ROI covering a strip the width of the bead and the height of 3 % of the bead through the centre of the bead, a sample rate of 12 kHz is available. Of course, any setting between these extremes is possible, e. g. 2 kHz sample rate with slightly reduced accuracy.

For this improved setup, software changes are necessary, since the computer is unable to calculate the forces with full time resolution in real-time. Therefore, the raw video data will be streamed to a fast disk (SSD) and only frames corresponding to e. g. 20 Hz sample rate will be analysed in real-time to provide a feedback to the experimenter.

Since a complete software rewrite from scratch is most viable for such extensive changes, further improvements can be easily implemented in software. As seen in the experimental part, some problems arose due to some relations (e. g. force versus voltage) not being directly accessible in the software.

Therefore, the new software will allow for direct measurement and display of U-I, U-F, I-F and z-F relations. Also, a simple scripting interface will be added, allowing for arbitrary specifications, e. g. increase the piezo speed such that a drag force increasing in 1 pN steps results and then perform five piezo movements for drag force calibration as described in section 2.6.1.

These changes of course only serve to improve the experimental yield for future research.

A. Automated flake detection software

A crucial step in the preparation of 2D membranes by mechanical exfoliation is the detection of sufficiently large monolayers (or double, triple, ... layers) on the silicon wafer. As mentioned in sec. 3.4.2, manual detection is time consuming and tiring. Therefore, I developed an automated flake detection program, suitable for detecting flakes of defined minimum size of quasi arbitrary materials on silicon wafers.

Preliminary experiments were performed with a reflecting microsope (Olympus BX51, Olympus, Japan) and a DSLR (EOS 350D, Canon, Japan). The wafer was laid onto a manual stage and moved with (as far as possible) constant speed whilst images were taken with the DSLR. Since the number of images taken with a DSLR is limited due to shutter wear, usually in the range of 100 000, and a typical wafer takes between 1000 and 10 000 images to completely image, depending on the chosen magnification, this of course was no viable process. Therefore, a new DSLR (EOS 600D, Canon, Japan) offering live view capabilities was purchased. Live view allows the continuous acquisition of images whilst the shutter is open the whole time.

Since one of the goals was to image the complete chip at high resolution, image stitching techniques needed to be employed. Since I only image a plane, three-dimensional corrections are negligible, unlike in classical image stitching situations, where panoramas are created. Therefore, the task is simply to find the overlap between two subsequent images. In other words, the second image is moved in relation to the first image, and that movement vector has to be determined. This is a typical application for cross-correlation.

For two image functions $I(x, y)$ and $J(x, y)$ describing some aspect of a discrete image, e. g. the grey value or a single colour channel, the cross-correlation

$$(I \star J)(x, y) = \sum_{x',y'} I(x', y')J(x' + x, y' + y) \tag{A.1}$$

is at its global maximum at (x, y) if J is moved in relation to I by the vector (x, y).

Cross-correlation as well as any other image stitching technique (except simple stitching with known movement between the images) relies on distinct features (distinct in

the sense that they are extreme values of the imaging function). Thus, they work best for a large number of objects on non-uniform background. However, flakes on a silicon wafer are the extreme opposite: only a few distinct features (if at all) on a completely uniform background. It comes to no surprise that it is therefore virtually impossible to create a single image of the complete chip by stitching a large number of smaller images together with unknown movement between the images. A controlled movement between images is called for.

Fortunately, an unused xy-stage originally belonging to a PALM SPS system (Zeiss, Germany) was available. This stage is used to move the imaging area exactly one image length (or height) after each image is taken. Thus, a simple stitching without overlap can be employed.

A.1. Stage control protocol

The stage consists of two stepper motors, controlled by a proprietary controller unit (isepos, Germany). This unit used to be directed by a proprietary imaging software. Fortunately, documentation of the communication protocol between software and controller was available. This allowed me to reverse engineer my own controller library in LabView, enabling the integration into the flake detection software.

The following documentation is specific to firmware revision 154 and SPS revision 122.

Communications between PC and controller is performed using the RS-232 (serial) protocol. In default configuration, the controller is set to 38 400 bd, 1 start bit, 8 data bits, 1 stop bit, even parity.

Every message (both from PC to controller and vice versa) consists of the form `STX LFD DATA DLE ETX CS`. `STX` is the *start of text* ASCII code `0x02`, `LFD` is a continous number, looping between 0 (ASCII `0x30`) and 9 (ASCII `0x39`), `DATA` is the command or response, `DLE` is the *data link escape* ASCII code `0x10`, `ETX` is the *end of text* ASCII code `0x03` and `CS` is a checksum. The checksum is computed as follows: Start with a null byte `0x00` and, from `STX` to `ETX`, for every byte of the message perform a bitwise exclusive or (`xor`) between the checksum byte and the current message byte. This corresponds to the protocol *3964R* used by Siemens programmable logic controllers (PLC, in German "Speicherprogrammierbare Steuerung", SPS).

Messages sent to the controller are either acknowledged with `DLE LFD`, acknowledging all received messages until message `LFD`, or rejected (e. g. because of a wrong checksum) with `NAK LFD` (`NAK` is the *negative acknowledgement* ASCII code `0x15`), requesting a

retransmit of all messages starting with `LFD`.

Error codes are transmitted as normal messages, with the content in the form `nERRc: m` with a component number `n` (which can be empty!), the error code `c` (an unsigned integer) and the plain-text error message `m`.

A.1.1. Initialisation

As a first step the serial interface should be reconfigured, if desired. This is done with the command `Midps,b`, where `M` is just a literal M, `i` is the interface number, which is 1 for the normal control interface, `d` is the number of data bits, which should be left at 8, `p` is the parity, which should be left as `e` for even parity, `s` is the number of stop bits, which should be set to 1, and finally `b` is the baud rate. Whilst the controller is theoretically capable of operating at 128 000 bd, this leads to transmission errors and missed commands. The maximum practical baud rate is 57 600 bd. Therefore, for maximum performance, one executes the command `M18e1,57600` at the start of each session.

It should be noted that the interface settings are valid until the device is turned off. Since a second try to set the interface to 57 600 bd over a (then wrong) 38 400 bd line results in all kinds of errors, precautions should be taken to avoid this. Usually, it is best to simply turn the controller off and on again if unsure of the current state.

Initialisation of all motors etc. is then performed by the `0INIT#1,2` command.

A.1.2. Positioning

Position reporting of the stage is performed based on data from two RGH24 linear encoder systems (Renishaw, United Kingdom). The position is represented as a (signed) integer, with one unit corresponding to 50 nm. The movement range of the stage is 161.343 mm × 76.580 mm, corresponding to 3 226 860 units × 1 531 600 units.

Initial position calibration, moving the stage to one endpoint location and setting that position as $(0, 0)$ is performed with the command `0REF#`. Depending on the starting position, this command may time out with an error message. In such a case the command has to be executed again, until no errors occur. Completed calibration results in the message `0STAT1,2,1` from the controller.

During stage movement the controller sends the current position to the PC every 100 ms in the format `0RPx,y` with `x` and `y` (possibly signed if performed prior to position calibration) integers in system units. Once stage movement has finished, a message `0REx,y` is sent. On demand position reporting can be achieved with the command

`0TP#`, returning a `0RPEx,y` message.

A.1.3. Normal Mode

In normal mode, the system moves to specified positions with specified velocities. It is activated with the command `0MN#XY,1` for slow movement or `0MN#XY,2` for fast movement.

Movement to a specific position (x, y) with speed `s` is performed with the command `0PXY#x,y,s`. The speed with the preceding comma is optional.

A.1.4. Continuous Mode

In continuous mode, the system is able to move along an axis with defined velocity until told to stop or until reaching the endpoint. This mode is activated with the command `0MC#XY,1` for slow movement or `0MC#XY,2` for fast movement.

Motion is started with the command `0G#ad,v` with the axis definition `a`, which can be either `X`, `Y` or `XY`, the direction `d` with is either `+` or `-`, and the velocity `v`. Again, the velocity is optional and can be omitted together with the preceding comma. Concurrent movement of both axis with different velocities or directions is possible by simply issuing the command twice, once for each axis.

Motion is stopped with the command `0K#a` with the axis definition `a` as above.

For reliability, position requests should only be performed if the system is stopped. As mentioned above, they are achieved by executing the command `0TP#`.

A.2. Detection implementation

A.2.1. Setup

The setup consists of the linear stage, which is attached to an adapter suitable for the used microscope. During measurements, it is of utmost importance that the prism is set to camera only, since otherwise light is lost and whatever is in front of the oculars will be slightly projected onto the image.

To enable focus corrections, the chip is not placed directly on the stage, but on a tripod which is placed into a rectangular cavity in the stage.

The complete detection process is controlled by a LabView program, which directs the user and is interacted with mostly via an attached joystick.

A.2.2. Rotation calibration

The rotation between stage and camera is not fixed and therefore has to be calibrated prior to each measurement. For early experiments, millimeter graph paper was fixated on the stage surface. I made three tiny adjacent perforations in the paper with a needle, resulting in black dots in the image. They are detected automatically by performing a colour threshold with subsequent particle filtering, resulting in three positions. The rotation is then calculated by comparing the angle of the line connecting the two dots farthest apart with a value obtained from an initial calibration. This rotational correction angle is stored for subsequent corrections.

A.2.3. Scanning, recording and stitching

After rotation correction, the stage moves to the centre position of the chip platform. Now, the user can direct the stage with the joystick and select edges of the polygon to be scanned. During this selection, the user should also pay attention to the image focus and adjust the chip platform, if necessary. Then, the bounding box of the polygon is separated into rectangles of 998 px × 644 px or 438.7 µm × 284.8 µm size. For each rectangle, it is checked whether it lies within the polygon. These rectangles are then put into order. Since the individual images taken are 1024 px × 680 px in size, an overlap of 13 px to the right and left and 18 px above and below is created, which is needed later for rotation correction of up to 2°. The resulting image positions are illustrated in fig. A.1.

During the scanning process, the stage is moved to the next image location. After sending the movement command, a delay of at least 750 ms is executed. If the next image location is not directly adjacent to the previous location, the delay is proportionally longer. Then, the image is taken and stored on disk. This is repeated until all image locations are processed.

Unfortunately, image acquisition is not as straightforward as one might imagine. Since there is no suitable API for the live view available, the following hack is used: First, the *Print Screen* key is sent to Windows. After a 100 ms delay, the clipboard contents are then converted to a Labview compatible image format and cropped to the position of the live view on screen. Of course, this requires the live view to be visible and always on the same location on screen. Therefore, a second monitor is used dedicated to displaying the live view maximised.

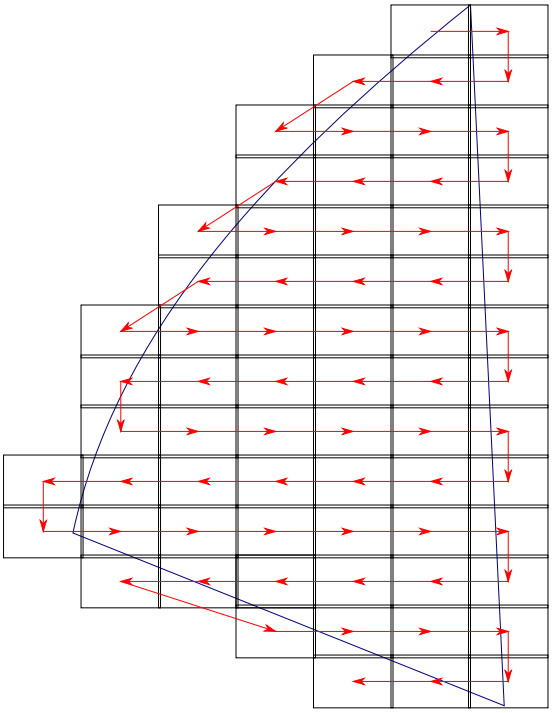

Fig. A.1.: Illustration of scanning positions and path

A.2.4. Flake detection

After all images are taken, multiple slightly overlapping large images of the chip are stitched together. Multiple images are required since LabView is limited to 2 GB images even in 64-bit mode. The overlapping and stitching are required since a flake could be placed centred on the seam between two images and would not be detected otherwise.

Once the large images are created and saved to disk, a $7\,\mathrm{px} \times 7\,\mathrm{px}$ Gaussian blur is applied to the image, which removes any disturbing colour noise. Then, a colour threshold is performed. This converts the colour image into a binary image, with the pixels set to 1 if the colour was in the threshold range and to 0 if it was not.

The colour threshold of course is flake material dependent and has to be determined manually for each new material. For that purpose, I created and additional helper program, which reads the large image, applies the blur, magnifies it in such a way that each individual pixel is clearly visible and writes the colour data into each magnified pixel. A region containing a manually found suitable flake is then selected and the colour region of interest adjusted accordingly. As a feedback, the colour information itself is colour coded to represent whether the pixel falls within the colour range.

Once the binary image is created, a distance map is calculated. For each pixel, the distance to the nearest 0 pixel is calculated. The resulting grey-scale map is saved as well. Assuming a point in this distance map has the value of 11, this means that centred on this pixel, a circle with a radius of 11 px, corresponding to a diameter of 9.5 µm, can be placed that never leaves the region with correct colour, which is exactly what we require. Therefore, in the original image, all areas with a corresponding distance map value of 11 or greater are marked and presented to the user.

The user then can either magnify each individual image location or simply click on it to have the stage move to the corresponding position on the chip. The user should then decide whether the result is a true or false positive and note true positives with the corresponding location and flake quality. Once this is performed for the whole chip, the user can then mark the best positions with a fine felt pen marker (by placing two dots on either side of the flake). During this marking phase, care should be taken to not move the chip too much, since the program of course cannot detect manual movement of the chip on the tripod and therefore finding further flake positions again is impeded.

B. List of figures

C. Bibliography

[1]K. C. Neuman and A. Nagy, "Single-molecule force spectroscopy: optical tweezers, magnetic tweezers and atomic force microscopy.", Nature Methods **5**, 491–505 (2008).

[2]D. Branton, D. W. Deamer, A. Marziali, H. Bayley, S. A. Benner, T. Butler, M. Di Ventra, S. Garaj, A. Hibbs, X. Huang, S. B. Jovanovich, P. S. Krstic, S. Lindsay, X. S. Ling, C. H. Mastrangelo, A. Meller, J. S. Oliver, Y. V. Pershin, J. M. Ramsey, R. Riehn, G. V. Soni, V. Tabard-Cossa, M. Wanunu, M. Wiggin, and J. A. Schloss, "The potential and challenges of nanopore sequencing.", Nature Biotechnology **26**, 1146–1153 (2008).

[3]J. L. Huppert, "Four-stranded nucleic acids: structure, function and targeting of G-quadruplexes.", Chemical Society Reviews **37**, 1375–1384 (2008).

[4]T. Osaki, H. Suzuki, B. Le Pioufle, and S. Takeuchi, "Multichannel simultaneous measurements of single-molecule translocation in α-hemolysin nanopore array", Analytical Chemistry **81**, 9866–9870 (2009).

[5]L. X. Tiefenauer and A. Studer, "Nano for bio: nanopore arrays for stable and functional lipid bilayer membranes (Mini Review).", Biointerphases **3**, FA74 (2008).

[6]J. Li, D. Stein, C. McMullan, D. Branton, M. J. Aziz, and J. a. Golovchenko, "Ion-beam sculpting at nanometre length scales.", Nature **412**, 166–169 (2001).

[7]A. Ashkin, "Acceleration and Trapping of Particles by Radiation Pressure", Physical Review Letters **24**, 156–159 (1970).

[8]A. Ashkin, "Optical Levitation by Radiation Pressure", Applied Physics Letters **19**, 283 (1971).

[9]A. Ashkin, J. M. Dziedzic, J. E. Bjorkholm, and S. Chu, "Observation of a single-beam gradient force optical trap for dielectric particles", Optics Letters **11**, 288 (1986).

[10]S. M. Block, L. S. Goldstein, and B. J. Schnapp, "Bead movement by single kinesin molecules studied with optical tweezers.", Nature **348**, 348–52 (1990).

[11]C. Bustamante, J. Marko, E. Siggia, and S. Smith, "Entropic elasticity of lambda-phage DNA", Science **265**, 1599–1600 (1994).

[12]A. Sischka, "Aufbau einer Optischen Pinzette", PhD thesis (Bielefeld University, 2002).

[13]A. Sischka, C. Kleimann, W. Hachmann, M. M. Schafer, I. Seuffert, K. Tönsing, and D. Anselmetti, "Single beam optical tweezers setup with backscattered light detection for three-dimensional measurements on DNA and nanopores", Review of Scientific Instruments **79**, 063702 (2008).

[14]S. Knust, A. Spiering, H. Vieker, A. Beyer, A. Gölzhäuser, K. Tönsing, A. Sischka, and D. Anselmetti, "Video-based and interference-free axial force detection and analysis for optical tweezers", Review of Scientific Instruments **83**, 103704 (2012).

[15]J. Eichler and H. J. Eichler, *Laser: Bauformen, Strahlführung, Anwendungen*, 6. Auflage (Springer, 2006).

[16]O. Svelto, *Principles of Lasers* (Springer US, Boston, MA, 2010), `http://link.springer.com/10.1007/978-1-4419-1302-9`.

[17]L. G. Gouy, "Sur une propriété nouvelle des ondes lumineuses", Comptes rendus hebdomadaires des séances de l'Académie des sciences **110**, 1251 (1890).

[18]N. Sultanova, S. Kasarova, and I. Nikolov, "Dispersion Properties of Optical Polymers", Acta Physica Polonica A **116**, 585 (2009).

[19]M. Daimon and A. Masumura, "Measurement of the refractive index of distilled water from the near-infrared region to the ultraviolet region", Applied Optics **46**, 3811 (2007).

[20]A. Ashkin, "Forces of a single-beam gradient laser trap on a dielectric sphere in the ray optics regime", Biophysical Journal **61**, 569–582 (1992).

[21]M. Kerker, *The scattering of light - and other electromagnetic radiation*, edited by E. M. Loebl (Academic Press, New York, 1969).

[22]P. Langevin, "Sur la théorie du mouvement brownien", Comptes rendus hebdomadaires des séances de l'Académie des sciences **146**, 530 (1908).

[23]D. S. Lemons, "Paul Langevin's 1908 paper "On the Theory of Brownian Motion" ["Sur la théorie du mouvement brownien," C. R. Acad. Sci. (Paris) 146, 530–533 (1908)]", American Journal of Physics **65**, 1079 (1997).

[24]L. D. Landau and E. M. Lifschitz, *Lehrbuch der theoretischen Physik - Band VI: Hydrodynamik*, edited by W. Weller, 5. Auflage (Verlag Harri Deutsch, Frankfurt am Main, 2007).

[25]B. M. Lansdorp and O. A. Saleh, "Power spectrum and Allan variance methods for calibrating single-molecule video-tracking instruments.", Review of Scientific Instruments **83**, 025115 (2012).

[26]Laser 2000, *Laser und Lichtquellen*, 2011, `http://www.laser2000.de/index.php?id=363099`.

[27]A. Rohrbach and E. H. K. Stelzer, "Three-dimensional position detection of optically trapped dielectric particles", Journal of Applied Physics **91**, 5474 (2002).

[28]W. Denk and W. W. Webb, "Optical measurement of picometer displacements of transparent microscopic objects.", Applied optics **29**, 2382–91 (1990).

[29]U. F. Keyser, J. van der Does, C. Dekker, and N. H. Dekker, "Optical tweezers for force measurements on DNA in nanopores", Review of Scientific Instruments **77**, 105105 (2006).

[30]H. Kramers, "Brownian motion in a field of force and the diffusion model of chemical reactions", Physica **7**, 284–304 (1940).

[31]A. Spiering, S. Getfert, A. Sischka, P. Reimann, and D. Anselmetti, "Nanopore translocation dynamics of a single DNA-bound protein.", Nano Letters **11**, 2978–82 (2011).

[32]A. R. Carter, G. M. King, and T. T. Perkins, "Back-scattered detection provides atomic-scale localization precision, stability, and registration in 3D.", Optics Express **15**, 13434–45 (2007).

[33]J. Crocker, "Methods of Digital Video Microscopy for Colloidal Studies", Journal of Colloid and Interface Science **179**, 298–310 (1996).

[34]G. M. Gibson, J. Leach, S. Keen, A. J. Wright, and M. J. Padgett, "Measuring the accuracy of particle position and force in optical tweezers using high-speed video microscopy", Optics Express **16**, 14561 (2008).

[35]O. Otto, F. Czerwinski, J. L. Gornall, G. Stober, L. B. Oddershede, R. Seidel, and U. F. Keyser, "Real-time particle tracking at 10,000 fps using optical fiber illumination", Optics Express **18**, 22722–22733 (2010).

[36]M. Wu, J. W. Roberts, and M. Buckley, "Three-dimensional fluorescent particle tracking at micron-scale using a single camera", Experiments in Fluids **38**, 461–465 (2005).

[37]K. Svoboda and S. M. Block, "Biological applications of optical forces.", Annual Review of Biophysics and Biomolecular Structure **23**, 247–85 (1994).

[38]J. Happel and H. Brenner, *Low Reynolds number hydrodynamics*, 1st paperb (Martinum Nijhoff Publishers, The Hague, The Netherlands, 1983).

[39]D. Allan, "Statistics of atomic frequency standards", Proceedings of the IEEE **54**, 221–230 (1966).

[40]N. Wiener, "Generalized harmonic analysis", Acta Mathematica **55**, 117–258 (1930).

[41]J. A. Barnes, A. R. Chi, L. S. Cutler, D. J. Healey, D. B. Leeson, T. E. McGunigal, J. A. Mullen, W. L. Smith, R. L. Sydnor, R. F. C. Vessot, and G. M. R. Winkler, "Characterization of Frequency Stability", IEEE Transactions on Instrumentation and Measurement **IM-20**, 105–120 (1971).

[42]H. Yin, M. D. Wang, K. Svoboda, R. Landick, S. M. Block, and J. Gelles, "Transcription against an applied force.", Science **270**, 1653–7 (1995).

[43]S. van Dorp, U. F. Keyser, N. H. Dekker, C. Dekker, and S. G. Lemay, "Origin of the electrophoretic force on DNA in solid-state nanopores", Nature Physics **5**, 347–351 (2009).

[44]M. D. Wang, H. Yin, R. Landick, J. Gelles, and S. M. Block, "Stretching DNA with optical tweezers.", Biophysical Journal **72**, 1335–46 (1997).

[45]P. Christen and R. Jaussi, *Biochemie*, Springer-Lehrbuch (Springer-Verlag, Berlin/Heidelberg, 2005), `http://www.springerlink.com/index/10.1007/b137457`.

[46]J. F. Marko and E. D. Siggia, "Stretching DNA", Macromolecules **28**, 8759–8770 (1995).

[47]H. Yamakawa, "Stiff-Chain Macromolecules", Annual Review of Physical Chemistry **35**, 23–47 (1984).

[48]M. Janitz, ed., *Next-Generation Genome Sequencing* (Wiley-VCH, Weinheim, 2008).

[49]J. R. Miller, S. Koren, and G. Sutton, "Assembly algorithms for next-generation sequencing data.", Genomics **95**, 315–27 (2010).

[50]M. Baker, "De novo genome assembly: what every biologist should know", Nature Methods **9**, 333–337 (2012).

[51]L. Galla, A. J. Meyer, A. Spiering, A. Sischka, M. Mayer, A. R. Hall, P. Reimann, and D. Anselmetti, "Hydrodynamic Slip on DNA Observed by Optical Tweezers-Controlled Translocation Experiments with Solid-State and Lipid-Coated Nanopores", Nano Letters **14**, 4176–4182 (2014).

[52]A. Sischka, L. Galla, A. J. Meyer, A. Spiering, S. Knust, M. Mayer, A. R. Hall, A. Beyer, P. Reimann, A. Goelzhaeuser, and D. Anselmetti, "Controlled Translocation of DNA Through Nanopores in Carbon Nano-, Silicon-Nitride- and Lipid-Coated Membranes", Analyst, Advance Article (2015).

[53]S. Getfert, T. Töws, and P. Reimann, "Reluctance of a neutral nanoparticle to enter a charged pore", Physical Review E **88**, 052710 (2013).

[54]W. R. Hogg and W. H. Coulter, *Apparatus and method for measuring a dividing particle size of a particulate system*, 1971.

[55]J. J. Kasianowicz, E. Brandin, D. Branton, and D. W. Deamer, "Characterization of individual polynucleotide molecules using a membrane channel", Proceedings of the National Academy of Sciences of the United States of America **93**, 13770–13773 (1996).

[56]E. C. Yusko, J. M. Johnson, S. Majd, P. Prangkio, R. C. Rollings, J. Li, J. Yang, and M. Mayer, "Controlling protein translocation through nanopores with bio-inspired fluid walls.", Nature Nanotechnology **6**, 253–60 (2011).

[57]B. Hille, *Ion Channels of Excitable Membranes*, 3rd Ed. (Sinauer Associates, Inc., Sunderland, MA, 2001).

[58]K. S. Novoselov, A. K. Geim, S. V. Morozov, D. Jiang, Y. Zhang, S. V. Dubonos, I. V. Grigorieva, and A. A. Firsov, "Electric field effect in atomically thin carbon films.", Science **306**, 666–9 (2004).

[59]A. C. Ferrari, J. C. Meyer, V. Scardaci, C. Casiraghi, M. Lazzeri, F. Mauri, S. Piscanec, D. Jiang, K. S. Novoselov, S. Roth, and a. K. Geim, "Raman spectrum of graphene and graphene layers", Physical Review Letters **97**, 187401 (2006).

[60]R. R. Nair, P. Blake, A. N. Grigorenko, K. S. Novoselov, T. J. Booth, T. Stauber, N. M. R. Peres, and A. K. Geim, "Fine structure constant defines visual transparency of graphene.", Science **320**, 1308 (2008).

[61]H. Deville and F. Wohler, "Ueber das Stickstoffsilicium", Annalen der Chemie und Pharmacie **104**, 256–256 (1857).

[62]A. Sischka, A. Spiering, M. Khaksar, M. Laxa, J. König, K.-J. Dietz, and D. Anselmetti, "Dynamic translocation of ligand-complexed DNA through solid-state nanopores with optical tweezers.", Journal of Physics: Condensed Matter **22**, 454121 (2010).

[63]T. M. Bayerl and M. Bloom, "Physical properties of single phospholipid bilayers adsorbed to micro glass beads. A new vesicular model system studied by 2H-nuclear magnetic resonance.", Biophysical Journal **58**, 357–362 (1990).

[64]C. E. Miller, J. Majewski, T. Gog, and T. L. Kuhl, "Characterization of biological thin films at the solid-liquid interface by X-ray reflectivity", Physical Review Letters **94**, 238104 (2005).

[65]B. Luan and A. Aksimentiev, "Electro-osmotic screening of the DNA charge in a nanopore", Physical Review E **78**, 021912 (2008).

[66]S. Kesselheim, W. Müller, and C. Holm, "Origin of current blockades in nanopore translocation experiments", Physical Review Letters **112**, 018101 (2014).

[67]M. Ströck, *DNA Overview*, 2006, `http://commons.wikimedia.org/wiki/File:DNA%5C_Overview.png` (visited on 05/03/2015).

[68]C. Lee, X. Wei, J. W. Kysar, and J. Hone, "Measurement of the elastic properties and intrinsic strength of monolayer graphene.", Science **321**, 385–388 (2008).

[69]G. Diankov, M. Neumann, and D. Goldhaber-Gordon, "Extreme Mono layer-Selectivity of Hydrogen-Plasma Reactions with Graphene", ACS Nano **7**, 1324–1332 (2013).

[70]The Royal Swedish Academy of Sciences, *Scientific Background on the Nobel Prize in Physics 2010 - Graphene*, tech. rep. (2010).

[71]A. K. Geim and K. S. Novoselov, "The rise of graphene.", Nature Materials **6**, 183–191 (2007).

[72]G. F. Schneider, S. W. Kowalczyk, V. E. Calado, G. Pandraud, H. W. Zandbergen, L. M. K. Vandersypen, and C. Dekker, "DNA Translocation through Grapheme Nanopores", Nano Letters **10**, 3163–3167 (2010).

[73]C. A. Merchant, K. Healy, M. Wanunu, V. Ray, N. Peterman, J. Bartel, M. D. Fischbein, K. Venta, Z. Luo, A. T. C. Johnson, and M. Drndić, "DNA translocation through graphene nanopores", Nano Letters **10**, 2915–2921 (2010).

[74]S. Garaj, W. Hubbard, a. Reina, J. Kong, D. Branton, and J. a. Golovchenko, "Graphene as a subnanometre trans-electrode membrane.", Nature **467**, 190–193 (2010).

[75]J. E. Mark, A. Eisenberg, W. W. Graessley, L. Mandelkern, and J. L. Koenig, *Physical Properties of Polymers* (American Chemical Society, Washington, D.C., 1984).

[76]G. W. C. Kaye and T. H. Laby, *Tables of Physical & Chemical Constants*, 16th Ed. (Kaye & Laby Online Version 1.0, 2005), http://www.kayelaby.npl.co.uk/.

[77]F. Schreiber, "Structure and growth of self-assembling monolayers", Progress in Surface Science **65**, 151–256 (2000).

[78]D. K. Schwartz, "Mechanisms and kinetics of self-assembled monolayer formation.", Annual Review of Physical Chemistry **52**, 107–137 (2001).

[79]A. Turchanin and A. Gölzhäuser, "Carbon nanomembranes from self-assembled monolayers: Functional surfaces without bulk", Progress in Surface Science **87**, 108–162 (2012).

[80]W. Eck, V. Stadler, W. Geyer, M. Zharnikov, A. Gölzhäuser, and M. Grunze, "Generation of surface amino groups on aromatic self-assembled monolayers by low energy electron beams - a first step towards chemical lithography", Advanced Materials **12**, 805–808 (2000).

[81]C. Sommer, *Forschungsbericht: DNA Translokation durch Graphennanoporen und Charakterisierung von Carbon Nano Sheets auf Siliziumnitrid-Chips*, tech. rep. (Universität Bielefeld, 2013).

[82]Q. H. Wang, "Graphene is not alone", Nature Nanotechnology **7**, 683 (2012).

[83]A. Castellanos-Gomez, L. Vicarelli, E. Prada, J. O. Island, K. L. Narasimha-Acharya, S. I. Blanter, D. J. Groenendijk, M. Buscema, G. a. Steele, J. V. Alvarez, H. W. Zandbergen, J. J. Palacios, and H. S. J. van der Zant, "Isolation and characterization of few-layer black phosphorus", 2D Materials **1**, 025001 (2014).

[84]Y. Yamada-Takamura and R. Friedlein, "Progress in the materials science of silicene", Science and Technology of Advanced Materials **15**, 064404 (2014).

[85]J. Sone, T. Yamagami, Y. Aoki, K. Nakatsuji, and H. Hirayama, "Epitaxial growth of silicene on ultra-thin Ag(111) films", New Journal of Physics **16**, 095004 (2014).

[86]M. E. Dávila, L. Xian, S. Cahangirov, A. Rubio, and G. L. Lay, "Germanene: a novel two-dimensional Germanium allotrope akin to Graphene and Silicene", New Journal of Physics **16**, 095002 (2014).

[87]G. A. Gibson, A. Chaiken, K. Nauka, C. C. Yang, R. Davidson, A. Holden, R. Bicknell, B. S. Yeh, J. Chen, H. Liao, S. Subramanian, D. Schut, J. Jasinski, and Z. Liliental-Weber, "Phase-change recording medium that enables ultrahigh-density electron-beam data storage", Applied Physics Letters **86**, 1–3 (2005).

[88]C. Tresca, F. Ricci, and G. Profeta, "Strain effects in monolayer iron-chalcogenide superconductors", 2D Materials **2**, 015001 (2014).

D. Declaration of own work

Ich erkläre hiermit, dass ich diese Arbeit eigenständig und nur mit den angegebenen Hilfsmitteln verfasst habe. Diese Arbeit dient zum Erlangen des Grades *Master of Science* an der Universität Bielefeld und wurde zuvor an keiner anderen Hochschule eingereicht.

Bielefeld, _____

_____

Sebastian Knust